Featured in Physics

Respiratory aerosols and droplets in the transmission of infectious diseases

Mira L. Pöhlker*

Multiphase Chemistry Department, Max Planck Institute for Chemistry, 55128 Mainz, Germany, Leipzig Institute for Meteorology, Leipzig University, 04318 Leipzig, Germany, and Department of Atmospheric Microphysics, Leibniz Institute for Tropospheric Research, 04318 Leipzig, Germany

Christopher Pöhlker,† Ovid O. Krüger, Jan-David Förster, Thomas Berkemeier, Wolfgang Elbert, Janine Fröhlich-Nowoisky, and Ulrich Pöschl

Multiphase Chemistry Department, Max Planck Institute for Chemistry, 55128 Mainz, Germany

Gholamhossein Bagheri and Eberhard Bodenschatz

Laboratory for Fluid Physics, Pattern Formation and Biocomplexity, Max Planck Institute for Dynamics and Self-Organization, 37018 Göttingen, Germany

J. Alex Huffman

Department of Chemistry and Biochemistry, University of Denver, Denver, Colorado 80208, USA

Simone Scheithauer

Institute of Infection Control and Infectious Diseases, University Medical Center, Georg August University, 37075 Göttingen, Germany

Eugene Mikhailov

St. Petersburg State University, St. Petersburg 199034, Russia and Multiphase Chemistry Department, Max Planck Institute for Chemistry, Mainz, Germany

(published 12 October 2023)

Knowing the physicochemical properties of exhaled droplets and aerosol particles is a prerequisite for a detailed mechanistic understanding and effective prevention of the airborne transmission of infectious human diseases. This review provides a critical consideration and synthesis of scientific knowledge on the number concentrations, size distributions, composition, mixing state, and related properties of respiratory particles emitted upon breathing, speaking, singing, coughing, and sneezing. A parametrization of respiratory particle size distributions is derived and presented based on five log-normal modes related to different origins in the respiratory tract, which can be used to trace and localize the sources of infectious particles. This approach may support the medical treatment as well as the risk assessment for aerosol and droplet transmission of infectious diseases. It was applied to analyze which respiratory activities may drive the spread of specific pathogens, such as *Mycobacterium tuberculosis*, influenza viruses, and severe acute respiratory syndrome coronaviruses 2 (SARS-CoV-2). The results confirm the high relevance of vocalization for the transmission of SARS-CoV-2, as well as the usefulness of physical distancing, face masks, room ventilation, and air filtration as preventative measures against coronavirus disease 2019 and other airborne infectious diseases.

DOI: 10.1103/RevModPhys.95.045001

*poehlker@tropos.de
†c.pohlker@mpic.de

CONTENTS

I. INTRODUCTION

Diseases that spread via the respiratory tract, such as measles, tuberculosis, influenza, and the coronavirus disease 2019 (COVID-19), have played dramatic and important roles in global public health (Wells, 1955; Riley, 1974; Kutter *et al.*, 2018; Cyranoski, 2020). Disease outbreaks can be driven, entirely or in large part, by emissions of pathogen-laden particles that can infect nearby persons, such as those expelled in a spray of droplets or in turbulent gas clouds with suspended small airborne aerosols of widely variable concentration (Bloom and Murray, 1992; Morawska, 2006; Tellier *et al.*, 2019; Bourouiba, 2020; Milton, 2020; Seminara *et al.*, 2020; Tang *et al.*, 2021). A detailed understanding of the dynamics of such airborne pathogen transmission in space and time is needed to improve public health interventions, which are a cornerstone in pandemic control besides vaccination strategies, to control outbreaks and reduce infection rates (Richard and Fouchier, 2016; Milton, 2020).

Several transmission routes for pathogens passable between humans are known (Seto, 2015; Judson and Munster, 2019; Kohanski, Lo, and Waring, 2020; Leung, 2021; Li, 2021). The most widely occurring and relevant routes can be separated into contact and contact-free groups. Contact transmission from an infected individual to a susceptible recipient can occur through either direct person-to-person contact (such as a handshake) or indirect contact via contaminated objects or surfaces (fomites), followed by a hand-to-face transport of pathogens (i.e., self-inoculation of the eyes, nose, or mouth) (Hendley, Wenzel, and Gwaltney, 1973; Pancic, Carpentier, and Came, 1980; Boone and Gerba, 2007; Reynolds *et al.*, 2016). Transmission without physical contact, i.e., through the air, can occur via both near- and far-field transmission from either small or large particles emitted by the mouth or nose of infected individuals via coughing, sneezing, talking, or even breathing (Morawska, 2006; Schulze-Röbbecke, 2014; Chen *et al.*, 2020; Fennelly, 2020; NASEM, 2020; Li, 2021; Tang *et al.*, 2021). For this pathway, the terms contact-free and airborne are in use. Particles containing viable pathogens can then land directly on the mucosal surfaces of the recipient or can be inhaled. This review focuses only on emissions from the respiratory tract, defined here as the path of respiratory air from the deep lungs through the mouth and nose. Nevertheless, other emissions of potentially pathogen-laden particles, for instance, from the human body (i.e., the "personal cloud" effect of skin and clothing emissions), and of aerosolized fecal material can also play critical roles in disease transmission if deposited in the respiratory tract of a recipient (Sherertz, Bassetti, and Bassetti-Wyss, 2001; Johnson *et al.*, 2013; You *et al.*, 2013; Meadow *et al.*, 2015; Yamamoto *et al.*, 2015; Lai *et al.*, 2018; Kang *et al.*, 2020; Yang *et al.*, 2021).

Particles with larger diameters are often called droplets in the context of respiratory emissions, although the definition of the droplet threshold size has been the subject of a lively debate (Zhang *et al.*, 2020; Li, 2021; Randall *et al.*, 2021; Tang *et al.*, 2021). A dividing size of 5 μm has been utilized, most prominently in the medical community (Langmuir, 1961). An original work by Wells (1934) and several more recent studies, mostly from the aerosol community (Chen *et al.*, 2020), instead advocated for a dividing size of 100 μm, which can be better justified physically and physiologically. After emission, droplets follow (semi)ballistic trajectories to deposit directly onto objects or mucosal surfaces, i.e., in the nose, mouth, or eyes. Owing to the large mass they are only weakly influenced by the airflow and inhalation is relatively unlikely (Vincent *et al.*, 1990; Hinds, 1999; Volkwein, Maynard, and Harper, 2011). Droplets larger than ∼100 μm also have too much mass to stay suspended for longer than a few seconds and thus fall to the ground rapidly within about 1 or 2 m of the emitter (Wells, 1934; Chen *et al.*, 2020). The near-field deposition of droplets depends largely on particle size and emission velocity, and thus extends increasingly far from the source via singing or shouting as well as coughing or

sneezing (Xie *et al.*, 2007; Bourouiba, Dehandschoewercker, and Bush, 2014; Bourouiba, 2020; Mittal, Ni, and Seo, 2020b; Bourouiba, 2021). This was recently confirmed using detailed numerical simulations (Chong *et al.*, 2021; Wang *et al.*, 2021). Particles with diameters smaller than ∼100 μm have been called aerosols or droplet nuclei in the context of respiratory emissions and have a sufficiently small mass and momentum to be inhalable via airflow into the respiratory tract (Wells, 1934; Vincent *et al.*, 1990; Randall *et al.*, 2021). Respiratory aerosols are generally present in the highest concentration in the near field in a plume closest to the emitter but can also mix readily into a volume of air in the far field (Chen *et al.*, 2020; Lelieveld *et al.*, 2020; Tang *et al.*, 2021). They can remain suspended for minutes or even hours, depending on particle size, the free air turbulence or flow dynamics, and ventilation rates (Bourouiba, 2021; Helleis, Klimach, and Pöschl, 2021). Thus, it can be possible for aerosols to be the dominant mode of transmission in both the near field (1 to 2 m) and the far field (for instance, mixed into the room air) (Chen *et al.*, 2020; Nissen *et al.*, 2020; Yang *et al.*, 2020; Li, 2021), though mitigation strategies may differ within the two categories of distance.

Disease transmission through exhaled particles can tend predominantly toward the aerosol route if mostly small and readily airborne particles containing viable pathogens are emitted, or predominantly toward the droplet route if mostly large and (semi)ballistically distributed droplets are involved. The predominant pathway not only is a function of respiratory activity, which strongly influences the size distribution of exhaled particles, but also may depend on the disease, which can be associated with a markedly different pathogen load in different parts of the respiratory tract. The boundary between aerosols and droplets is fraught because, from a physical perspective, they lie at different ends of the size continuum (Wilson *et al.*, 2020). The historically used dividing size of 5 μm has been debated controversially, as it has relatively little support from either physical or physiological reasoning (Li, 2021; Randall *et al.*, 2021; Tang *et al.*, 2021). For example, the settling velocity of a 5 μm droplet leads to a residence time of 25 min. Upward convection from body heat and other turbulent dynamics makes the estimation of residence time more complicated, but even particles smaller than this will mix into the majority of the room volume and are thus relevant for inhalation in the far field. More recently a dividing size of 100 μm has been discussed as a more physically grounded threshold (Prather *et al.*, 2020), largely because this is approximately the size above which particles are unlikely to be inhaled, based on the physics of airflow into the respiratory tract (Yeh and Schum, 1980; Heyder *et al.*, 1986; Hinds, 1999; Thomas, 2013). Note also that, while many communities differentiate between aerosol and droplet size regimes, the specific cut-point definition between the regimes can be different. In the near field, infection can be caused by ballistic droplet spray and contact-based mechanisms, as well as by inhalation of concentrated aerosol clouds, which means that near-field aerosol infection can mimic epidemiological patterns of large-droplet spray or contact infections (Roy and Milton, 2004; Chen *et al.*, 2020; Bourouiba, 2021). Accordingly, it can be complicated to separate these processes to identify the most significant route for a given pathogen (Milton, 2012; Tellier *et al.*, 2019; Fennelly, 2020; Morawska *et al.*, 2020). The size range of deposited pathogen-containing particles may also play an important role in the development and severity of a disease, which has been shown primarily in animal models thus far (Druett *et al.*, 1953; Day and Berendt, 1972; Roy, Reed, and Hutt, 2010; Port *et al.*, 2021).

The "classical" examples of pathogens that spread predominantly via aerosols are *Mycobacterium tuberculosis*, which causes tuberculosis (TB), the measles morbillivirus, which causes measles, and the varicella-zoster virus, which causes chicken pox (Riley *et al.*, 1959, 1962; Riley, Murphy, and Riley, 1978; Bloch *et al.*, 1985; Jones-Lopez *et al.*, 2013; Tellier *et al.*, 2019; Leung, 2021). Other examples of pathogens that can spread via aerosols are the bacterium *Coxiella burnetii*, which causes Q fever, and spores of *Bacillus anthracis*, which cause anthrax (Fennelly, Davidow *et al.*, 2004; de Rooij *et al.*, 2016). For the COVID-19 pandemic, which was caused by the readily transmissible severe acute respiratory syndrome coronavirus 2 (SARS-CoV-2) (Satija and Lal, 2007; Zuo, Uspal, and Wei, 2020), the preponderance of evidence suggests that SARS-CoV-2 is aerosol transmissible (Lednicky *et al.*, 2020, 2021; Liu *et al.*, 2020; Nissen *et al.*, 2020; van Doremalen *et al.*, 2020; Kutter *et al.*, 2021; Santarpia *et al.*, 2022), with virus-laden respiratory particles transmitted through the air being key drivers of infection (Kwon *et al.*, 2020; NASEM, 2020; Miller *et al.*, 2021). This is in line with studies suggesting that the closely related coronaviruses SARS-CoV-1 and Middle East respiratory syndrome coronavirus (MERS-CoV) also spread through aerosols (Olsen *et al.*, 2003; Wong *et al.*, 2004; Yu *et al.*, 2004; Booth *et al.*, 2005; Li *et al.*, 2005).

Figure 1 illustrates the life cycle of respiratory particles in contact-free pathogen transmission, spanning from exhalation over airborne transport to the potential infection of a recipient. The emission of particles in relation to respiratory activities such as breathing, speaking, singing, coughing, and sneezing has been analyzed in numerous studies, as summarized in reviews by Gralton *et al.* (2011), Han, Weng, and Huang (2013), and Bake *et al.* (2019). The fluid dynamics involved in the spread of the exhaled multiphase cloud of potentially pathogen-laden particles was summarized by Bourouiba (2021), Seminara *et al.* (2020), and Mittal, Ni, and Seo (2020b). The transmitted pathogen dose response of the recipient is determined by multiple factors, such as the number, size distribution, and physicochemical properties of the pathogen bearing particles being inhaled or deposited on mucosal surfaces during a given exposure time and the pathogen characteristics (Haas, 2015). The droplet route (particle diameters > 100 μm) is almost exclusively relevant in the near field through droplet spray deposition on persons or objects (creating fomites). The aerosol routes (particle diameter ≤ 100 μm) can be relevant in the near field upon inhalation of concentrated clouds of small particles near the emitter, as well as in the far field when small particles accumulate in indoor environments (such as in schools, in restaurants, and on public transport) or are distributed via directed airflow (such as air conditioning) before significant dilution occurs (Li *et al.*, 2005; Knibbs, Morawska, and Bell, 2012; Bourouiba, Dehandschoewercker, and Bush, 2014;

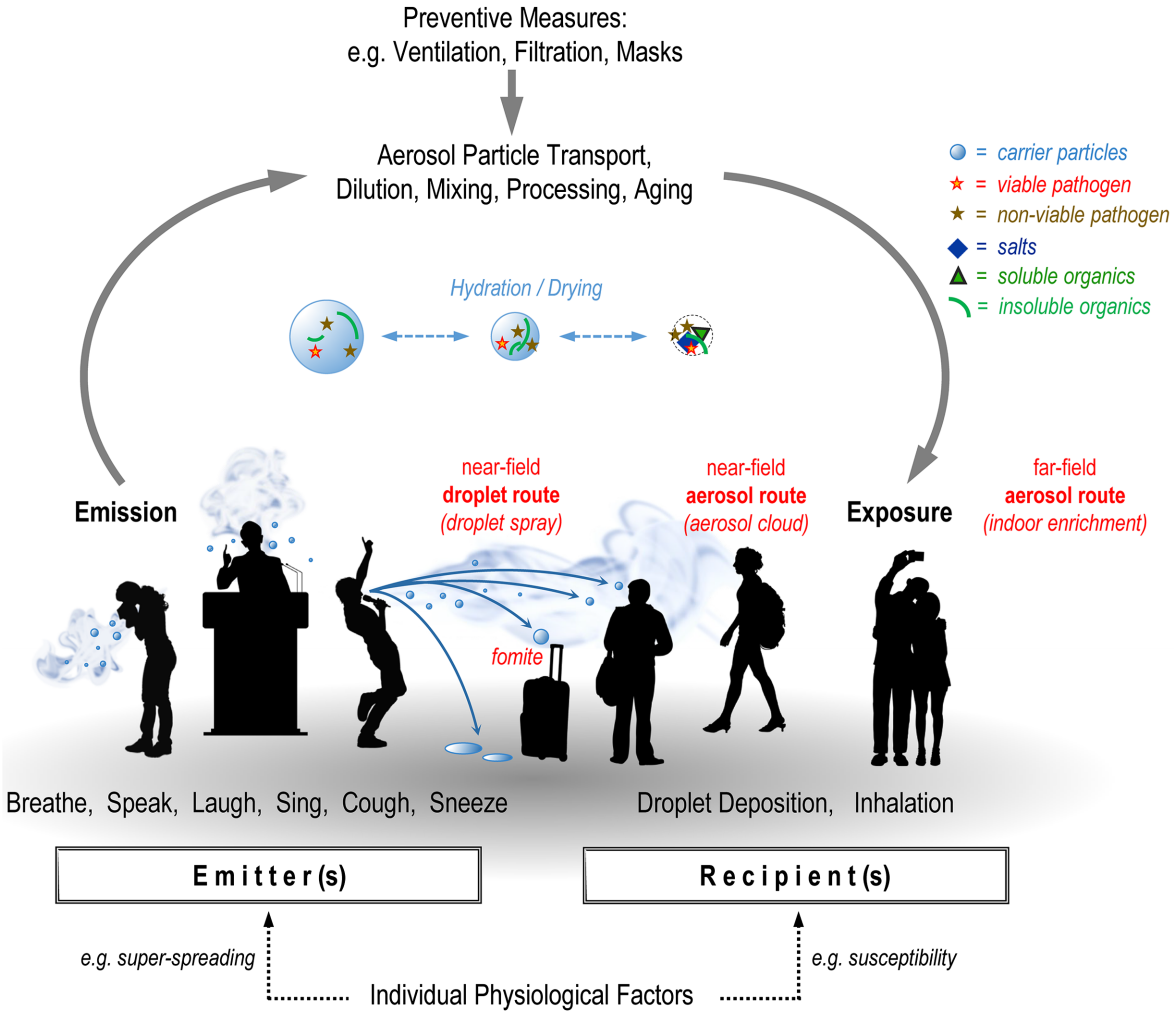

FIG. 1. Conceptual scheme of the aerosol and droplet pathogen transmission routes along with relevant physicochemical properties of respiratory particles.

Prussin, Garcia, and Marr, 2015; Birnir and Angheluta, 2020; Chen *et al.*, 2020; Stadnytskyi *et al.*, 2020; Yang *et al.*, 2020).

The aerosol infection pathway is influenced largely by individual physiological factors of both the emitter (for instance, high individual variation in infectiousness with low-spreading or superspreading individuals) and the recipient (enhanced susceptibility due to preexisting conditions, coinfections, etc.) (Lloyd-Smith *et al.*, 2005; Bischoff *et al.*, 2013; Edwards *et al.*, 2021; Leung, 2021; Miller *et al.*, 2021). The timing of maximum pathogen replication with associated exhalation and the encounter of emitter and recipient is also important. Current evidence on the replication and emission of wild-type SARS-CoV-2, for instance, peaks two to three days prior to and on the first days of symptom onset (Ferretti *et al.*, 2020; He *et al.*, 2020; Matricardi, Dal Negro, and Nisini, 2020). A mechanistic understanding of essential processes in Fig. 1 requires transdisciplinary bridges among infection epidemiology, virology, pulmonology, and immunology, as well as aerosol physics and chemistry, fluid dynamics, indoor-air science, and related fields (Morawska, 2006; Milton, 2020; Santl-Temkiv *et al.*, 2020).

This review addresses the microphysical particle properties involved in contact-free disease transmission caused by infectious agents within the human respiratory tract. It focuses particularly on the concentrations and size distributions of respiratory particles, as well as the distribution of pathogens within these carrier particle populations. Section II provides a general summary of definitions, nomenclature, and key parameters, as well as mechanistically relevant information on droplet formation in the respiratory tract, and is followed by rapid droplet desiccation after emission. Section III follows with a review and synthesis of the scientific literature on respiratory particle size distributions (PSDs) from breathing, speaking, and singing. The generalized multimodal, log-normal parametrization of exhaled PSDs introduced here is based on previous observations and parametrization approaches (Chao *et al.*, 2009; Morawska *et al.*, 2009; Johnson *et al.*, 2011; Han, Weng, and Huang, 2013; Asadi *et al.*, 2019; Bagheri *et al.*, 2023). The new parametrization (i) covers the size range of < 10 nm to > 1000 μm, (ii) is based on the smallest number of modes needed to adequately represent the available experimental PSDs weighted by both particle number and volume, (iii) is widely representative of the existing literature, and (iv) is readily applicable to modeling studies. The parametrization has further been related to the emission mechanisms and sites in the respiratory tract as

well as to mode-specific particle number concentrations in relation to different respiratory activities. Finally, using the multimodal parametrization, the emission mechanisms and particle size modes most closely associated with the spread of common pathogens are identified. The literature summary and consistent parametrization of the exhaled PSDs can be used as a framework for an improved understanding, control, and prevention of infectious disease transmission, such as for COVID-19 and other present and future diseases that spread via the respiratory tract.

II. DEFINITIONS, NOMENCLATURE, AND KEY PARAMETERS IN AEROSOL AND DROPLET PATHOGEN TRANSMISSION

A. Definitions and nomenclature on respiratory aerosol and droplets

A major challenge in the multidisciplinary field of airborne disease transmission is that the different scientific communities involved often do not "speak the same language" (Milton, 2020). Moreover, the terminology is not always clearly defined or consistently used, and thus can promote misunderstanding (Roy and Milton, 2004; Tang *et al.*, 2021). The fundamental terms aerosol and droplet are used especially inconsistently by different scientific communities and with different meanings and implications.

The term droplet can convey two broadly different concepts: (i) it is often used as a counterpart for aerosol in a dichotomous classification of airborne versus (semi)ballistic transmission routes (details to follow). In this sense, the term droplet is meant to differentiate a particular (large) particle size regime marked by aerodynamic behavior separate from the smaller range of the size continuum of respiratory particles. (ii) Moreover, the term droplet is also frequently used to mean respiratory particles that contain water. Note, however, that all respiratory particles comprise significant amounts of water upon exhalation, and thus can be considered droplets regardless of size (Bourouiba, 2021; Tang *et al.*, 2021). Further, the term droplet nuclei, as originally named by Wells (1934), is used for the remaining residues after the evaporation of respiratory droplets (Chao *et al.*, 2009; Bourouiba, Dehandschoewercker, and Bush, 2014; Niazi, Groth, Spann, and Johnson, 2021). This term is used primarily within broadly medically oriented communities and can be seen as a synonym of the term *condensation nuclei*, which is used broadly within the atmospheric physics community. As defined within the scope of atmospheric physics, nuclei are those particles involved in a nucleation process that lead to particle growth, such as a physical surface on which cloud droplets or ice crystals initiate growth. Note, however, that nuclei here refers to the end point of droplet desiccation, and thus shrinkage of a droplet rather than growth from a seed nucleus.

The term *aerosol* is used in some fields as a synonym for droplet nucleus, whereas communities of physical science typically use the term aerosol to refer to particles small enough to stay suspended in air for a certain period of time (as defined more specifically in this review). Use of the term *airborne* is especially contentious and is used inconsistently within the context of respiratory disease (Roy and Milton, 2004; Tellier *et al.*, 2019; Klompas, Baker, and Rhee, 2020; Li, 2021; Tang *et al.*, 2021). In most subfields of the physical sciences, the term airborne is broadly associated with particles that are suspended in or transported through the air. In this context, both smaller aerosol particles and droplets can be considered airborne, although the residence time in air and the ability to be inhaled varies strongly with particle size (Hinds, 1999; Morawska and Milton, 2020; Prather *et al.*, 2020). For these reasons, the majority of discussions associated with the term airborne among physical scientists are associated with aerosols (Chen *et al.*, 2020). In stark contrast to this perspective, nonphysical subfields of science and medicine have historically applied additional limitations to the use of the term airborne, for example, to aerosol-based diseases with demonstrably high basic reproduction numbers (R_0) such as measles, but without specific physical or mechanistic reasoning (Milton, 2020; Leung, 2021; Li, 2021; Tang *et al.*, 2021). A broader discussion of the differences in the way different communities define this term are not addressed in detail here. For the purposes of this discussion, we adopt a physical perspective of the term airborne comprising both smaller aerosols and larger droplets.

For clarity, we define here the terminology used throughout this manuscript:

- *Aerosol*.—An aerosol is defined as a suspension of liquid or solid particles in a gas, with particle diameters ranging from few nanometers up to about 100 μm (Hinds, 1999; Pöschl, 2005; Frohlich-Nowoisky *et al.*, 2016; Seinfeld and Pandis, 2016). Note that sometimes the plural term aerosols is used to refer specifically to the suspended particles, which frequently causes confusion in relation to the aforementioned rigorous definition of aerosol, which is already plural with respect to the particles involved. The term *droplet nuclei* is frequently taken within medical communities to be synonymous with aerosol.
- *Droplets*.—Generally speaking, droplets are liquid particles. In the medical and epidemiological literature the term droplet is frequently used for aqueous liquid particles larger than 5 μm in diameter. Here the term droplet is used cautiously to avoid misunderstanding. We use it only for aqueous droplets (of all sizes) directly upon emission from the respiratory tract, regardless of particle size. After the onset of drying (which happens quickly), the terms residue or dried particle are used for the partially or fully dried droplets. Note that we avoid using the term droplet nuclei.
- *Particle*.—The term particle refers here to the entire population of liquid or solid particles, encompassing the full spectrum of possible sizes, as well as physical and chemical states.

Throughout the review, we predominantly use the terms particle and aerosol and employ the term droplet to only a minor degree. Where not clear from the context, we further specify these terms with attributes defined by physical properties such as aerodynamic behavior, i.e., airborne versus (semi)ballistic, or water content, i.e., wet versus dry or dried. Often a particular particle size range is of relevance: in these

cases we have numerically specified the diameter thresholds (for instance, > 1 μm or from 0.1 to 10 μm). To broadly subdivide the modes of the particle size distribution into two groups according to the commonly applied set of measurement instrumentation (see Table IV and Secs. III.C.2 and III.C.3), we have used the relative terms small, for all modes centered below 5 μm, and large, for all modes centered above 5 μm. Note that this 5 μm threshold is not related to the traditionally used 5 μm threshold in a dichotomous classification of aerosol versus droplet infection routes (details to follow). Particle sizes in this review always refer to diameter, never to radius.

Neither the lower nor upper aerosol size ranges have rigorously defined physical limits: The lower limit is marked by a gradual transition from gas molecules and larger molecular clusters to nanometer-sized particles. The upper limit is given by the gradually changing aerodynamic properties of particles that vary as a function of size when moving in a gas, the most important of which is the increased sedimentation rate of large particles due to gravity. An alternative but parallel transition at the upper size limit is the point at which particles become too large to be efficiently inhalable (Vincent *et al.*, 1990; Hinds, 1999). Here the particle's Reynolds number (Re), which is the ratio of the resisting force of the viscous gas to the inertial force of the moving particle, separates the *Stokes regime* (with viscous forces ≫ inertial forces and $\mathrm{Re} < 1$) from the purely ballistic *Newton regime* (with viscous forces ≪ inertial forces and $\mathrm{Re} > 1000$), with a semiballistic *transition regime* in between ($1 < \mathrm{Re} < 1000$) (Hinds, 1999). Thus, Re quantifies to which degree the particles are prone to follow the air streams patterns, for instance, upon inhalation. Re is calculated through

$$\mathrm{Re} = \frac{\rho_g v_s D}{\eta}, \tag{1}$$

with the density of the gas ρ_g, which is the density of air here, the relative velocity between air and particle v_s, which is the settling velocity here, the particle diameter D, and the gas dynamic viscosity η, also for air here. For a spherical particle in the Stokes regime, v_s is calculated through

$$v_s = \frac{\rho_p D^2 g C_c}{18\eta},$$
$$\text{with} \quad C_c = 1 + \frac{\lambda}{D}\left[2.34 + 1.05\exp\left(-0.39\frac{D}{\lambda}\right)\right]$$
$$\text{for} \quad \mathrm{Re} < 1, \tag{2}$$

with the particle density ρ_p, the gravitational acceleration g, the Cunningham slip correction C_c, and the gas mean free path λ (Hinds, 1999). The Cunningham slip correction C_c matters primarily for particles with $D < 1$ μm and converges to unity for $D > 1$ μm. Note that the numerical factors used to obtain C_c (i.e., 2.34, 1.05, and −0.39) were taken from Hinds (1999), whereas the factors reported by Davies (1945) (i.e., 2.514, 0.800, and −0.55) are even more commonly used. For a spherical particle in the transition regime, v_s is calculated through

$$v_s = \left(\frac{4\rho_p D g}{3 C_D \rho_g}\right)^{1/2},$$
$$\text{with} \quad C_D = \frac{24}{\mathrm{Re}}\left(1 + 0.15\mathrm{Re}^{0.687}\right)$$
$$\text{for} \quad \mathrm{Re} > 1, \tag{3}$$

with the drag coefficient C_D. Re for water drops with $D < 80$ μm at room temperature is < 1, so for this size range using the Stokes drag would not result in significant errors. Note that the drag coefficient C_D in Eq. (3) is an empirical correction that depends upon v_s.

Within the Stokes regime and in quiescent or still air, v_s scales with D^2, spanning from essentially infinite airborne residence times for smaller particles (i.e., $D < 1$ μm) to finite settling velocities for large particles (Fig. 2). For example, for an exhalation at a height of 1.5 m a 5 μm particle settles out within ∼30 min, a 8 μm particle settles out within ∼10 min, and a 20 μm particle settles out within ∼2 min. In real-world settings, however, the air is typically not still, but rather influenced by air movement on different scales, including upward convection due to heating from bodies, so the particle residence time in the air of occupied rooms is usually much longer than in still air. The drag of the ambient air can extend particle residence times significantly (Milton, 2020; Bazant and Bush, 2021). For nonspherical particles, which may be relevant when particles are fully dried, Eq. (2) should be modified to take particle shape into account. If the particle shape does not considerably deviate from a sphere, especially at low Re, the errors are not significant when using Eq. (2) (Bagheri and Bonadonna, 2016).

Figure 2 shows that aerosol and droplet transmission routes cannot be strictly separated but exist in different size regimes

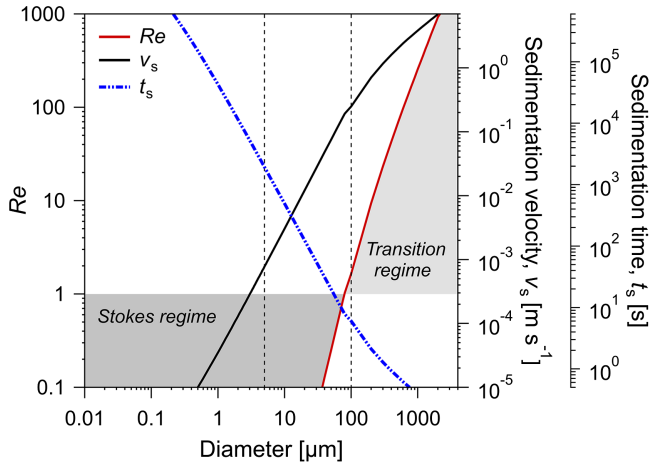

FIG. 2. Size dependence of the Reynolds number Re, settling velocity v_s, and sedimentation time from a height of 1.5 m t_s for spherical particles in still air. Gray shading highlights Stokes ($\mathrm{Re} < 1$) vs transition regimes ($1 < \mathrm{Re} < 1000$). Vertical dashed lines mark a frequently used threshold at 5 μm to separate large from small particles as well as a threshold at 100 μm, as proposed by Prather *et al.* (2020).

of a particle size and fluid mechanical continuum. The terminology used to separate the concepts of aerosol and droplet transmission often causes more confusion than clarity by introducing the false notion that droplets and aerosols are somehow fundamentally different. Bourouiba (2020) criticized the widely used and "overly simplified […] dichotomous classification between large vs small droplets [with] various arbitrary droplet diameter cutoffs, from 5 to 10 μm," which still underlies the current risk management, recommendations, and infection control. Bourouiba (2020) further proposed considering aerosol and droplet spray transmission as a multiphase turbulent cloud of buoyant hot and moist air that contains a continuous range of particle sizes. In this context, Prather *et al.* (2020) advocated that 100 μm would be a more appropriate threshold than the historically used 5 or 10 μm. All such clear-cut boundaries are simplifications of the physics involved. Nevertheless, here we adopt the threshold of 100 μm, like Prather *et al.* (2020). As later shown, this threshold includes the number-concentration maxima of the largest particles generated in the respiratory tract. Moreover, this is the largest particle size that can typically be inhaled, and thus provides a compelling practical benefit in terms of transmission pathways and mitigation strategies.

Concerning the composition of respiratory particles, we use the following terminology throughout the text: Mucosal fluids comprise a large group of liquid surface films (tear fluid, nasal mucus, bronchial mucus, gastric mucus, sweat, etc.) that cover different parts of the body or organ surfaces exposed to the external environment (Schenkels, Veerman, and Nieuw Amerongen, 1995; Bansil and Turner, 2006). These fluids typically have site-specific composition and fulfill a variety of specific functions. The following two mucosal fluids play an essential role in respiratory particle emission.

- *Saliva* is present in the oral cavity, where it is produced by different salivary glands (Schenkels, Veerman, and Nieuw Amerongen, 1995; Humphrey and Williamson, 2001).
- *Epithelial lining fluid (ELF)* covers the air-facing surfaces of the lower respiratory tract (LRT). Note that in addition to ELF, the terms respiratory tract lining fluid, airway surface liquid, and mucus are also widely used in the literature (Bansil and Turner, 2006). Here we restrict our use to the term ELF.

Further, we use the terms mucosalivary or mucosal films and fluids to refer to both ELF and saliva. An overview of the complex and variable composition of saliva and ELF is provided in Sec. II.C. The term respiratory particles here refers to emissions from both saliva and ELF.

B. Properties of respiratory particles

The following physicochemical aerosol properties matter most in the spread of disease.

- Particle number and volume concentration (Secs. II.B.1 and III.D)
- Particle number and volume size distribution (Secs. II.B.2 and III)
- Size-dependent distribution of pathogens in the respiratory carrier particle population (Secs. II.B.3 and III.E)
- Composition and hygroscopicity of the mucosalivary particles along with their desiccation and (re)humidification properties (Sec. II.C)

Further, physical and biochemical properties of the pathogens themselves play important roles, which are addressed only briefly in Sec. II.B.4. For further details, refer to the cited literature.

1. Particle number and volume concentrations and emission rates

The particle number N or volume V_p concentration C in an air volume V_{air} defines the overall abundance of exhaled (and potentially pathogen bearing) particles according to

$$C_N = \frac{N}{V_{air}}, \qquad C_V = \frac{V_p}{V_{air}}. \tag{4}$$

The particle emission rates Q are derived through

$$Q_N = Nf, \qquad Q_V = V_p f \tag{5}$$

as well as

$$Q_N = C_N \dot{V}, \qquad Q_V = C_V \dot{V} \tag{6}$$

with a given N and V_p, the rate f of a given respiratory event, and the air emission rate $\dot{V}$. Table I summarizes average parameters for respiratory events and specifies those values used in the calculations in this review. The particle source is highly variable in terms of strength and frequency. It spans from semicontinuous tidal breathing to short and intense events such as sneezing with a duration $\Delta t < 1$ s (Table I). The intersubject and intrasubject variability in C_N as a function of respiratory activity and physiological factors is remarkably high, spanning 2 to 3 orders of magnitude from $\sim$0.1 up to $\sim$100 cm^{-3} (Duguid, 1946; Morawska *et al.*, 2009; Xie *et al.*, 2009; Holmgren *et al.*, 2010; Schwarz *et al.*, 2015; Bake *et al.*, 2017; Asadi *et al.*, 2019; Gregson *et al.*, 2021). Note, however, that the experimental approaches and measurement size ranges also vary widely among studies in this context, which complicates comparability, as further addressed later in the review. C_N and Q_N can be converted into C_V and Q_V through

$$C_V = \frac{\pi}{6} D^3 C_N, \qquad Q_V = \frac{\pi}{6} D^3 Q_N \tag{7}$$

under the assumption that the particles have a nearly spherical shape.

Exhaled puffs of air are discontinuous, turbulent fluid volumes emitted from a point source (mouth or nose) and driven at first by momentum and subsequently by buoyancy (Bourouiba, 2021). The puffs are spatially heterogeneous due to mixing and dilution in turbulent eddies and variable water vapor and temperature fields (Ng *et al.*, 2021), which results in a decrease in C_N with distance from the source, and therefore makes analyses of measurements complicated to interpret (Gregson *et al.*, 2021). Note further that the C_N levels are typically much lower than ambient aerosol concentrations

TABLE I. Parameters of different respiratory activities and events summarized from previous studies. The following events are specified: breathe (event = one exhalation), speak (event = one spoken word of average length), cough (event = one cough), and sneeze (event = one sneeze). Relevant event-specific parameters are the emitted air volume V_{air}, duration Δt, and peak flow rate q per event. Relevant time-averaged parameters are the event rate f, which is the number of event repetitions per hour, and the average air emission rate $\dot{V}$ obtained through $\dot{V} = V_{air} f$ (Tortora and Derrickson, 2017). For speaking, two short words spoken per second were assumed to obtain a speaking-related f according to Johnson *et al.* (2011). Several parameters show an inherently high intersubject and intrasubject variability, which is reflected in the table as typical parameter ranges. The values in brackets show the characteristic values used in calculations in this review (such as those in Secs. III.D and III.E). The values represent the average of male and female adults. The values typically represent healthy subjects: only for the cough rate are healthy and diseased subjects distinguished.

	Properties per respiratory event			Time-averaged properties	
	Exhaled volume V_{air} (l)	Duration Δt (s)	Peak flow rate q ($l\,s^{-1}$)	Event rate f (h^{-1})	Air emission rate $\dot{V}$ ($l\,h^{-1}$)
Tidal breath	0.4–1.7[a,b,c,d] [0.5][k,h,l]	1.5–2.5[e,f] [2][k]	0.2–0.7[c,f,g]	600–1200[a,b,d] [720][h,k,l]	360–800[f,h,i,j] [360][*]
Spoken word	[0.1][*]	0.5[i]	0.3–1.6[f,m,n]	[7200][i]	450–920[f,i] [700][f,j]
Cough	0.3–4[a,g,i,k,l,o,p,q] [1.5][s]	0.2–1[a,g,k,q,r]	0.2–15[a,f,g,p,s,t]	Healthy: 0–4 [u,v,w] Healthy smoker: 0–8[v,w] Diseased: 0–140[l,u,v,w,x,y] [10][k]	[15][*]
Sneeze	1–4[k] [2][l]	0.1–0.2[k]	10–20[*]	5–30[k] [10][†]	[20][*]

[a] Ai and Melikov (2018).
[b] Gao *et al.* (2018).
[c] Holmgren *et al.* (2010).
[d] Levitzky (2017).
[e] Conrad and Schönle (1979).
[f] Gupta, Lin, and Chen (2010).
[g] Gupta, Lin, and Chen (2009).
[h] Tortora and Derrickson (2017).
[i] Johnson *et al.* (2011).
[j] Archer *et al.* (2022).
[k] Bourouiba (2021).
[l] Patterson and Wood (2019).
[m] Abkarian *et al.* (2020).
[n] Chi *et al.* (2015).
[o] Chao *et al.* (2009).
[p] Lee *et al.* (2019).
[q] Wei and Li (2017).
[r] Ren *et al.* (2020).
[s] Ren *et al.* (2020).
[t] Yang *et al.* (2007).
[u] Sinha *et al.* (2016).
[v] Sumner *et al.* (2013).
[w] Yousaf *et al.* (2013).
[x] Patterson *et al.* (2018).
[y] Sunger *et al.* (2013).
[*] Calculated through $\dot{V} = V_{air} f$.
[†] Sparse literature, values adopted from coughing.

(both indoor and outdoor), which typically range from a few hundred to a few thousand particles per cm^3 (Vette *et al.*, 2001; Riley *et al.*, 2002; Andreae, 2009). This imposes further experimental challenges since the ambient background aerosol must be either removed (i.e., filtration) or carefully characterized (i.e., background subtraction) (Gregson *et al.*, 2022). Even in a clean-room environment, however, it is challenging to detect the influence of respiratory aerosols on top of existing particle concentrations. For a comparison of respiration C_N levels from different studies, it is essential to specify the measurement size range, as most instruments or techniques cover only a limited band of the overall relevant size distribution; see Table IV. Thus, most reported number concentrations account not for the total C_N but rather for a subset within a certain size range determined by the instruments' specifications. As one result of the parametrization of particle size distributions presented in this study, Sec. III.D presents a statistical summary of measured particle number and volume concentrations as well as emission rates in relation to respiratory activities.

2. Particle number and volume size distributions

The initial PSD immediately following emission depends on the formation mechanisms and sites within the respiratory tract (Sec. II.D) (Johnson and Morawska, 2009; Morawska *et al.*, 2009; Johnson *et al.*, 2011; Asadi *et al.*, 2019; Bagheri *et al.*, 2023). After emission and rapid evaporation (Sec. II.C), the PSD determines the particles' mobility and deposition rates (Bourouiba, Dehandschoewercker, and Bush, 2014; Cummins *et al.*, 2020; Ng *et al.*, 2021). Typically the interaction of deposition and ventilation rates defines the residence time of the particles in the air (Lai, 2002; Riley *et al.*, 2002; Li *et al.*, 2007; Nazaroff, 2016; Helleis, Klimach, and Pöschl, 2021; McNeill, 2022). The particle movement and transport through air is driven by multiple forces, such as drag, inertial, electrostatic, radiative, gravitational, and thermophoretic forces, as well as Brownian motion and turbulent diffusion (Hinds, 1999; Lai, 2002; Riley *et al.*, 2002; Li *et al.*, 2007; Kulkarni, Baron, and Willeke, 2011; Nazaroff, 2016; Jayaweera *et al.*, 2020). The influence of these forces strongly depends on the PSD, and thus affects transport over distances as well as either dilution or potential enrichment under given air conditions (Wells, 1934; Abkarian *et al.*, 2020; Mittal, Meneveau, and Wu, 2020; Yang *et al.*, 2020; Liu *et al.*, 2021). Moreover, the PSD defines the filtration efficiency of face masks (upon both inhalation and exhalation) as well as the deposition sites of particles in the upper respiratory tract (URT) and LRT; see also Fig. 8 (Drewnick *et al.*, 2021; Bagheri *et al.*, 2023).

The respiration PSDs have a characteristic multimodal shape (Papineni and Rosenthal, 1997; Chao *et al.*, 2009; Morawska *et al.*, 2009; Johnson *et al.*, 2011; Han, Weng, and Huang, 2013; Asadi *et al.*, 2019; Bagheri *et al.*, 2023). They can be described well by a multimode log-normal fit function with n individual modes (i) according to

$$f_N(D) = \sum_{i=1}^{n} A_i \exp\left\{-\left[\frac{\ln(D/D_i)}{\sigma_i}\right]^2\right\}, \tag{8}$$

with D the particle diameter, D_i the mode mean geometric diameter, A_i the number concentration at D_i, and σ_i the modal geometric standard deviation that defines the mode width (Seinfeld and Pandis, 2016). In this review, $f_N(D)$ is given as $dN/d\log D$, which is broadly established in aerosol science. Thus, Eq. (8) uses both log and ln. To convert uniformly to log (if preferred), $\ln(D/D_i)$ can be replaced by $2.303\ \log(D/D_i)$ to make the equation uniform. For the multimodal log-normal fitting, the smallest possible number of modes yielding a good representation of the experimental data is preferred. Ideally the individual modes can be associated with the mechanisms and sites of specific emission processes in the respiratory tract. Equation (8) is used throughout this review and in the parametrization present here. Note that different versions of log-normal fit functions have been broadly used in aerosol studies, particularly in the field of respiratory aerosols. As an alternative example, the following equation, which is from Heintzenberg (1994), has been widely used (Chao *et al.*, 2009; Morawska *et al.*, 2009; Johnson *et al.*, 2011; Han, Weng, and Huang, 2013; Asadi *et al.*, 2019):

$$f_H(D) = \sum_{i=1}^{n} \frac{C_i}{\sqrt{2\pi}\ln(\sigma_i)} \exp\left\{-\left[\frac{\ln(D/D_i)}{\sqrt{2}\ln(\sigma_i)}\right]^2\right\}, \tag{9}$$

with D_i the mode mean geometric diameter, as in Eq. (8), C_i the integral particle number concentration of the mode, and σ_i the modal geometric standard deviation. Note that Eqs. (8) and (9) yield the same fitting results. They differ only in the definition or meaning of the fit parameters.

Essentially all measurements of respiratory aerosols yield particle number size distributions (NSDs) as primary data (i.e., the number of counted particles in a given sequence of size bins). The NSDs can be converted to size distributions of the number emission rates (Q_N) according to Eq. (5) and f in Table I. Further, the NSDs can be converted to particle volume size distributions (VSDs) according to

$$\begin{aligned} f_V(D) &= \frac{\pi}{6} D^3 f_N(D) \\ &= \frac{\pi}{6} D^3 \sum_{i=1}^{n} A_i \exp\left\{-\left[\frac{\ln(D/D_i)}{\sigma_i}\right]^2\right\} \end{aligned} \tag{10}$$

assuming a nearly spherical particle shape.

Inconsistencies and deviations in the PSDs reported in the published literature can presumably be explained by the highly dynamic properties of the respiratory particle population, along with experimental challenges in its characterization (Nicas, Nazaroff, and Hubbard, 2005; Xie *et al.*, 2009; Johnson *et al.*, 2011; Bagheri *et al.*, 2023). Moreover, many different measurement techniques have been used, each of which can detect aerosol particles over a narrow band of the overall PSD. To construct a PSD over the full range of particle sizes emitted by human respiration (< 10 nm to > 1000 μm) requires data from a set of instruments ideally with overlapping detection range to be stitched together, each of which may use different physical parameters for detection (i.e., optical, aerodynamic, geometrical, or electric mobility sizing). The matching of PSDs using these different techniques introduces additional uncertainties to be considered in the interpretation of those measurements (Seinfeld and Pandis, 2016). Section III follows up on this general overview of respiratory particle NSDs and VSDs with a comprehensive summary of the available literature and the development of an efficient parametrization scheme, representing their characteristic multimodal shape.

3. Size distributions of pathogens within respiratory particle populations

The mixing state of pathogens and "carrier" particles relates to the quantity of pathogens distributed across the mucusalivary particle population and the questions as to whether and in which particle size range the pathogens are embedded (Riemer *et al.*, 2019). These aspects are relevant for a mechanistic understanding of the pathogens' aerosolization, transport, and deposition (Gralton *et al.*, 2011; Fennelly, 2020; Zuo, Uspal, and Wei, 2020). Small pathogens such as viruses are generally not emitted alone, but rather embedded within much larger mucusalivary particles (Fig. 3) (Lindsley *et al.*, 2010a; Vejerano and Marr, 2018). At the same time and for typical

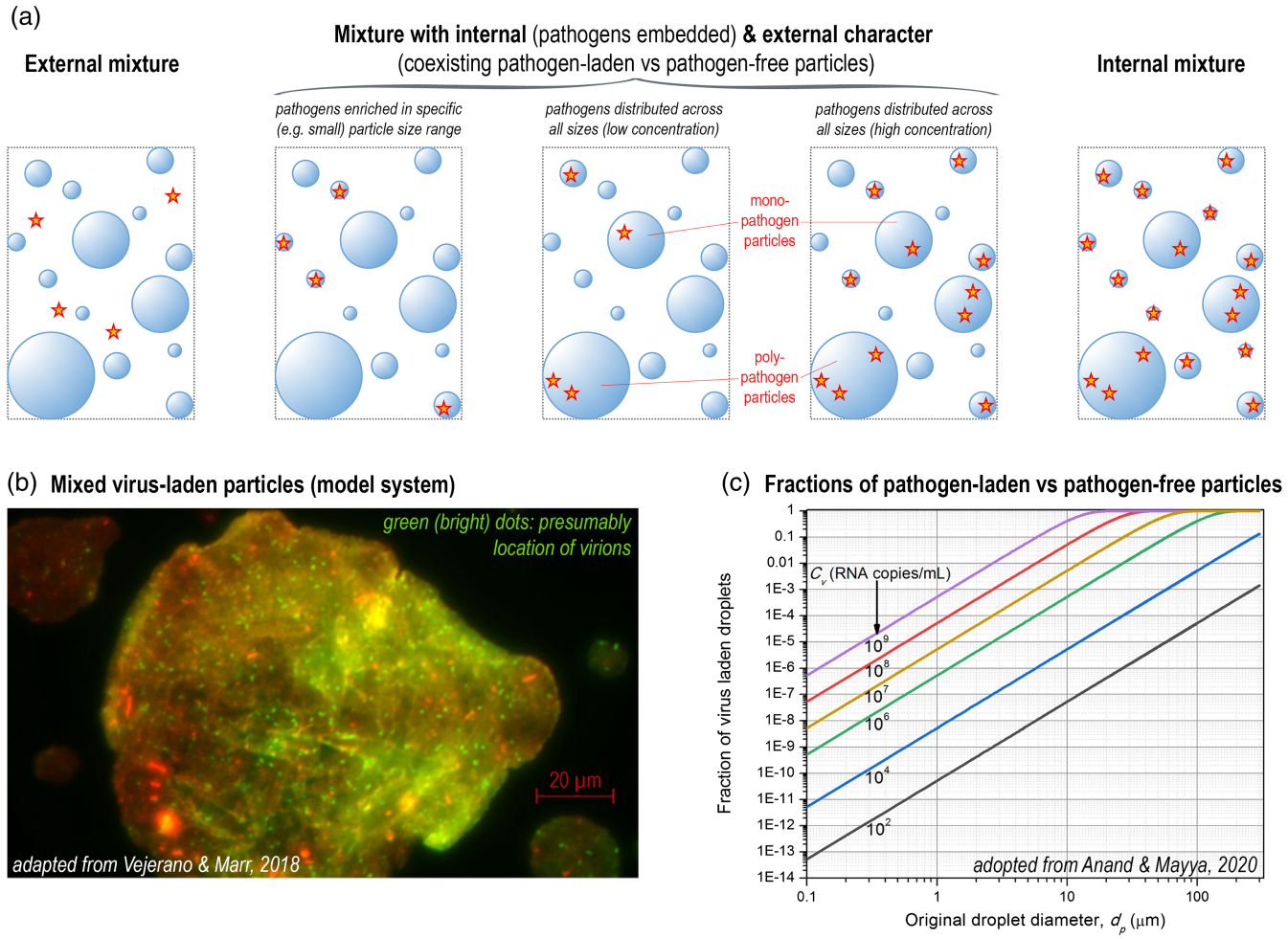

FIG. 3. Internal vs external mixing states in relation to pathogens and mucusalivary carrier particles. (a) Scheme of ideal cases of internal vs external respiratory particle populations as well as intermediate states with both internal and external character. The latter case likely represents pathogen-laden aerosols. Further emphasized is the difference between mono- and poly-pathogen particles (Nordsiek, Bodenschatz, and Bagheri, 2021). (b) Microscopy image showing laboratory-generated virus-laden and internally mixed particles as surrogates for authentic respiratory particles comprising salt, glycoprotein, surfactant, and the well-studied *Pseudomonas* ϕ6 virions. Green fluorescence is associated with surfactants, which are assumed to partition to the ϕ6 virions. Adapted from Vejerano and Marr, 2018. (c) Fraction of pathogen-laden particles as a function of particle size and pathogen load of the fluids in the respiratory tract based on calculations suggesting that highly variable fractions of pathogen-laden vs pathogen-free particles coexist. Adapted from Anand and Mayya, 2020.

pathogen concentrations in respiratory fluids [up to about 10^9 ml^{-1} (Fajnzylber *et al.*, 2020; van Kampen *et al.*, 2021)], only a certain fraction of the carrier particles are pathogen laden, whereas the rest is pathogen free (Anand and Mayya, 2020). From this perspective, the pathogen-mucusalivary aerosol is neither completely internally nor completely externally mixed. It can be regarded as internally mixed in the sense that the pathogens are embedded within mucusalivary particles and as externally mixed, in the sense that the pathogen-laden particle fraction is likely small in most cases such that pathogen-laden and pathogen-free particles coexist (Anand and Mayya, 2020). Note, however, that published data on the pathogen mixing state is sparse and microphysical details are widely unknown. For example, it is unknown whether small pathogens such as virions are located within the carrier particles or on their surface, which may be relevant for their exposure to environmental conditions and thus their viability (Vejerano and Marr, 2018; Pan *et al.*, 2019; Huynh *et al.*, 2022). It is further unknown to what extent respiratory particles hold one or more pathogen copies (mono- versus poly-pathogen particles), which has implications for the assessment of infection risks (Anand and Mayya, 2020; Nordsiek, Bodenschatz, and Bagheri, 2021).

The likelihood that an emitted particle contains a pathogen increases with particle size (Anand and Mayya, 2020). At particularly high pathogen concentrations in respiratory fluids, one could expect more than one pathogen to occur per particle, with a probability that increases with particle size. Accordingly, the dose response might also scale with the cumulative particle volume (Fig. 3). If instead the pathogens were embedded with a relatively constant number of virions in a particular (for instance, smaller) particle size fraction, the dose response would likely rather scale with the number of inhaled particles in this specific size range (for instance,

a specific mode of the PSD). Size-resolved sampling and detection of airborne pathogens from infected individuals, which allows important conclusions on the mixing state, is, however, experimentally demanding and corresponding studies are therefore rare (Roy and Milton, 2004). The existing studies, especially those on *M. tuberculosis* (Fennelly, Martyny *et al.*, 2004; Fennelly *et al.*, 2012; Patterson *et al.*, 2018), the influenza virus (Fabian *et al.*, 2008; Lindsley *et al.*, 2012; Lednicky and Loeb, 2013; Milton *et al.*, 2013; Fennelly, 2020; Li, Niu, and Zhu, 2021), and SARS-CoV-2 (Chia *et al.*, 2020; Liu *et al.*, 2020; Lednicky *et al.*, 2021; Santarpia *et al.*, 2022), suggest that pathogens are typically enriched in specific size ranges of the carrier PSD, likely defined by the particle formation mechanisms and sites in relation to the site of infection; see Sec. II.D. Furthermore, PSDs combined with the pathogen number density in mucusalivary particles determines the infection risk associated with multipathogen aerosols, which was recently addressed in an extended dose-response model (Nordsiek, Bodenschatz, and Bagheri, 2021). Nevertheless, the occurrence and relevance of multipathogen particles are still uncertain.

Beyond the actually inhaled dose, the mixing state is also important for the dose-response relationship of a given pathogen. Specifically, the size range and deposition properties of the mucusalivary particles that actually carry most of the pathogens defines which regions of the URT and LRT are reached. Note that the pathogen load does not necessarily scale with particle volume across the entire size range because of the rather complicated interaction of different formation mechanisms and sites (Sec. II.D). This is supported by experimental evidence showing high pathogen loads in comparatively small particle size fractions (Sec. III.E); however, biases due to the difficulty of sampling larger particles should not be ruled out. As different deposition sites in the respiratory tract can show different susceptibilities to a given pathogen, the dose response can be size dependent in terms of the inhaled PSD (Thomas, 2013; Teske *et al.*, 2014; Fennelly, 2020). Previous studies have reported experimental evidence of a higher severity, morbidity and fatality for small pathogen-laden particles that can reach the LRT in contrast to large particles that mostly deposit in the URT (Thomas, 2013). Specifically, such effects have been reported for influenza virions (e.g., Alford *et al.*, 1966; Little *et al.*, 1979; Snyder *et al.*, 1986), *M. tuberculosis* (Sonkin, 1951; Wells, 1955), and other pathogens (Druett *et al.*, 1953; Druett, Henderson, and Peacock, 1956; Thomas *et al.*, 2009). In this sense large carrier particles may be more infectious, as they are prone to contain larger pathogen loads, whereas smaller carrier particles may be more harmful, as the contained pathogens are more prone to penetrate deeper into the respiratory tract, depending on the pathogen. Milton (2012) introduced the concept of *anisotropic infection*, emphasizing that the clinical severity of certain disease depends on the mode of acquisition. This means that differences in the size-dependent pathogen deposition site in the respiratory tract or disease acquisition modes including contact can be associated with dramatic differences in disease development, ranging from an acute disease response to a much milder course.

4. Decay of pathogen viability in aerosol

Another essential parameter in disease transmission through the aerosol route is the survival of the corresponding pathogens during airborne transport. The decline in the pathogen's viability defines the lifetime of its infectious potential upon airborne transport and must be considered in infection control measures and risk assessments. The inactivation typically follows a first-order exponential decay function

$$N_p(t) = N_{p,0} \exp(-kt), \tag{11}$$

with $N_p(t)$ the number of airborne and viable pathogens at a given time t, $N_{p,0}$ the initial number of viable pathogens at $t = 0$, and k the inactivation rate, which further gives the half-life as $T_{1/2} = \ln(2/k)$ (Knibbs *et al.*, 2014; Hitchman, 2020). Various environmental factors, such as temperature, desiccation at low humidity, radiation (i.e., ultraviolet light), and reactive gaseous species can damage the pathogens' lipids, proteins, or nucleic acids and inactivate them (Pica and Bouvier, 2012; Fennelly, 2020; Dabisch *et al.*, 2021; Leung, 2021; Niazi, Groth, Spann, and Johnson, 2021). An overview of the effects of temperature and humidity on pathogen viability was provided by Tang (2009). The pathogen viability may further depend on the chemical microenvironment, and thus on ELF and saliva composition as well as water content, though knowledge in this context has remained incomplete (Vejerano and Marr, 2018; Niazi, Groth, Spann, and Johnson, 2021). After droplet desiccation, for example, ELF and saliva can potentially act as an organic barrier against environmental exposures such as sunlight and atmospheric oxidants (Oswin *et al.*, 2022). Such effects might be particularly relevant if drying transforms the organic constituents into a highly viscous or even glassy phase that slows down or even inhibits the diffusion of reactants (Berkemeier *et al.*, 2016; Huynh *et al.*, 2022). Typical half-lives $T_{1/2}$ for selected pathogens in aerosol are summarized in Table II. For the noteworthy studies in the table, the variability in $T_{1/2}$ is large, and strongly enhanced decay rates were found for increased temperature and irradiance (Schuit *et al.*, 2020; Dabisch *et al.*, 2021). For SARS-CoV-2, the decrease in ambient relative humidity (RH) has been shown to decrease viability of the virus, and after 20 min viability drops to about ∼20%, regardless of the RH (within the 40%–90% RH range studied) (Oswin *et al.*, 2022).

C. Hygroscopic growth and shrinkage of respiratory particles in relation to their chemical composition and hygroscopicity

The composition of the exhaled mucosal fluid droplets is complex, highly variable, and not well characterized (Sarkar, Xu, and Lee, 2019; Niazi, Groth, Spann, and Johnson, 2021). In the respiratory tract, and thus also in freshly emitted droplets, the fluids contain large mass fractions of water with $> 99\%$ in saliva (Humphrey and Williamson, 2001) and ∼95% in ELF (Bansil and Turner, 2006; Hamed and Fiegel, 2014). Dissolved in the water are various salts acting as electrolytes and buffers with sodium (Na^+), potassium (K^+), and calcium (Ca^{2+}) as main cations, as well as

TABLE II. Summary of experimentally determined half-lives ($T_{1/2}$) in the exponential decay of pathogen viability in aerosol. The wide range of "typical" timescales involved in pathogen viability and their dependence on environmental factors by means of selected studies are illustrated. The table does not provide a comprehensive overview of the published literature. Temperature (θ), relative humidity (RH), and irradiance (E, integrated ultraviolet B radiation) are specified as important environmental factors. $T_{1/2}$ values in parentheses represent confidence intervals. Where E is not specified, experiments were (presumably) conducted in the dark.

		Conditions			
Pathogen (type of carrier particles)	$T_{1/2}$ (min)	θ (°C)	RH (%)	E (W m^{-2})	Reference
Human coronavirus 229E	200 ± 10	20 ± 1	80 ± 5	···	Ijaz *et al.* (1985)
	4040 ± 494	20 ± 1	50 ± 5	···	
	1605 ± 373	20 ± 1	30 ± 5	···	
M. tuberculosis, *M. avium*, and *M. intracellulare*	7.5 (6–9)[a]	24 ± 2	74 ± 3		Lever, Williams, and Bennett (2000)
Mycobacterium tuberculosis	90	20–25	60–70	···	Pfrommer *et al.* (2020)
Pseudomonas aeruginosa	50 (30–151)	···	···	···	Knibbs *et al.* (2014)
Influenza A (i.e., H1N1, H5N1, and H3N2)	15–90	25	55	···	Pyankov, Pyankova, and Agranovski (2012)
Influenza A (i.e., H1N1)	∼32	20	20–70	0	Schuit *et al.* (2020)
	∼2	20	20–70	1.44	
MERS-CoV	> 70	25	79	···	Pyankov *et al.* (2018)
	∼24	38	24	···	
SARS-CoV-1	72 (47–146)	23	40	···	van Doremalen *et al.* (2020)
SARS-CoV-2	66 (38–158)	23	40	···	van Doremalen *et al.* (2020)
SARS-CoV-2	> 960[b]	25 ± 2	53 ± 11	···	Fears *et al.* (2020)
SARS-CoV-2	30–177	19–22	40–88	···	Smither *et al.* (2020)
SARS-CoV-2	10– > 100	10–40	20–70	0	Dabisch *et al.* (2021)
	3–5	10–30	45	0.9	
	1–3	10–40	20–70	1.9	
SARS-CoV-2 (in cell culture media)	3.5 (2–12)[c]	18–21	40	···	Oswin *et al.* (2022)
	5 (3–10)	18–21	90	···	

[a]All data points from this study were fitted jointly with exponential decay function to obtain the average half-life (with values for a 95% confidence interval) shown here.
[b]This value is based on one measurement only.
[c]Data were digitized from a figure and fitted with an exponential decay function to obtain the average half-life (with values for 90% confidence interval) shown here.

chloride (Cl^-), hydrogen carbonate (HCO_3^-), and phosphates (mainly $H_2PO_4^-$ and HPO_4^{2-}) as major anions; see Table III. Further, a broad variety of organic constituents are either dissolved or suspended in the water. This includes proteins for defensive purposes (such as lysozyme and immunoglobulins), glycoproteins responsible for the viscous and elastic gel-like properties of the fluids (i.e., mucins), as well as further compounds such as lipids, surfactants (i.e., phospholipids), cholesterol, and urea (Bansil and Turner, 2006). For instance, Bredberg *et al.* (2012) detected more than 100 different proteins in exhaled particle samples. Further, the ELF composition changes from the upper conducting airways toward the alveolar region (Cross *et al.*, 1994; van der Vliet and Cross, 2000; Holmgren *et al.*, 2011; Lakey *et al.*, 2016; Niazi, Groth, Spann, and Johnson, 2021). Table III provides a general overview of the main constituents and specifies typical concentration ranges. However, it does not seek to resolve the entire chemical complexity or variability of the fluids.

The life cycle of the respiratory particles is dynamic. Martin (2000) summarized the underlying general physical principles and behavior for atmospheric particles that can also presumably be extrapolated in large parts to respiratory aerosols. At the moment of exhalation, the particles are in a liquid state and can be regarded as droplets of mucosal fluids. The warm (∼37 °C), water-saturated (∼100% RH), and particle-laden air leaves the respiratory tract and typically experiences sudden changes in temperature and RH (Wells, 1934; Duguid, 1946; Liu *et al.*, 2017; Chaudhuri *et al.*, 2020; Chong *et al.*, 2021; Ng *et al.*, 2021). A frequent scenario is exhalation into subsaturated water vapor conditions (i.e., RH < 100%), such as room air at typically 40% to 80% RH (Chao *et al.*, 2009; Morawska *et al.*, 2009; Drossinos and Stilianakis, 2020; Davies *et al.*, 2021). Under these conditions, the particles leave the respiratory tract at RH ≈ 100% with an initial diameter D_{exh}. In relation to the particle composition and the associated hygroscopicity, evaporation of water occurs quickly (i.e., < 1 s) and causes a substantial decrease in D (Wei and Li, 2015; Marr *et al.*, 2019; Chaudhuri, Basu, and Saha, 2020; Davies *et al.*, 2021). For complete evaporation, the droplets shrink completely to their dry diameter D_{dry}, which is defined by the remaining nonvolatile solutes, whereas at typical intermediate RH levels the droplets shrink to an equilibrium wet diameter (D_{wet}) (Nicas, Nazaroff, and Hubbard, 2005; Morawska *et al.*, 2009; Holmgren *et al.*, 2011). The ratio of the wet diameter as a function of RH $D_{wet}(RH)$ and the dry diameter D_{dry} defines the particles' growth factor g_d as

$$g_d = \frac{D_{wet}(RH)}{D_{dry}}. \quad (12)$$

TABLE III. Overview of the main constituents in saliva and ELF. The range of typical mass concentrations β, in mg per 100 ml, are specified as reported in the literature. For saliva, the cited studies often compared concentrations under resting vs stimulated conditions, which are both implemented here. The values in brackets represent the best-guess values based on the most robust studies (in our view) or means for values with low data coverage. Empty cells indicate species for which no robust concentrations were found in the literature.

Constituent	Saliva β (mg dl^{-1})	ELF β (mg dl^{-1})
	Inorganic	
Ca	2–11 [6][a,b,c,d,e,f]	
Cl	30–130 [70][b,c,d]	250–326[g,h]
HCO_3^-	6–220 [85][b,c,d]	150–230[h]
K	51–130 [66][b,c,d,e,f,i]	51–94[h]
Mg	0.1–1.2[a,c,j]	
Na	0–130 [39][b,c,d,e,f,i]	190–237[g,h]
Phosphates	20–220 [34][b,c,d,j]	
	Organic	
Glutathion	≤ 0.1[k,l]	3–5[m,n,o]
Lactate	1–50 [12][d]	
Lipids	1.4–3[j,p]	489–1204 [762]*
Cholesterol	0.13–50 [8][e,p]	9–14 [12][m]
Phospholipids	< 0.1[p]	480–1190 [750][m,q,r]
DPPC		330[q,r]
Proteins	128–640[b,i,s,t] [220][e,f,w,x]	470–1290[o,u,v] [1000]
Albumin	8–50 [20][s,w,y,z]	290–730[h,v]
Amylase	5–121 [38][e,s]	0[aa]
IgA	3–19[i,s,w,bb]	4–140[m,n,v]
IgG	1.1–1.4[w,bb]	56–260[m,n,v,cc]
IgM	0.21–0.48[w,bb]	1.3–10[m,v]
Lysozyme	10–22[e,w]	3–250[m,n,dd]
Mucins	6–55 [23][s,ff]	∼1[ee]
Transferrin	0.3–1.2[x]	30–170 [105][m,cc]
SP-A	< 0.1[gg]	1.9–41 [31][q,u]
SP-B	< 0.1[gg]	34–120 [77][q]
Urate	0.5–21 [2][e]	1.6–3.5[m,n,o,hh]
Urea	12–70 [30][e,t,z]	27[t]

[a] Ben-Aryeh *et al.* (1986).
[b] Dawes (1969).
[c] Dawes (1974).
[d] Dawes and Dong (1995).
[e] Kumar *et al.* (2017).
[f] Sarkar, Xu, and Lee (2019).
[g] Jayaraman *et al.* (2001).
[h] Knowles *et al.* (1997).
[i] Ben-Aryeh *et al.* (1990).
[j] Renke (2016).
[k] Dauletbaev (2001).
[l] Iwasaki *et al.* (2006).
[m] Bicer (2014).
[n] Hatch (1992).
[o] van der Vliet *et al.* (1999).
[p] Larsson, Olivecrona, and Ericson (1996).
[q] Hull *et al.* (1997).
[r] Veldhuizen *et al.* (1998).
[s] Cheaib and Lussi (2013).
[t] Dwyer (2004).
[u] Dargaville, South, and McDougall (1999).
[v] Sutinen *et al.* (1995).
[w] Rantonen and Meurman (2000).
[x] Suh, Kim, and Kho (2009).
[y] Henskens *et al.* (1993).
[z] Meurman *et al.* (2002).
[aa] Bredberg *et al.* (2012).
[bb] Brandtzaeg (1998).
[cc] Rennard *et al.* (1990).
[dd] Thompson *et al.* (1990).
[ee] Henderson *et al.* (2014).
[ff] Kang, Lee, and Kho (2018).
[gg] Schicht *et al.* (2015).
[hh] Slade *et al.* (1993).
*Calculated sum of cholesterol and phospholipids. DPPC, dipalmitoylphosphatidylcholine; Ig, immunoglobulin; SP, surfactant protein

The cube of g_d gives the volume growth factor (g_V) through $g_V = g_d^3$. Under certain conditions, such as during mixing of the respiratory puff with cold and humid outdoor air, supersaturated water vapor conditions (i.e., RH > 100%) can occur (Chong *et al.*, 2021; Ng *et al.*, 2021). An everyday situation that illustrates this effect is the appearance of one's own breath when breathing out into cold winter air. Here condensation of moisture in the rapidly cooling exhaled air onto ambient aerosol particles occurs. Such a supersaturation can cause an initial and significant growth of the droplets, as later outlined in more detail.

Figure 4 illustrates the drying process for saliva proxy droplets consisting of an aqueous mixture of salts and protein.[1] This shows that the droplets, after emission from the respiratory tract with RH ≈ 100% into an environment with RH < 100%, shrink substantially in the initial phase of drying. The shrinkage curve in Fig. 4(a) represents thermodynamic equilibrium states; however, particles might deviate from the equilibrium curve if changes in RH are rapid. A droplet's evaporation time is roughly proportional to D_{exh}^2 (Langmuir, 1918; Wells, 1934; Wells and Wells, 1936; Seinfeld and Pandis, 2016) according to

$$D(t)^2 = D_{exh}^2 + \frac{8 D_g M_w}{\rho_w}(c_g - c_{gs})t, \tag{13}$$

in which D_g is the diffusion coefficient of water in the gas phase, M_w is the molar mass of water, and ρ_w is the density of water. Note that this classical so-called D^2 law is based on the assumption of isolated, pure liquid droplets evaporating into a homogeneous environment of a given RH Chong *et al.* (2021) and holds for multicomponent mixtures only in the early stages

[1] Saliva proxy comprises salts NaCl and KCl and protein bovine serum albumin (BSA) with volume fractions $\epsilon_{NaCl} = 0.1$, $\epsilon_{KCl} = 0.1$, and $\epsilon_{BSA} = 0.8$. BSA was chosen as proxy protein for a complex protein mixture in real saliva; compare to Table III.

of the evaporation process, when the difference between far-surface water concentration and near-surface water concentration $(c_g - c_{gs})$ is approximately constant (Kulmala, Vesala, and Wagner, 1993; Niimura and Hasegawa, 2019).

The drying dynamics of saliva proxy particles are illustrated in Fig. 4(b) using calculations with the kinetic multilayer model of gas-particle interactions in aerosols and clouds, KM-GAP (Shiraiwa *et al.*, 2012). Processes limiting particle evaporation are the gas-phase diffusion of water molecules away from the particle surface, heat transfer to the particle surface after evaporational cooling, and, potentially, bulk diffusion of water molecules through the partially dried-out salt-protein matrix. While small particles equilibrate on the millisecond timescale, large particles may take seconds to reach thermodynamic equilibrium, especially if the diffusion of water through the salt-protein matrix is slow.

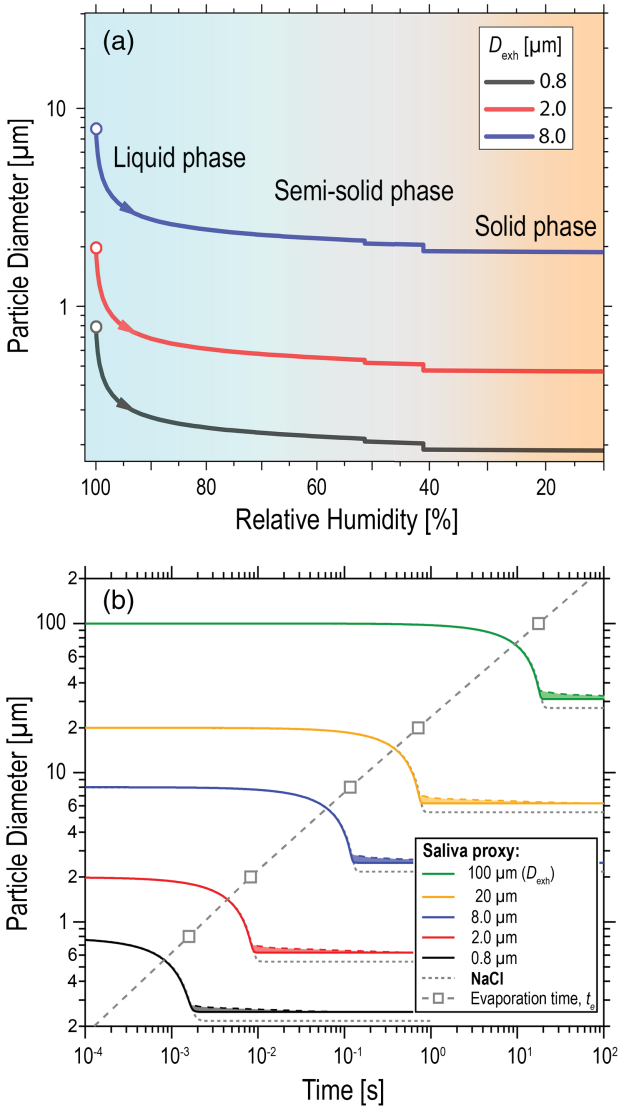

FIG. 4. Drying of saliva proxy droplets consisting of aqueous NaCl, KCl, and protein (BSA) with dry volume fractions of $\epsilon_{NaCl} = 0.1$, $\epsilon_{KCl} = 0.1$, and $\epsilon_{BSA} = 0.8$. (a) Thermodynamic modeling. Equilibrium diameters were plotted against relative humidity (RH) while assuming different initial diameters D_{exh} (open circles) upon exhalation at 100% RH. Steps near 50% and 40% RH correspond to efflorescence phase transitions of NaCl and KCl, respectively. (b) Kinetic modeling. Droplet diameters were plotted against time while assuming different initial diameters D_{exh} upon exhalation at 99.5% RH into an environment at 55% RH. Solid colored lines represent saliva proxy droplets, with shadings indicating uncertainties related to different diffusivity parametrizations for a semisolid phase state with $\lesssim$80% RH. The dotted gray lines represent aqueous NaCl droplets for comparison. The gray squares and the dashed gray line represent the characteristic time of evaporation t_e (e-folding time) plotted as a function of the initial particle diameter D_{exh}.

The shadings in Fig. 4(b) illustrate the minor effect of three different diffusivity parametrizations ranging from fully liquid particles to particles undergoing a liquid-to-semisolid phase transition and a significant drop in water diffusivity between 75% and 80% RH.[2] A Vignes-type mixing rule between liquid water and a semisolid salt-protein matrix yielded near-identical results to the fully liquid scenario.

The gray dotted lines in Fig. 4(b) show the corresponding drying dynamics of pure NaCl solution droplets, as shown previously and in good agreement with other modeling approaches (Davies *et al.*, 2021). The KM-GAP model returns near-identical evaporation speeds for saliva proxy and NaCl particles.[3] Owing to the consumption of latent heat during evaporation, particles cool to a minimum temperature of ~291.7 K irrespective of initial particle size. This temperature lies close to the wet bulb temperature, which is the lower limit at which net evaporation can still take place under the given ambient conditions.

The gray squares and dashed gray line in Fig. 4(b) represent the characteristic e-folding time of evaporation t_e, which is the time needed for a droplet to shrink by a factor of $1/e$ relative to its initial size D_{exh},

$$t_e = D_{exh}^2 \frac{(e^{-2} - 1)\rho_w}{8 D_g M_w (c_g - c_{gs})}. \tag{14}$$

Equation (14) exhibits a D^2 dependence analogous to the droplet evaporation rate [Eq. (13)], which applies as long as the evaporation kinetics are governed by gas diffusion (rather than bulk diffusion or phase transitions).

A comparison of these evaporation times with the sedimentation times of larger respiratory droplets (as shown in Fig. 2) reveals that the largest droplets (i.e., those that are

[2]Diffusivity parametrizations employed for the calculations in this study include (i) a constant diffusivity of water that would be expected in pure liquid water droplets $D_w = 1 \times 10^{-5}$ cm^2 s^{-1} [the lower boundaries in Fig. 4(b)]; (ii) a Vignes-type mixing rule (Vignes, 1966) $D_w = D_{w,w}^{x_w} D_{w,s}^{1-x_w}$ between pure liquid water diffusing at $D_{w,w} = 1 \times 10^{-5}$ cm^2 s^{-1} and water in a semisolid salt-protein matrix diffusing at $D_{w,s} = 1 \times 10^{-10}$ cm^2 s^{-1} [the solid lines in Fig. 4(b)]; (iii) percolation theory (Shante and Kirkpatrick, 1971; Murata, Lee, and Tanioka, 1999; Shiraiwa *et al.*, 2011) assuming a coordination number of $Z = 4$, a packing fraction $f = 0.95$, and values for $D_{w,w}$ and $D_{w,s}$, as previously defined [the upper boundaries in Fig. 4(b)].

[3]Water activity parametrizations for NaCl particles were obtained using the extended aerosol inorganics model (Clegg, Brimblecombe, and Wexler, 1998), and water activity in saliva particles was parametrized according to the ZSR model presented in Fig. 5(b).

~100 μm and larger) may settle too fast to reach an equilibrium state with the ambient RH (Nicas, Nazaroff, and Hubbard, 2005; Wei and Li, 2015; Ai and Melikov, 2018; Niazi, Groth, Spann, and Johnson, 2021) and can stay in a water-rich state over their entire lifetime. Chong *et al.* (2021) further showed that the influence of the local RH field around the droplets in the exhaled humid puffs has to be considered, as it tends to delay the evaporation significantly (i.e., a factor of 30 or even larger). In this sense, the calculations in Fig. 4(b) (assuming an instantaneous change in environment RH to 55%) represent lower limits of the evaporation times (or upper limits for the equilibration rate or speed) of characteristic droplet sizes without the influence of the surrounding puff of humid exhalation air (de Rivas and Villermaux, 2016; Villermaux *et al.*, 2017).

Figure 4(a) suggests a shrinkage factor of $D_{\mathrm{exh}}/D_{\mathrm{dry}} \approx 4.5$ for complete drying of saliva as well as $D_{\mathrm{exh}}/D_{\mathrm{wet}} \approx 4$ for drying to typical room RH levels (i.e., ~40% to ~80% RH). This is consistent with the shrinkage expected based on typical salt concentrations in saliva (Table III): the drying of a saline solution with ~1% NaCl [a typical value for saliva, from Humphrey and Williamson (2001)] would result in $g_{\mathrm{d}} \approx 6$. In previous experimental (Duguid, 1946; Holmgren *et al.*, 2011; Stadnytskyi *et al.*, 2020; Davies *et al.*, 2021; Groth *et al.*, 2021) and numerical studies (Nicas, Nazaroff, and Hubbard, 2005; Wei and Li, 2015; Marr *et al.*, 2019; Chaudhuri, Basu, and Saha, 2020) on respiratory particles, estimates or measurements of g_{d} ranged from ~2 to ~6. Recent experimental measurements on authentic human samples evidence $g_{\mathrm{d}} \sim$ 4.2–5.0 for particles composed mainly of saliva (Lieber *et al.*, 2021; Stiti *et al.*, 2022; Bagheri *et al.*, 2023) and $g_{\mathrm{d}} \sim 4.5$ for particles composed mainly of ELF (Bagheri *et al.*, 2023).

The hygroscopic growth and shrinkage of the respiratory particles can be calculated using Köhler theory, which describes thermodynamic water equilibrium states between the gas and aqueous phases (Köhler, 1936). Specifically, it describes the interplay of the enhancement in water saturation vapor pressure (p_0) over a curved relative to a flat surface and the reduction in p_0 over a solute surface relative to pure water. The Köhler theory has been broadly applied in atmospheric research, as it allows one to describe and model the water uptake and loss by ambient aerosol particles under variable RH conditions (Seinfeld and Pandis, 2016). It has been particularly important to describe the nucleation of cloud droplets by ambient aerosol particles (Andreae and Rosenfeld, 2008). The corresponding Köhler equation

$$s = a_{\mathrm{w}}\mathrm{Ke},$$
$$\text{with } \mathrm{Ke} = \exp\left(\frac{4\sigma_{\mathrm{sol}}M_{\mathrm{w}}}{RT\rho_{\mathrm{w}}D_{\mathrm{wet}}}\right), \tag{15}$$

expresses the necessary conditions for an aqueous solution droplet to be in equilibrium state with the water vapor of the surrounding gas. Specifically, it relates the water vapor saturation ratio s to the *Raoult term*, which is the water activity in the aqueous solution (a_{w}) and describes the size and composition dependencies of the droplet's solute effect, as well as the *Kelvin term* (Ke), which describes the increase in equilibrium water vapor pressure due to the droplet's surface curvature (Köhler, 1936; Seinfeld and Pandis, 2016). In Ke, σ_{sol} is the solution droplet's surface tension, M_{w} is the molar weight of water, ρ_{w} is the water density, R is the universal gas constant, T is the absolute temperature, and $D_{\mathrm{wet}}(\mathrm{RH})$ is the droplet diameter at a given s or RH, with $s = \mathrm{RH}/100\%$ (Seinfeld and Pandis, 2016). The effect of droplet curvature becomes important for $D_{\mathrm{wet}} < 0.1$ μm [Eq. (16)].

Different approximations and parametrizations exist to describe a_{w} and σ_{sol} as a function of the droplet's chemical composition, as outlined systematically by Rose *et al.* (2008). Typically, σ_{sol} is approximated by the surface tension of pure water. A commonly used parametrization of a_{w} is based on the hygroscopicity parameter κ, which was introduced by Petters and Kreidenweis (2007) according to

$$a_{\mathrm{w}} = \left(1 + \kappa\frac{V_{\mathrm{s}}}{V_{\mathrm{w}}}\right)^{-1}, \tag{16}$$

with V as the volumes of the dry solute (s) and pure water (w). The parameter κ reflects the chemical composition of the solutes in the droplets. It is widely used in atmospheric aerosol research (Mikhailov *et al.*, 2013; Paramonov *et al.*, 2013; Pöhlker *et al.*, 2018) and for ambient aerosol samples typically ranges from ~0.1 for organic solutes to ~0.9 for salts (Andreae and Rosenfeld, 2008). According to Petters and Kreidenweis (2007) and Rose *et al.* (2008), κ can be related to fundamental properties of the water and solute as well as the solute's dissociation behavior through

$$\kappa = i_{\mathrm{s}}\frac{n_{\mathrm{s}}V_{\mathrm{w}}}{n_{\mathrm{w}}V_{\mathrm{s}}} = i_{\mathrm{s}}\frac{\rho_{\mathrm{s}}M_{\mathrm{w}}}{\rho_{\mathrm{w}}M_{\mathrm{s}}}, \quad \text{where } i_{\mathrm{s}} \approx \nu_s\Phi_s, \tag{17}$$

with n the numbers of moles, ρ the densities, and M molar masses of the dry solutes (s) and pure water (w) as well as the van 't Hoff factor of the solute i_{s}, with ν_s the stoichiometric dissociation number and Φ_s the molar osmotic coefficient in aqueous solution. To calculate κ based on g_{d}, transform Eq. (16) into

$$\kappa = (g_V - 1)\frac{1 - a_{\mathrm{w}}}{a_{\mathrm{w}}}. \tag{18}$$

Figure 5(a) shows the modeled hygroscopic growth and shrinkage of pure 100 nm NaCl and KCl particles, which are both main constituents of saliva (Table III). Both salts show a pronounced hysteresis in g_{d} with sharp phase transitions at their deliquescence relative humidity (DRH) and efflorescence relative humidity (ERH). For increasing RH starting from dry particles (i.e., < ERH), a sudden deliquescence phase transition occurs at DRH ≈ 75% for NaCl and at DRH ≈ 85% for KCl. In the course of the drying from RH > DRH, the efflorescence phase transitions occur at ERH ≈ 40% for NaCl and at ERH ≈ 50% for KCl (Li *et al.*, 2014). Further shown in Fig. 5(a) is the hygroscopic growth curve of BSA as a proxy for the complex protein mixture in ELF and saliva. The protein (as well as organic compounds in general) shows a significantly lower g_{d} than the salts and is further characterized by the absence of a hysteresis (Mikhailov *et al.*, 2009; Estillore *et al.*, 2017). The experimental g_{d} data points for BSA were originated by Mikhailov

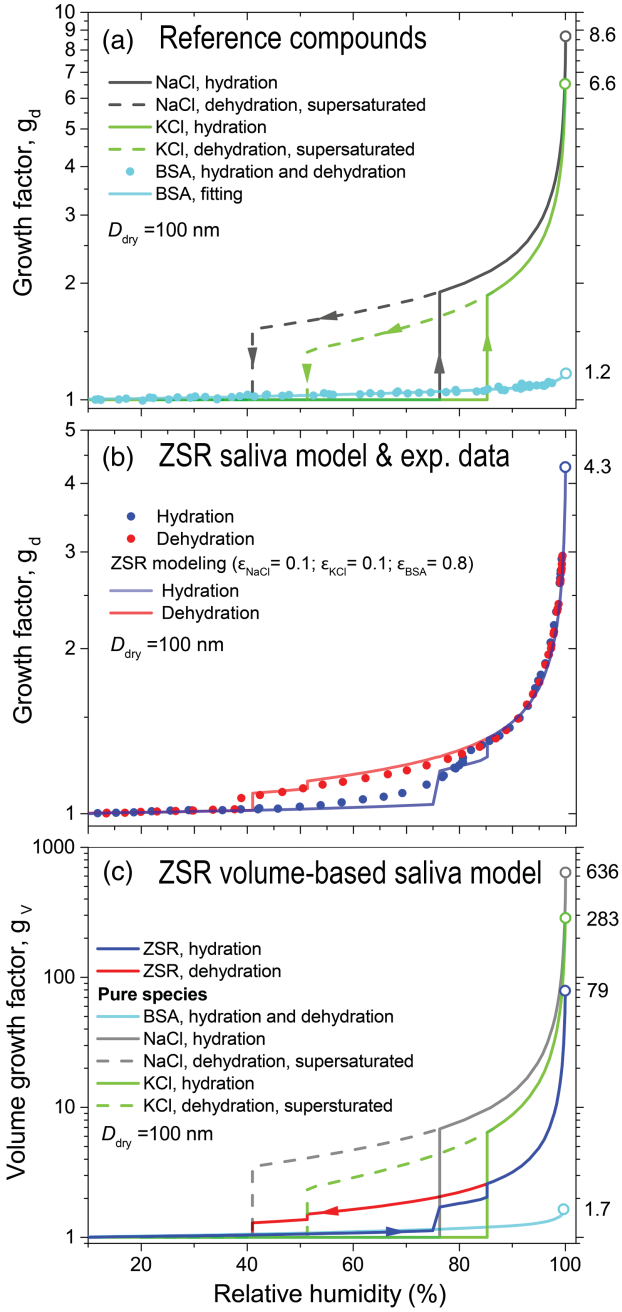

FIG. 5. Hygroscopic growth curves as a function of RH (up to 99.5%) (a) for the reference compounds NaCl, KCl, and protein BSA, as well as (b),(c) for authentic saliva, showing a hysteresis shape in the growth factor g_d with deliquescence and efflorescence phase transitions. (c) The volume hygroscopic growth factor g_V corresponding to g_d in (b). The modeled data (solid and dashed lines) for pure compounds and saliva proxy system (with volume fractions $\epsilon_{NaCl} = 0.1$, $\epsilon_{KCl} = 0.1$, and $\epsilon_{BSA} = 0.8$) were obtained from the aerosol inorganic model (Clegg, Brimblecombe, and Wexler, 1998) and the aerosol inorganic-organic mixtures functional groups activity coefficients model (Zuend *et al.*, 2008; Jing *et al.*, 2017; Mikhailov and Vlasenko, 2020). The experimental data (the circular markers) in (b) were obtained from a high-humidity tandem differential mobility analyzer (HHTDMA) analysis according to Mikhailov and Vlasenko (2020) for stimulated saliva from three healthy, nonsmoking individuals.

et al. (2004) and were fitted using a polynomial three-parameter function according to Kreidenweis *et al.* (2005) as follows:

$$g_d = \left[1 + (k_1 + k_2 s + k_3 s^2)\frac{s}{1-s}\right]^{1/3}, \tag{19}$$

where $k_1 = 0.111$, $k_2 = 0.0239$, and $k_3 = -0.131$, which yields a good fit with $R^2 = 0.95$.

Mikhailov *et al.* (2009) generally defined deliquescence as a transformation of a solid or semisolid substance into a liquid aqueous solution, with gas-phase water being absorbed (also called liquefaction or liquescence upon humidification or hydration). Efflorescence is a transformation of a substance from a liquid aqueous solution into a (semi)solid phase upon water evaporation (also called solidification upon drying or dehydration). Below DRH, the dissolved salts in the particles are supersaturated until the efflorescence phase transition occurs, which is a kinetically limited, homogeneous nucleation process and depends on particle size as well as impurities (Gao, Chen, and Yu, 2007; Laskina *et al.*, 2015). Accordingly, for NaCl (as a main constituent in saliva) a range of ERH values from 37% to 50% has been reported; see Martin (2000), Mikhailov *et al.* (2004), Laskina *et al.* (2015), and references therein. Figures 5(a) and 5(c) show the NaCl ERH at ~40%, which is at the lower end of the aforementioned RH range. DRH values $> 50\%$ are commonly attributed to heterogeneous nucleation due to the presence of impurities (Tang and Munkelwitz, 1994; Lightstone *et al.*, 2000; Mikhailov *et al.*, 2004).

Figure 6 relates to Fig. 5(a) and shows the modeled behavior of g_d beyond water saturation into the supersaturated regime. Under certain conditions, such as breathing in cold and humid air, the respiratory particles can experience an episodic occurrence of supersaturated conditions (Ng *et al.*, 2021). Figure 6 shows that, as long as the supersaturated conditions prevail,

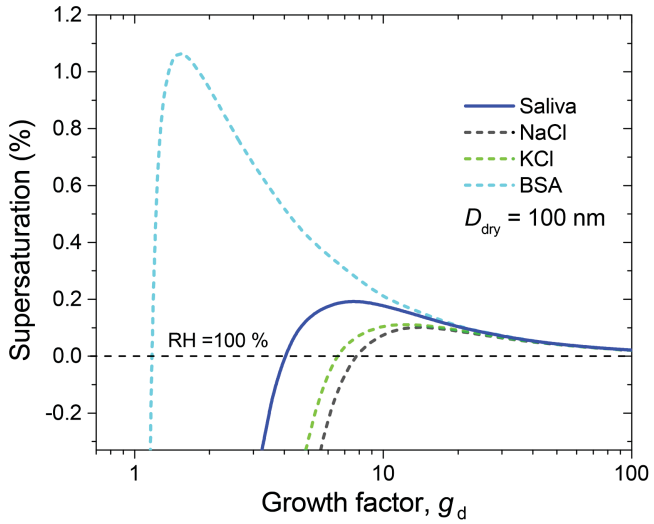

FIG. 6. Hygroscopic growth behavior, represented by growth factor g_d, for the reference compounds NaCl, KCl, and the protein bovine serum albumin (BSA) under supersaturated water vapor conditions.

the exhaled particles might grow substantially before the onset of droplet drying in the course of dilution and dissipation of the exhaled puffs.

As a prediction of the expected hygroscopic behavior of saliva, the three-compound system with the main constituents NaCl, KCl, and BSA was modeled and is shown in Fig. 5(b). The overall g_d of multicompound systems can usually be approximated accurately as the additive influence of the $g_{d,i}$ from the individual compounds i as well as their corresponding volume fractions ϵ_i in the mixture

$$g_d = \left(\sum\nolimits_i \epsilon_i {g_{d,i}}^3\right)^{1/3}, \qquad \epsilon_i = \frac{V_{s,i}}{V_s}, \tag{20}$$

with $V_{s,i}$ the volume of the individual components and V_s the total particle volume. This approach is based on the Zdanovskii-Stokes-Robinson (ZSR) model, which assumes independent water uptake of individual components in mixtures (Stokes and Robinson, 1966).

The resulting g_d of the NaCl-KCl-BSA system in Fig. 5(b) is characterized by a hysteresis with two subsequent deliquescence phase transitions, reflecting the influence of both salts. These model predictions were compared to the results of a "proof-of-concept" hygroscopicity measurement of authentic saliva, and the corresponding data points were added[4] to Fig. 5(b). The model and experimental results agree well despite the fact that the NaCl-KCl-BSA system largely simplifies the chemical complexity of real saliva. The experimental results further underline that a hysteresis in the g_d and g_V curves can generally be expected in the hygroscopic behavior of saliva, and presumably also of ELF, as the two fluids are characterized by similar salt concentrations (Table III). Hygroscopic growth curves for a simulated ELF system with DRH ~ 70% and ERH ~ 50% were recently reported by Davies *et al.* (2021) and Oswin *et al.* (2022), which are largely consistent with Fig. 5(b). Groth *et al.* (2021) reported DRH ~ 65% and ERH ~ 35% for human cough aerosol, which was characterized by a comparatively high organic volume of almost 0.9. Note in this context that the ERH of the saliva at ~38% is lower than the efflorescence RH of the constituents NaCl and KCl at ~41% and ~52% [Fig. 5(c)]. This can be explained by a suppression of the efflorescence phase transition by organic compounds and a corresponding shift of the ERH of the salts to lower values; see Mikhailov *et al.* (2004) and references therein.

The occurrence of a hysteresis in g_d has been discussed as a presumably important microphysical process in respiratory particles that can affect the viability of embedded pathogens (Vejerano and Marr, 2018; Niazi, Groth, Spann, and Johnson, 2021). A hysteresis entails a "bistability" in the humidity dependence within the intermediate humidity range (ERH < RH < DRH), which corresponds to typical indoor RH levels (i.e, ~40% to ~80%) (Niazi, Groth, Cravigan *et al.*, 2021). If the particles are dried from RH > DRH, they shrink upon continuous evaporative water loss and retain a certain amount of water in a metastable salt supersaturation state until the ERH is reached. If the particles are humidified from RH < ERH, they remain as dried residues until the DRH is reached. This means that for ERH < RH < DRH the pathogen-laden particles can either be dried residues or contain a certain amount of water, depending on the "history" of the RH change. It has been proposed that this effect might shed light on the mechanistic relationship of the RH-dependent survival of pathogens (Lin and Marr, 2020; Niazi, Groth, Cravigan *et al.*, 2021; Niazi, Groth, Spann, and Johnson, 2021). Several studies have indicated that bacterial and viral survival rates tend to peak in the low and/or high RH range, with a minimum in the intermediate RH range (Harper, 1961; Arundel *et al.*, 1986; Noti *et al.*, 2013). Such a V-shaped relationship has not been found in all related studies, however. Oswin *et al.* (2022) recently reported a continuous loss of virus stability and infectivity with decreasing RH. Kormuth *et al.* (2018) reported a sustained infectivity across a wide RH range. Further, the specific RH sensitivity appears to be characteristic for a given pathogen (Webb, Bather, and Hodges, 1963; Songer, 1967). Accordingly, the hysteresis and phase transitions of the pathogen-laden respiratory particles in the intermediate RH range might play a decisive role for pathogen transmission.

A further result of the saliva measurement is the RH dependence of κ in the high-humidity regime calculated with Eq. (18), as shown in Fig. 7. A declining trend in κ was observed for < 92% RH, followed by a sudden increase for > 92% RH. Liu *et al.* (2018) and Mikhailov *et al.* (2021) reported similar results for atmospherically relevant purely organic as well as mixed organic-inorganic aerosol particles. Both studies explained the increasing κ for high RH with occurrence of liquid-liquid phase separation (LLPS) in the particles, which was found to be a common and important microphysical process in atmospheric aerosols (Bertram *et al.*, 2011; Song *et al.*, 2012, 2017; Renbaum-Wolff *et al.*, 2016). This suggests that LLPS might also be a characteristic phenomenon in saliva and ELF under high RH conditions, such as near the mouth or within the respiratory tract, again with potentially important implications for pathogen viability (Vejerano and Marr, 2018; Niazi, Groth, Spann, and Johnson, 2021).

D. Formation mechanisms and sites of respiratory particles

Knowledge of the formation mechanisms of human-expired particles and the corresponding sites in the respiratory tract is essential for a mechanistic understanding of airborne

[4]The experimental proof-of-concept data in Fig. 5(b) were obtained from the high-humidity tandem differential mobility analyzer (HHTDMA) analysis in the RH range of 2% to 99.5% according to Mikhailov and Vlasenko (2020) for stimulated saliva from three healthy, nonsmoking individuals. The collected saliva was diluted (1 ml aliquot from each sample mixed with 75 ml of pure water), filtered through a 5 μm syringe filter (25 mm GD/X, sterile, 6901-2504, GE Healthcare Life Science, Whatman), and nebulized for HHTDMA analysis. The HHTDMA procedure and data analysis was outlined by Mikhailov and Vlasenko (2020) and Mikhailov *et al.* (2021). Three operation modes are available for the HHTDMA instrument: a restructuring mode, a hydration mode, and a dehydration mode. The restructuring mode was used to specify the optimal RH range, in which initially irregular particles transform into compact spherical particles. In hygroscopic growth experiments, the restructuring mode was coupled *in situ* with a conventional hydration or dehydration mode.

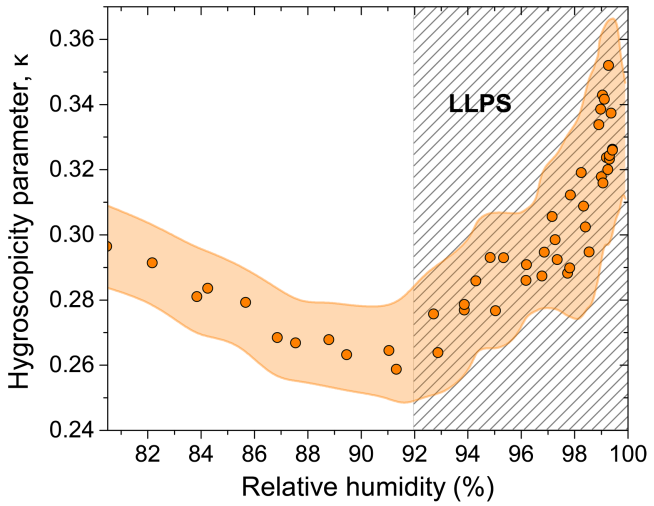

FIG. 7. Hygroscopicity parameter κ in the high RH regime obtained for dried and size-selected (~100 nm) saliva particles based on HHTDMA measurements; see Fig. 5(b). Orange shading indicates uncertainty in κ through error propagation, as outlined by Mikhailov and Vlasenko (2020). The gray background shading > 92% RH with increasing κ values suggests that the particles underwent liquid-liquid phase separation (LLPS).

pathogen transmission; see Johnson and Morawska (2009), Gralton *et al.* (2011), Johnson *et al.* (2011), Patterson and Wood (2019), Dhand and Li (2020), and references therein. Generally the formation is driven by a complex combination of shear and film rupture instabilities, ejecting parts of the mucosalivary films that cover the air-facing surfaces of the respiratory tract (Grotberg, 2001; Seminara *et al.*, 2020; Bourouiba, 2021). These processes are complex, as they depend on a variety of factors, such as respiratory activities (for instance, breathing, speaking, and coughing), geometries and movements of the air-fluid interfaces in the respiratory tract, and the composition and viscoelastic properties of the mucosalivary fluids (Anwarul Hasan, Lange, and King, 2010; Dhand and Li, 2020). The formation site largely defines the composition of exhaled particles, comprising a variable mixture of ELF from the LRT and saliva from the URT; see Sec. II.C. Moreover, pathogens preferentially colonize certain regions of the airways (Shinya *et al.*, 2006; van Riel *et al.*, 2007). Thus, expiration particles may carry particularly high pathogen loads if the site of infection is the same or close to the site of particle formation (Gralton *et al.*, 2011; Patterson and Wood, 2019). The four particle formation mechanisms and associated sites outlined next and summarized in Fig. 8 are widely discussed and considered the most relevant.

1. Bronchiole fluid film burst mechanism

The bronchiole fluid film burst (BFFB) mechanism (or bronchiolar particle generation) is illustrated in Fig. 8(e). It produces comparatively small particles (< 1 μm) from collapsing liquid films deep in the lungs (Johnson and Morawska, 2009; Schwarz, Holz, and Hohlfeld, 2020). During exhalation, the airways partly close, which refers to a compression and an associated blockage of air passage when the airway walls come into contact (Holmgren *et al.*, 2010). Figure 9 conceptually shows the breathing patterns that involve the BFFB process. Closure begins in the lower lungs and progresses toward the upper lung regions with decreasing lung volume (Dollfuss, Milic-Emili, and Bates, 1967; Holmgren *et al.*, 2013). During breathing (such as in normal tidal breathing), the terminal bronchioles are considered the primary site of airway closure. During the subsequent inhalation, the bronchioles reopen and films of the ELF span across the passages, forming a blockage of liquid menisci (Holmgren *et al.*, 2013). When these films rupture, small particles similar to soap film droplets form (Lhuissier and Villermaux, 2009; Prather *et al.*, 2013). These particles are first drawn into the alveoli and are subsequently exhaled, which explains why the concentrations of emitted particles increase toward the end of an individual expiration (Schwarz *et al.*, 2010; Holmgren *et al.*, 2013). Exhaled particle concentrations (C_N) decrease upon breath holding at high lung volume due to diffusion and sedimentation losses in the alveoli, whereas concentrations increase upon breath holding at low lung volume due to a closure of more and more bronchioles with breath holding time (Johnson and Morawska, 2009; Fabian *et al.*, 2011; Holmgren *et al.*, 2013; Schwarz *et al.*, 2015; Bake *et al.*, 2019; Bagheri *et al.*, 2023).

The BFFB particle formation can be modulated by different breathing patterns, with the C_N of exhaled particles scaling proportionally to the fraction of fully contracted bronchioles (Almstrand *et al.*, 2010; Haslbeck *et al.*, 2010; Holmgren *et al.*, 2010, 2013; Fabian *et al.*, 2011; Johnson *et al.*, 2011). Exhalation below functional residual capacity is especially related to airway closure and enhanced particle emission (Schwarz *et al.*, 2010; Tortora and Derrickson, 2017). Schwarz *et al.* (2010) showed that C_N is related to the ventilation ratio V_B/V_{VC} through

$$C_N = C_T \exp\left(b\frac{V_B}{V_{VC}}\right), \tag{21}$$

with V_B the breathed air volume, V_{VC} the vital capacity (Fig. 9), C_T the particle number concentration during low-volume tidal breathing, and b an empirical factor representing the shape of exponential function and typically ranging from 4 to 12 (Schwarz *et al.*, 2010). The ventilation ratio for normal tidal breathing corresponds to ~0.2 and approximates unity for airway closure breathing patterns. Further, Schwarz *et al.* (2010) found a large intersubject variability, in contrast to a high reproducibility, in C_N for the same individual and suggested that the properties of the BFFB particle emissions can serve as a fingerprint for the actual individual lung status. The BFFB particle production is active upon breathing, and therefore also involved in all other respiratory activities (such as speaking and coughing) (Johnson *et al.*, 2011; Bagheri *et al.*, 2023). Thus, BFFB particle production is considered potentially important for airborne pathogen transmission from symptomatic as well as presymptomatic, asymptomatic, and paucisymptomatic infected individuals (Dhand and Li, 2020; Scheuch, 2020).

2. High-speed and turbulent airflow and airway compression and vibration

Gas-fluid interactions, and especially turbulence-induced instabilities at the air-mucus interface (two fluids streaming at

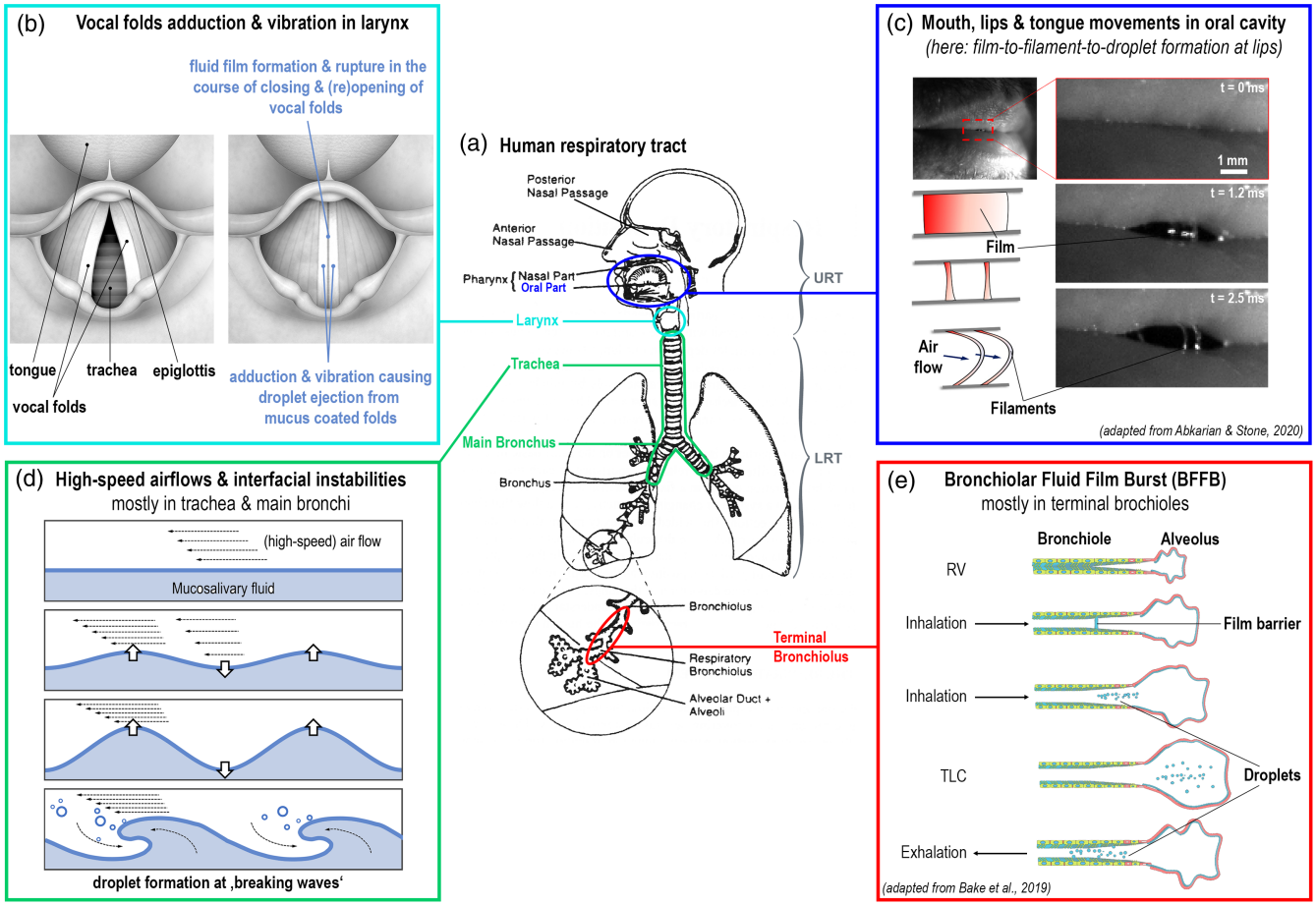

FIG. 8. Conceptual scheme summarizing particle formation mechanisms and sites in (a) the human respiratory tract. The scheme emphasizes the subdivision into the upper respiratory tract (URT) or extrathoracic airways, reaching from larynx to mouth and nose, vs the lower respiratory tract (LRT) or tracheobronchial airways, including trachea, bronchi, bronchioles, and alveoli. Note that the four particle formation categories (b)–(e) are distinguished in the literature and also here primarily by production sites, whereas the production mechanisms are governed by the same few fluid mechanical principles. Concept adapted from Niazi, Groth, Spann, and Johnson, 2021. (a) Adapted from Hinds, 1999. (c) Adapted from Abkarian and Stone, 2020. (e) Adapted from Bake *et al.*, 2019.

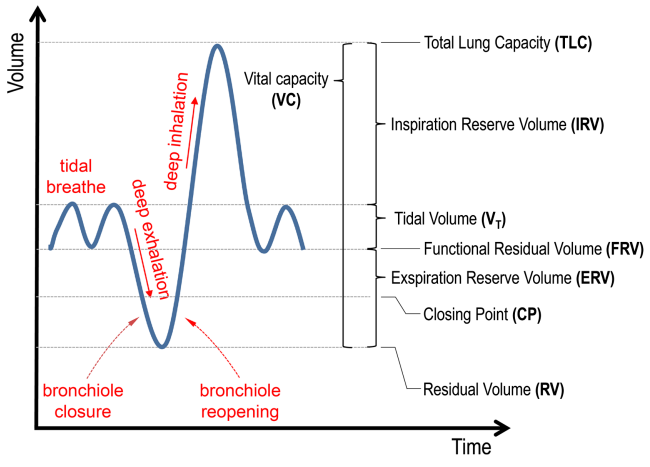

FIG. 9. Conceptual rendering of breathing patterns, including "normal" tidal breathing (corresponding to tidal volume) as well as deep inhalations and exhalations. Similar representations for a variety of breathing patterns can be found in previous studies (Almstrand *et al.*, 2010; Holmgren *et al.*, 2013; Patterson and Wood, 2019).

largely different speeds relative to each other), have been widely discussed as particle generation mechanisms, especially for short and vigorous expirations such as coughing and sneezing (Moriarty and Grotberg, 1999; Holmgren *et al.*, 2010; Patterson and Wood, 2019; Dhand and Li, 2020; Fontes *et al.*, 2020; Wilson *et al.*, 2020). Central airways such as the trachea and main bronchi, with their high-speed and often turbulent airflow, are considered the region where this process is assumed to be most pronounced, whereas airflow in the small airways is mostly laminar due to the strong increase in cross-sectional area (Hinds, 1999; Johnson and Morawska, 2009; Holmgren *et al.*, 2010; Patterson and Wood, 2019; Dhand and Li, 2020). In such high-speed airflow, the associated interfacial shearing causes Kelvin-Helmholtz instabilities as interfacial waves of mucus with increasing amplitude [Fig. 8(d)]. Eventually small droplets are torn off the crest of these waves or filaments of mucus are drawn thin and fragmented into droplets (Plateau-Rayleigh instability) (Dhand and Li, 2020; Seminara *et al.*, 2020). The critical air speed, which created instabilities at the ELF-air interface is defined by the ELF layer thickness [typically 5–10 μm (Seminara *et al.*, 2020)], along with its viscoelastic properties

and surface tension (Moriarty and Grotberg, 1999; Anwarul Hasan, Lange, and King, 2010; Dhand and Li, 2020). Furthermore, dynamic compression and vibration of the airways "squeezes and loosens mucus and promotes expulsion of foreign material from the airways" (Dhand and Li, 2020). For breath-related emissions, turbulence-induced aerosolization has been excluded as a relevant mechanism since variations in flow rates had essentially no influence on droplet emissions (Johnson and Morawska, 2009; Schwarz *et al.*, 2010).

3. Larynx with vocal folds adduction and vibration

Vocal fold adduction and vibration within the larynx, or laryngeal particle generation, is regarded as relevant mechanism during coughing and sneezing as well as during vocalizations such as speaking and singing [Fig. 8(b)] (Asadi *et al.*, 2019). It has been suggested that the narrowing of the mucus-bathed folds forms a flow restriction in which a high-speed airstream caused sufficient shear stress at the ELF-air interface to tear off droplets (Dhand and Li, 2020). Additionally, vigorous vibration and energetic movement of the ELF-coated folds during vocalization may create instabilities in the ELF surface layer and result in particle formation (Moriarty and Grotberg, 1999; Morawska *et al.*, 2009). It has further been considered that, as with the BFFB mechanism, ELF films may form and burst or ELF filaments may fragment in the open-close cycling of the glottic structure (i.e., the opening between the vocal folds) (Johnson *et al.*, 2011; Asadi *et al.*, 2019; Patterson and Wood, 2019; Wilson *et al.*, 2020). Some have suggested that the vocalization frequency (vocal pitch) modulates the particles' emission rate and diameters (Morawska *et al.*, 2009; Asadi *et al.*, 2019; Bagheri *et al.*, 2023).

4. Oral cavity with mouth, lip, and tongue movements

The upper respiratory tract, and particularly the oral cavity between the lips and epiglottis and the nasal passage, is regarded as the main site for large-droplet formation (Abkarian and Stone, 2020; Abkarian *et al.*, 2020; Bagheri *et al.*, 2023). Here droplets through fragmentation of liquid sheets and filamentous structures that are formed from the permanently present saliva in the course of mouth, lip, and tongue movements [Fig. 8(c)] (Johnson *et al.*, 2011; Seminara *et al.*, 2020; Bagheri *et al.*, 2023). In addition, pulsed and high velocity airflow, such as coughing and sneezing, causes significant shear forces in the throat, nasal, and buccal passages, creating a droplet spray through Kelvin-Helmholtz instability (Fontes *et al.*, 2020). The velocity and pressure fields involved strongly depend on the anatomy of the airflow passages as well as the chemical and fluid properties of the saliva (Fontes *et al.*, 2020).

5. Clinical aerosol-generating procedures

So-called aerosol-generating procedures (AGPs), for instance, intubation or high flow nasal oxygen treatments, are clinical procedures that are labeled as such because they can emit aerosols from the patient (Klompas, Baker, and Rhee, 2021). Aerosols can be generated from the nose, mouth, throat, or lungs from a patient undergoing various kinds of invasive procedures. From a clinical perspective, these AGPs have often been considered one of the only sources of infectious aerosols from patients with most respiratory diseases, including COVID-19. The distinction is vital because protective guidelines are often different for situations in which healthcare workers expect to deal with AGPs versus every other situation. When aerosols are present that could contain pathogens, protective equipment (such as masks, respirators, and eye coverings) needs to be significantly improved to reduce the inhalation of small airborne particles (i.e., FFP2 or N95 respirators). Thus, surgical-style procedure masks and face shields are not sufficient protection when aerosols are present, and healthcare workers can thus be left at risk. A survey of AGPs and the physical properties of aerosols emitted by these procedures is not discussed here, in large part because AGPs have been shown to generally produce fewer aerosols than standard respiratory activities like breathing, speaking, and coughing (Brown *et al.*, 2021; Wilson *et al.*, 2021; Hamilton *et al.*, 2022).

III. MULTIMODAL SIZE DISTRIBUTIONS OF HUMAN RESPIRATORY PARTICLES AND ITS PARAMETRIZATION

A. Literature data synthesis

Studies with size distribution data on human respiratory particles along with information on sampling conditions and parameters are collected and summarized in Table IV. The PSDs from the individual studies have been obtained from data tables, digitized from figures, or obtained from direct correspondence with the authors.

Different instruments and measurement strategies for respiratory aerosol characterization have been applied with specific strengths and limitations and are critically evaluated here. Moreover, the individual studies typically cover only part of the entire aerosol size range. The characterization of the comparatively low concentrations of respiratory aerosols requires online or offline techniques that provide full size distributions, ideally also at high time resolution (up to 1 Hz). The most commonly applied online instruments are the scanning mobility particle sizer (SMPS), manufactured by TSI Inc., St. Paul, Minnesota, with a nominal size range typically from 0.01 to 0.4 μm, the aerodynamic particle sizer (APS), TSI Inc., with a nominal size range from 0.5 to 20 μm, and the optical particle sizer (OPS) or optical particle counter (OPC), from different manufacturers, with a nominal size typically ranging from 0.3 to 10 μm. The smallest dry particle size reported in the literature is 0.01 μm, which is due mainly to instrument limitations. Considering the known intricate processes occurring inside the respiratory tract, there is no reason for such a limit at 0.01 μm, and we cannot exclude that particle size distribution persists at smaller sizes. For larger particle fractions (i.e., > 10 μm), passive sampling through particle sedimentation or impaction of expelled droplets (often called droplet deposition analysis) or active sampling through droplet impaction on solid surfaces (for instance, glass slides or culture plates)

TABLE IV. Summary of studies in chronological order reporting aerosol number size distributions (NSDs) from human respiratory activities. A summary is given of analyzed respiratory activities, the number of volunteers in study (N), sizing instruments or techniques, covered size range (as available in figures or tables for further use), and relative humidity (RH) and temperature (θ) in the moment of droplet or particle measurement. Respiratory activities are abbreviated as follows: b = breath, sp = speak, si = sing, sh = shout, c = cough, and sn = sneeze. Note that RH and θ are not clearly defined in all studies. For the definition of the flag in the last column, see Sec. III.A.

Reference(s)	N	Respiratory activity	Instrument (manufacturer, model)	Nominal size range (μm)	RH (%)	θ (°C)	Flag
Duguid (1946)	⋯	sp, c, sn	Impaction and microscopy	1–2000	⋯	⋯	A
Loudon and Roberts (1967a, 1967b)	3	sp, c	Filter sampling or sedimentation and microscopy	2–2000	⋯	⋯	A
Papineni and Rosenthal (1997)	5	b, sp, c	OPC (Climet, CI-7300) plus sedimentation and microscopy	0.3–2.5	45	25	C
Yang *et al.* (2007)	54	c	SMPS (TSI, 3934) plus OPC (TSI, 3310A)	0.6–30	∼95vs ∼35	⋯	C
Fabian *et al.* (2008)	13	b	OPC (Airnet 310)	0.3–5.0	⋯	⋯	B
Morawska *et al.* (2008, 2009)	15	c, sp, c	UV-APS (TSI, 3312A)	0.5–20	83–93	∼27	A
Chao *et al.* (2009)	11	sp, c	Particle image velocimetry and interferometric Mie imaging	2–2000	∼100[a]	∼37	A
Almstrand *et al.* (2009)	1	b	OPC (Grimm, 1.108)	0.3–3.0	∼100[b]	36	A
Johnson and Morawska (2009)	17	b	UV-APS (TSI, 3312A)	0.5–20	90 ± 7	28 ± 1	A
Xie *et al.* (2009)	7	sp, c	Sedimentation and microscopy	10–1000	∼70	∼28	A
Almstrand *et al.* (2010)	10	b	OPC (Grimm, 1.108)	0.3–3.0	∼100[c]	36	A
Haslbeck *et al.* (2010)	16	b	Laser spectrometer (PMS, Lasair II-110)	0.1–5.0	∼95	37	B
Holmgren *et al.* (2010)	16	b	SMPS (TSI, 3936) plus OPC (Grimm, 1.108)	0.01–4.0	∼95	∼35	A
Schwarz *et al.* (2010, 2015)	21	b	Laser spectrometer *(PMS, Lasair II-110)*	0.1–5.0	90–100	37	B
Lai, Bottomley, and McNerney (2011)	8	sh	OPC (Lighthouse, 5016)	0.5–10	∼dried	∼RT	B
Fabian *et al.* (2011)	17	b	OPC (Climet, CI-550)	0.3–10	⋯	⋯	B
Johnson *et al.* (2011)	15	b, sp, c	UV-APS (TSI, 3312A) plus sedimentation and microscopy	0.5–2000	90 ± 7	28 ± 1	A
Holmgren *et al.* (2011)	3	b	OPC (Grimm, 1.108)	0.3–20	75vs 99.5	∼35	A
Lindsley *et al.* (2012)	9	c	SMPS plus OPC (MSP Corp.)	0.35–10	21 ± 1	28 ± 8	A
Zayas *et al.* (2012)	45	c	Laser diffraction droplet sizer (Spraytec, Malvern Inst.)	0.1–900	19 ± 4	23 ± 2	B
Han, Weng, and Huang (2013)	20	sn	Laser diffraction droplet sizer (Spraytec, Malvern Inst.)	0.1–1000	> 32	23 and 24	C
Holmgren *et al.* (2013)	19	b	OPC (Grimm, 1.108)	0.3–3.0	∼100	36	A
Lee *et al.* (2019)	10	c	SMPS (Grimm, 1.108) plus OPS (TSI, 3330)	0.01–10	30–50	21–25	B
Asadi *et al.* (2019)	48	sp	APS (TSI, 3321)	0.5–20	45–80	20–25	A
Alsved, Matamis *et al.* (2020)	12	b, sp, si	APS (TSI, 3321)	0.5–10	≤ 40	∼22	A
Asadi *et al.* (2020)	10	b, sp, c	APS (TSI, 3321)	0.5–20	30–35	22–24	A
Hartmann *et al.* (2020)	18	b, sp, c	Laser particle counter (LPC, Solair 3100)	0.3–3.0	40 ± 2[d]	22 ± 0.5	B
Smith *et al.* (2020)	7	sp, c	Laser diffraction droplet sizer (Spraytec, Malvern Inst.)	1–2000	90–100	⋯	C
Li, Niu, and Zhu (2021)	1	c	APS (TSI, 3321)	0.5–20	54 ± 5[e]	25 ± 1	A
Gregson *et al.* (2021)	25	b, sp, si	APS (TSI, 3321)	0.5–20	∼45	∼20	A
Mürbe *et al.* (2021)	8	b, sp, si	Laser particle counter (Lighthouse Solair 3100 E)	0.3–10	40 ± 2	22 ± 0.5	B
Good *et al.* (2021)	63	si	OPC (Grimm, 11-D)	0.25–33	⋯	⋯	A
Bagheri *et al.* (2023)	132	b, sp, si, sh	SMPS (TSI, 3910) plus OPS (TSI, 3330) plus holography	0.01– > 1000	< 30	23	A
Archer *et al.* (2022)	136	b, sp, si	APS (TSI, 3321)	0.5–20	∼45[f]	∼20	A
Fleischer *et al.* (2022)	30	b, sp, si, sh	Laser particle counter (Lighthouse Solair 3100 E)	0.3–10	40 ± 2	22 ± 0.5	B

[a]Referring to the statement in the study that "evaporation and condensation effects had negligible impact on the measured droplet size."
[b]Estimated RH range. The study states that the analysis was conducted "without altering particle size through evaporation or condensation."
[c]Estimated RH range. See Almstrand *et al.* (2009).
[d]θ and RH not specified by Hartmann *et al.* (2020). Values here are from Mürbe *et al.* (2021), who used the same experimental setup.
[e]Three measurement distances (i.e., 0.3, 0.9, and 1.8 m) between the inlet and volunteer used: here 0.3 and 0.9 m are implemented.
[f]θ and RH are not specified. The values were adapted from Gregson *et al.* (2021) using the same experimental setup.

followed by image analysis has been used (Duguid, 1946; Loudon and Roberts, 1967a, 1967b; Xie *et al.*, 2009; Johnson *et al.*, 2011). Further, several online techniques have been applied, including interferometric Mie imaging (Chao *et al.*, 2009), open-path laser diffraction droplet sizing (Han, Weng, and Huang, 2013; Smith *et al.*, 2020), and holography (Bagheri *et al.*, 2023). Further techniques and details were discussed by Mahjoub Mohammed Merghani *et al.* (2021).

The APS has been a widely used instrument in respiratory aerosol characterization (Johnson and Morawska, 2009; Morawska *et al.*, 2009; Johnson *et al.*, 2011; Asadi *et al.*, 2019; Gregson *et al.*, 2021). Different models of the APS have been used; see Table IV for details. However, several instrumental issues have been reported for different APS models, and caution is thus required when APS-derived PSDs are used (Armendariz and Leith, 2002; Peters and Leith, 2003; Volckens and Peters, 2005; Pfeifer *et al.*, 2016; Bagheri *et al.*, 2023). While the sizing accuracy of the APS is generally acceptable, issues with the counting efficiency and instrument's unit-to-unit variability in certain size ranges have been reported (Peters and Leith, 2003; Pfeifer *et al.*, 2016). Generally Peters and Leith (2003) showed that the counting efficiency can be strongly size dependent and varies between different APS models. Particularly relevant for the characterization of expiration aerosols upon release (which means in a humid state) is a substantially decreased counting efficiency of liquid particles (i.e., declining from 75% at 0.8 μm to 25% for 10 μm) due to impaction losses in the instrument's flow system (Volckens and Peters, 2005). Pfeifer *et al.* (2016) recently showed a strongly increased unit-to-unit variability (up to 60%) for particles smaller (0.9 μm) and larger (3 μm), probably due to different detector sensitivities. In addition, in previous studies on expiration aerosols (Johnson and Morawska, 2009; Morawska *et al.*, 2009) the decline in detection efficiencies in the lower and upper APS size range was emphasized. Bagheri *et al.* (2023) recently provided a direct comparison of the APS versus OPC PSDs in the Supplemental Material of their study that underlined a significant undercounting of the APS above ∼5 μm. In ambient aerosol observations, a similar deviation showing a decline in APS counting efficiency also above ∼5 μm relative to an OPC was reported (Martin *et al.*, 2010; Artaxo *et al.*, 2022). Note that Martin *et al.* (2010) limited the APS size range from 0.8 to 5 μm. In light of these known issues of the instrument, we have chosen a conservative approach here and limited the size range of reported APS data to the relatively narrow band from 0.9 to 5 μm, where the counting efficiency is relatively high and unit-to-unit variability is relatively low. For other instruments and sizing strategies the entire reported size ranges have been used; see Table IV.

For OPC instruments, polystyrene latex spheres (PSLs) are typically used for particle size calibrations. The refractive index of PSLs differs from respiratory particles, however, which will effect the calculated sizing. Holmgren *et al.* (2010) provided a size correction of ∼1.6 based on a diluted isotopic water solution of organic and inorganic solutes, which approximates the composition of the exhaled particles. This correction was adopted for all OPS data if it was not implemented in the original studies.

B. Development of a generalized parametrization scheme

As part of the literature synthesis, we developed a multimodal, log-normal parametrization of exhaled PSDs in relation to previous observations and fitting approaches (Chao *et al.*, 2009; Morawska *et al.*, 2009; Johnson *et al.*, 2011; Han, Weng, and Huang, 2013; Asadi *et al.*, 2019; Bagheri *et al.*, 2023). This parametrization was developed under the assumption that the respiration aerosol emission is governed by the same basic formation and loss mechanisms in the human respiratory tract and that the respiratory aerosol PSD, therefore, has some general and consistent properties. This relates, in particular, to the number, position, and width of the individual modes, which convey physical meaning in the sense that they represent a certain set of intersubjectively active processes in the human respiratory tract; see Sec. II.D. A related similar was previously proposed by Johnson *et al.* (2011). In addition, Morawska *et al.* (2009), Alsved, Matamis *et al.* (2020), Gregson *et al.* (2021), and others reported fitting approaches, although mostly for narrower ranges of the overall PSD. A main guideline in developing a uniform parametrization scheme was to find the smallest number of modes and their generalized properties to describe all PSDs in Table VI in number and volume representation, instead of adjusting the number of modes and their properties for either the NSD or VSD of individual studies. Log-normal fit functions according to Eqs. (8) and (9) have been widely used because they match the experimental PSDs' shape of respiratory aerosols well (Johnson *et al.*, 2011; Asadi *et al.*, 2019; Gregson *et al.*, 2021; Bagheri *et al.*, 2023) as well as ambient aerosols from different sources (Willeke and Whitby, 1975; Heintzenberg, 1994). There is no rigorous theoretical justification for the use of log-normal fit functions, and their application can be regarded as a semi-empirical (though widely established) fit (John, 2011; Seinfeld and Pandis, 2016).

While previous parametrizations follow a one-dimensional strategy by fitting either the NSD or the VSD (Morawska *et al.*, 2009; Johnson *et al.*, 2011; Asadi *et al.*, 2019), we applied here a two-dimensional fitting approach to ensure that the parametrization described the NSD and VSD of a given dataset equally well; see Sec. II.B.2. This was done iteratively by optimizing the coefficient of determination R^2 for the NSD and VSD fits. One consistent parametrization scheme was developed that represents all PSDs of appropriate resolution and quality from the existing literature in Table VI. Since not all PSDs of the studies in Table IV were equally appropriate for the development of a general parametrization, the following flags in Table IV specify to what extent the individual studies were used:

- *A*.—The study was used in the literature and data synthesis. The size resolution of the reported PSDs is sufficiently high to allow a multimodal fitting with comparatively low uncertainty. The reported PSDs were further used to calculate the average parametrizations in Fig. 18 and the averaged fit parameters in Table VI.
- *B*.—The study was used in the literature and data synthesis of this work for comparison only. The size resolution of the reported PSDs is comparatively low and fitting entails high uncertainties. Therefore, the reported

PSDs were not used to calculate the average parametrizations in Fig. 18 and the averaged fit parameters in Table VI.

- *C.*—The corresponding study was not used in the data synthesis of this work. The study was omitted for one or more of the following reasons: (i) data points from the original publication could not be unambiguously digitized (Papineni and Rosenthal, 1997), (ii) important information for the calculation of concentrations and for PSD normalization was missing (Han, Weng, and Huang, 2013; Smith *et al.*, 2020), or (iii) fundamental open questions on the methodology or experimental limitations remained (Yang *et al.*, 2007).

The number of modes was chosen as small as possible, with five modes being the minimum to still cover all major features of the shape of the experimental PSDs. The individual log-normal modes overlap to a significant extent. This requires one to constrain some of the fit parameters either within a certain corridor of values or even to a fixed value in order to obtain physically meaningful multimodal fits. Here we constrained the width of the modes to $\sigma_i = 0.9$, with the position D_i and height A_i of the modes being free parameters. Note that $\sigma_i = 0.9$ was found to be an appropriate width of all modes of the respiration aerosol PSDs, as outlined in Sec. III.C.1.

The fitting of the experimental PSDs from the studies in Table VI followed this workflow:

(1) Respiration PSDs were obtained from tables or digitized from figures of the original publications.[5] The size range of the APS data was limited to 0.9–5 μm for the aforementioned reasons. For OPC data, the size bins were corrected according to the difference in the refractive index of the calibration and respiratory particles.
(2) The data were normalized by the size bin widths to $dC/d\log D$ and $dQ/d\log D$ if they were not already available as such in the original publications.
(3) The PSDs where fitted by a multimodal log-normal function with least squares in number and volume (NSD and VSD) using Eq. (8). The fitting was conducted with IGOR Pro (version 8.04; Wavemetrics, Inc., Portland, Oregon). The fit functions were iteratively optimized to equally describe both the NSD and the VSD of a given dataset. A fit for a given PSD was accepted if both NSD and VSD were described in a physically meaningful way with a maximum R^2. As part of the fitting process, some fit parameters were constrained as described in the corresponding parts of Sec. III.
(4) After fitting, the NSDs and VSDs were normalized to allow a comparison of the shape of all PSDs of a certain category. Normalization to a specific area under the curve was conducted: (a) for small particles ($D < 5$ μm), the overall trimodal PSD was normalized to the area under breath-related bimodal distribution (i.e., modes B1 and B2; for details see Sec. III.C.1), and (b) for large particles ($D > 5$ μm), the overall bimodal PSD was normalized to the area under the second of both modes (i.e., mode O2; for details see Sec. III.C.2).
(5) Average PSDs were calculated using the arithmetic means of the corresponding fit parameters, based on all PSDs flagged with A's in Table IV.

Figure 10 illustrates the workflow and relates it to the figures in Sec. III.

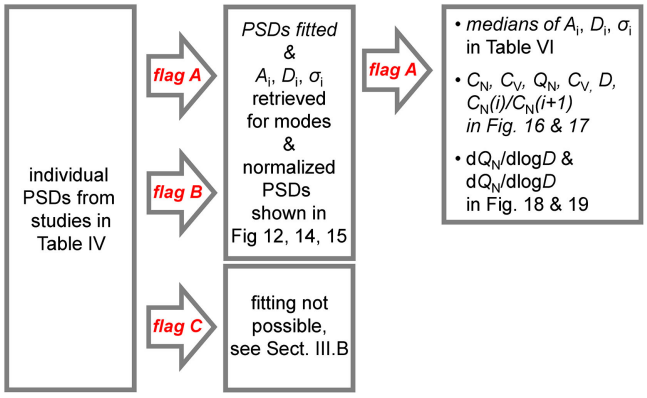

FIG. 10. Flow scheme illustrating how the original PSDs from the studies in Table IV were normalized and combined to obtain the synthesis of Figs. 12, 14, and 15, as well as the generalized parametrization in Table VI.

C. Parametrizations of particle size distributions for specific respiratory activities

1. Breathing

Breathing is the most fundamental, frequent, and continuous respiratory activity. Speaking, laughing, singing, coughing, and sneezing involve breathing as an underlying mode. Hence, the development of a parametrization of respiration PSDs should start with a robust representation of breath-related emissions. Several studies have investigated aerosol formation in relation to different breathing patterns (see Fig. 9), and it is widely supposed that the BFFB mechanism outlined in Sec. II.D is primarily (if not exclusively) responsible for the breath-related particle formation (Johnson and Morawska, 2009; Holmgren *et al.*, 2010; Holmgren and Ljungström, 2012; Bake *et al.*, 2017, 2019; Bagheri *et al.*, 2023). Here we have integrated the published experimental data to parametrize the shape of the breath PSD. The largely variable particle concentrations (C_N and C_V) and emission rates (Q_N and Q_V) of breath-related emissions in relation to other respiratory activities are addressed in Sec. III.D. This analysis shows that after fitting and normalization all published breath PSDs agree well despite differences in methodology and variable RH conditions during the measurements.

The experimental basis for the parametrization comprises 36 breath PSDs from 16 studies; see Table IV. Good data coverage exists for the particle size ranging from 0.3 to 5 μm due to the wide use of the instrument's APS (Johnson and Morawska, 2009; Morawska *et al.*, 2009; Johnson *et al.*, 2011;

[5]For digitization, the Web application WebPlotDigitizer available under https://automeris.io/WebPlotDigitizer/ (last accessed on September 30, 2022) has been used. Only those data points that could be unambiguously picked were collected.

Alsved, Matamis *et al.*, 2020; Gregson *et al.*, 2021) (i.e., 0.9 to 5 μm; see Sec. III.A) as well as different OPC models (Fabian *et al.*, 2008, 2011; Almstrand *et al.*, 2009, 2010; Haslbeck *et al.*, 2010; Holmgren *et al.*, 2010, 2013; Cummins *et al.*, 2020; Cyranoski, 2020; Hartmann *et al.*, 2020; Curtius, Granzin, and Schrod, 2021; Bagheri *et al.*, 2023) (i.e., 0.3 to 3 μm); see Table IV. Studies with data coverage < 0.3 μm are sparse. Holmgren *et al.* (2010) and Bagheri *et al.* (2023) published two of the few studies thus far with highly size-resolved SMPS measurements reaching below 0.3 μm that cover the peak and overall shape of the breath PSD. Therefore, we primarily used these two datasets to parametrize the lower end of the breath PSD based on Eq. (8). Figure 11 shows the PSDs for tidal breathing and breathing with airway closure from Holmgren *et al.* (2010), as well as the PSD for tidal breathing averaged across a large number of subjects from Bagheri *et al.* (2023). In addition, the corresponding multimodal log-normal fits are shown, and they represent the PSDs accurately in number and volume representation.

The breath PSDs in Fig. 11 represent (slightly) different RH conditions, which could entail large differences in the hygroscopic growth factor g_d due to the steep slope of the RH-g_d relationship in the high RH range (Fig. 5). Specifically, the mode position D_i varies as a function of RH. The PSDs from Holmgren *et al.* (2010) were obtained at RH $\approx 95\%$, whereas the PSDs from Bagheri *et al.* (2023) were obtained at RH $< 30\%$ and corrected afterward to RH $= 100\%$ by applying a factor of $g_d = 4.5$ based on experimental data from authentic human ELF. Consistent with the high RH conditions, the modes of the PSDs from Bagheri *et al.* (2023), for breathing in Fig. 11 and vocalization in the subsequent figures, are located at comparatively large D_i (see Fig. 11 and Table V), whereas the PSD shape is consistent with Holmgren *et al.* (2010) and other studies. Accordingly, the PSDs from Bagheri *et al.* (2023) can be regarded as an upper bound for particle size of the individual modes, which provides a valuable reference to assess the influence of RH.

Predominant are two bronchiolar breathing modes, to which we refer as B1 (peaking at $D < 0.2$ μm in NSD) and B2 (peaking at $D > 0.2$ μm in NSD), following the nomenclature of Johnson *et al.* (2011). Across the entire PSD of respiration aerosols, the size range of the B1 mode has the lowest coverage of experimental data to date, (i) with four studies providing breath-related data (Haslbeck *et al.*, 2010; Holmgren *et al.*, 2010; Schwarz *et al.*, 2010; Bagheri *et al.*, 2023), shown in this section, (ii) one study with vocalization-related data (Bagheri *et al.*, 2023), shown in Sec. III.C.2, and (iii) two studies with cough-related data [see Zayas *et al.* (2012) and Lee *et al.* (2019), with the latter having restrictions], shown in Sec. III.C.3. Accordingly, the existence and properties of the B1 mode can be regarded as more uncertain than the B2 mode, which is characterized by a significantly high data coverage. Nevertheless, the four existing studies on

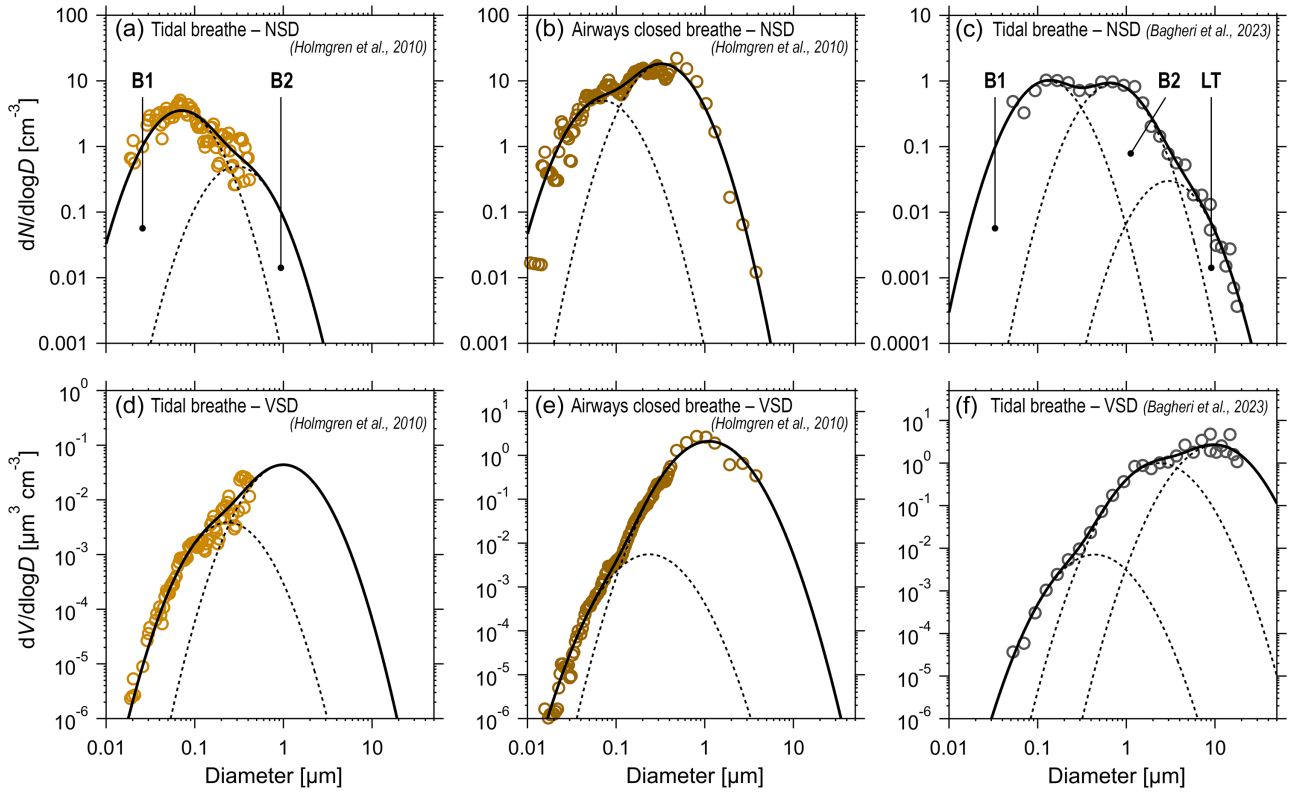

FIG. 11. Number and volume particle size distributions (NSD and VSD) for (a),(d) tidal breathing and (b),(e) breathing with airway closure, as well as (c),(f) tidal breathing. Circular markers represent data points from the original studies. Solid lines represent bimodal log-normal fits of the data with the underlying log-normal modes B1 and B2 from Holmgren *et al.* (2010) as well as B1, B2, and LT from Bagheri *et al.* (2023), which are shown as black dashed lines. In this representation, the individual PSDs were not normalized. The corresponding fit parameters are summarized in Table V. (a),(b),(d),(e) From Holmgren *et al.*, 2010. (c),(f) From Bagheri *et al.*, 2023.

TABLE V. Fit parameters for bimodal log-normal fits of NSDs and VSDs for (i) tidal breathing vs breathing with airway closure from Holmgren *et al.* (2010) as well as tidal breathing from Bagheri *et al.* (2023), as shown in Fig. 11, and (ii) sea spray aerosol based on a study by Prather *et al.* (2013), as shown in Fig. 13. Specified are the mode-specific particle number and volume concentrations (C_N, C_V), height (A_i), position (D_i), and width (σ_i). The coefficient of determination (R_N^2 vs R_V^2) shows the quality of fits for the number and volume representations of the PSDs.

Breathing pattern	Mode	C_N (cm^{-3})	A_i (cm^{-3})	D_i (μm)	σ_i	R_N^2	C_V (μm^3 cm^{-3})	R_V^2
Tidal breathing	B1	2.42	3.5	0.07	0.9	0.77	0.003	0.69
(Holmgren *et al.*, 2010)	B2	0.35	0.5	0.3	0.9		0.03	
Airway closure	B1	3.46	5	0.07	0.9	0.84	0.004	0.89
(Holmgren *et al.*, 2010)	B2	12.47	18	0.33	0.9		1.45	
Tidal breathing	B1	0.69	1	0.13	0.9	0.97	0.005	0.72
(Bagheri *et al.*, 2023)	B2	0.62	0.9	0.70	0.9		0.69	
	LT	0.02	0.03	3.00	0.9		1.82	
SSA: Sintered glass	1	1.08	2	0.05	0.70	0.93	0.0002	0.54
	2	0.05	0.07	0.25	0.90	0.93	0.002	
SSA: Plunging waterfall	1	0.98	0.7	0.11	1.8	0.90	0.99	0.69

breathing [and, in particular, the statistically robust work by Bagheri *et al.* (2023), with more than 130 subjects] consistently support the existence and shape of the B1 mode, as shown in Fig. 11. In the bimodal fits, the position D_i and the height A_i of both log-normal modes were free parameters, whereas the width σ_i of the modes was fixed to 0.9. This σ_i value was iteratively optimized in the literature synthesis conducted here. In fact, an important result of the fitting approach overall is the observation that $\sigma_i = 0.9$ describes fairly well the width of all log-normal modes of respiratory PSDs across multiple studies. For comparison, the width of the characteristic modes in the ambient aerosol is typically smaller, with σ ranging from ∼0.4 to ∼0.6 (Pöhlker *et al.*, 2016). The shape of the PSD from Bagheri *et al.* (2023) agrees well with the underlying B1 and B2 modes, but also requires to involve the larynx and trachea (LT) mode, which becomes prominent for vocalization activities and is introduced in Sec. III.C.2. The data of the studies by Haslbeck *et al.* (2010) and Schwarz *et al.* (2010), both with sizing data down to 0.1 μm, though with much lower size resolution, generally support the bimodal character of the breath PSD with predominant B1 and B2 modes. Note that monomodal log-normal functions were actually also tested to fit the experimental NSDs and VSDs in Fig. 11 during a search for the simplest fit function. It turned out, however, that a monomodal fit does not accurately describe the data across the entire experimental size range, which underlines the inherent multimodal character of breath PSDs.

Figure 11 and Table V show that the resulting D_i values for the B1 and B2 modes are consistent for all three PSDs, and that the difference in shape is determined mainly by variable heights of the modes B1 and B2. Holmgren *et al.* (2010) argued that different breathing patterns (i.e., tidal breathing versus breathing with airway closure) might entail differences in the PSDs' shape. They attributed mode B2 to the BFFB mechanism in the terminal bronchioles, as it increased strongly for airway closure relative to tidal breathing (i.e., A_{B2} increased by a factor of 36). They further speculated that mode B1 may originate from a similar film bursting, for instance, at the alveoli openings in the course of alveolar dynamics during respiration, which to our knowledge has thus far remained an unverified hypothesis (Scarpelli, 1998; Scarpelli and Hills, 2000; Namati *et al.*, 2008). Differences in breath NSD shape can be described by the ratio of the mode heights with $A_{B1}/A_{B2} = 7.0$ for tidal breathing versus $A_{B1}/A_{B2} = 0.3$ for airway closure breathing given by Holmgren *et al.* (2010) versus $A_{B1}/A_{B2} = 1.1$ for tidal breathing given by Bagheri *et al.* (2023).

Figure 12 summarizes all breath PSDs found in the literature after fitting and normalization. It shows a consistent picture, with essentially all data points falling within a relatively narrow "corridor." Only the VSDs from Morawska *et al.* (2009) and Bagheri *et al.* (2023) deviate for particles larger than ∼1 μm, which can be explained with an involvement of the LT mode at least for the VSD of Bagheri *et al.* (2023); see Fig. 11. Nevertheless, the LT mode was not found in most breath PSDs, and its role can therefore not be conclusively clarified with the data available to date. At first glance, the good agreement among all breath PSDs is noteworthy given that multiple studies with different instruments and data from a large number of volunteers in the experiments are combined here. In fact, Fig. 12 suggests that breath aerosols are associated with a characteristic bimodal shape of the PSD without a clear intersubject or intrasubject variability. This is in stark contrast to the breath-related C_N and Q_N, which are widely variable across individuals (Sec. III.D) (Schwarz *et al.*, 2010; Mürbe *et al.*, 2021). At second glance, though, the consistent PSD shape appears less surprising, as the size distribution (after BFFB emission deep in the lung) is "shaped" by the transmissibility of the respiratory tract upon exhalation (Schwarz *et al.*, 2010). This means that on their way to the mouth or nose certain small particle fractions are removed by diffusional losses and certain large particle fractions are removed by sedimentation or impaction (von der Weiden, Drewnick, and Borrmann, 2009). In fact, established lung deposition models, such as the International Commission on Radiological Protection (ICPR) model (Hinds, 1999), show a penetration maximum of the respiratory tract between 0.3 and 0.4 μm, which corresponds with the size distribution maximum in Fig. 12. Accordingly, the characteristic shape of the breath PSD is presumably determined by both the BFFB emission mechanism and particle losses upon exhalation.

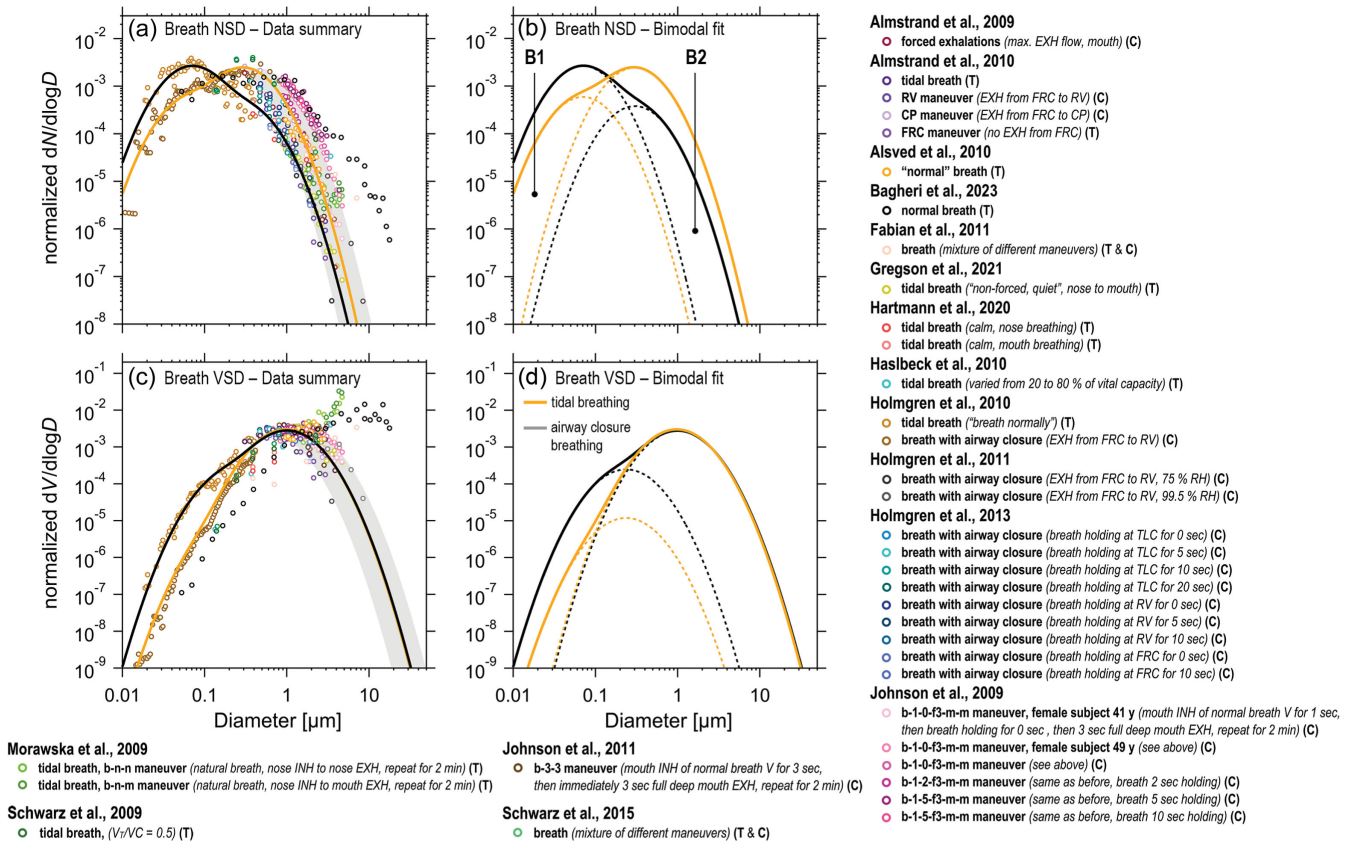

FIG. 12. (a),(c) Breath aerosol number and volume size distributions obtained from multiple studies and (b),(d) bimodal fit functions with underlying log-normal modes for parametrizations of NSDs and VSDs. Tidal breathing (black line) vs airway closure breathing (orange line) maneuvers were discriminated according to Holmgren *et al.* (2010). In the legend, *T* specifies tidal-like breathing patterns and *C* specifies breathing patterns with airway closure. After fitting, all NSDs and VSDs were normalized to the area under the curve to account for the widely variable breath aerosol concentrations. The underlying log-normal modes B1 and B2 are shown as dashed lines. The gray shading in (a) and (c) shows the influence of the aerosol humidification state based on breath aerosol characterization at 75% vs 99.5% RH given by Holmgren *et al.* (2011). The legend summarizes information on specific breathing maneuvers conducted in the individual studies in relation to Fig. 9. For further details, refer to the original articles.

The fit functions in Fig. 12 were calculated as the averages of all fit parameters from the individually fitted NSDs and represent a robust parametrization of breath PSDs. The average fit parameters are summarized in Table VI. Across all individual NSDs, the B2 mode D_{B2} ranges from 0.15 to 0.70 µm (average: $D_{B2} = 0.31$ µm). The variability in D_{B2} can be explained by two effects: First, the measured droplet diameters equilibrate quickly as a function of RH (Sec. II.C). Therefore, the differences in D_{B2} of the individual NSDs reflect to some extent the large differences in RH under the corresponding measurement conditions; see Table IV. Note that temperature and RH are poorly defined or even undefined in some studies, which complicates the comparison among different NSDs. For many studies in Table IV, RH levels ranged between 80% and water saturation, a humidity regime in which a small ΔRH causes a large ΔD (Figs. 4 and 5). One reference point here is the PSDs from Bagheri *et al.* (2023) corrected to RH = 100%, which represent the upper bound of the variability in D in Fig. 12. Another reference point was provided by Holmgren *et al.* (2011), who characterized the RH-related ΔD by measuring comparable breath NSDs (involving airway closure) at 75% versus 99.5% RH. Here the NSD at 75% corresponds to $D_{B2} = 0.18$ µm and the NSD at 99.5% corresponds to $D_{B2} = 0.45$ µm, yielding an increase in D by a factor of 2.5, which is in good agreement with Fig. 5. This RH-related difference in mode B2 from Holmgren *et al.* (2011) is shown in Figs. 12(a) and 12(c) as gray shading and corresponds well with the overall scattering of the data points. Second, the different breathing pattern summarized in Fig. 12 and the associated differences in air residence time in the respiratory tract might also cause certain modulations in the overall PSD shape (Johnson and Morawska, 2009; Schwarz *et al.*, 2010; Holmgren *et al.*, 2013). This effect seems to be smaller than the RH influence, although further studies are needed.

In Sec. II.D, the mechanistic analogy between respiratory aerosol formation through the BFFB process and other natural bubble bursting processes, such as sea spray aerosol (SSA) formation through bubble bursting at the air-ocean interface, has been discussed (Holmgren *et al.*, 2010). For further illustration, Fig. 13 shows SSA size distributions from Prather *et al.* (2013) generated in the laboratory with natural sea water through three different processes. Note that the breath aerosol versus SSA PSDs span across a similar size range and further show some analogies in terms of mode position and shape (i.e., the similar bimodal shape of sintered

TABLE VI. Average fit parameters for breathing (see Fig. 12), speaking and singing (see Fig. 14), and coughing (see Fig. 15) size distributions in a $dN/d\log D$ representation. Specified are the following mode-specific parameters: height (A_i), position (D_i), width (σ_i), integral particle number and volume concentrations (C_N and C_V), and emission rates (Q_N and Q_V). Q_N and Q_V were obtained from C_N and C_V by applying Eq. (6) with q from Table I.

Respiratory activity	Mode	A_i (cm^{-3})	D_i (μm)	σ_i	C_N (cm^{-3})	C_V ($\mu m^3\,cm^{-3}$)	Q_N (h^{-1})	Q_V ($\mu m^3\,h^{-1}$)
Tidal breathing	B1	1.40×10^{1}	0.07	0.90	9.70	1.08×10^{-2}	3.49×10^{6}	3.88×10^{3}
	B2	2.00	0.30	0.90	1.39	0.12	4.99×10^{5}	4.36×10^{4}
Breathing with airway closure	B1	7.00	0.07	0.90	4.85	5.39×10^{-3}	1.75×10^{6}	1.94×10^{3}
	B2	2.75×10^{1}	0.24	0.90	1.91×10^{1}	0.85	6.86×10^{6}	3.07×10^{5}
Speaking	B1	0.18	0.13	0.90	0.12	1.39×10^{-4}	8.73×10^{4}	9.70×10^{1}
	B2	0.20	0.30	0.90	0.14	1.21×10^{-2}	9.70×10^{4}	8.48×10^{3}
	LT	0.30	1.10	0.90	0.21	0.90	1.45×10^{5}	6.27×10^{5}
	O1	0.03	1.00×10^{1}	0.90	2.08×10^{-2}	6.73×10^{1}	1.45×10^{4}	4.71×10^{7}
	O2	0.21	7.05×10^{1}	0.90	0.15	1.63×10^{5}	1.02×10^{5}	1.14×10^{11}
Coughing	B1	9.80×10^{1}	0.07	0.90	6.79×10^{1}	7.54×10^{-2}	1.02×10^{6}	1.13×10^{3}
	B2	1.40×10^{1}	0.3	0.90	9.70	0.85	1.45×10^{5}	1.27×10^{4}
	LT	0.50	1.00	0.90	0.35	1.12	5.20×10^{3}	1.68×10^{4}
	O1	0.40	1.20×10^{1}	1.30	0.40	1.59×10^{4}	6.00×10^{3}	2.39×10^{8}
	O2	8.50×10^{-2}	9.00×10^{1}	0.90	5.89×10^{2}	1.39×10^{5}	8.83×10^{3}	2.09×10^{9}

glass PSD versus tidal breath PSD). This might reflect the mechanistic relationship of both aerosol formation processes (Lhuissier and Villermaux, 2009, 2012). In this context, the similarity underlines the general plausibility of the breath PSD parametrizations in Fig. 12 in the relation to the relatively well characterized SSA size distributions (Quinn *et al.*, 2015; Wex *et al.*, 2016; Gong *et al.*, 2020). There are other examples of particle size distributions under conditions less complicated than those in the respiratory tract, such as fragmentation of a water jet that can lead to a bimodal particle size distribution, i.e., a main droplet mode and a satellite droplet mode (Villermaux, 2020). The satellite droplet mode resulting from the thinning of liquid bridges has also been shown to be affected by the presence of surfactants (Kovalchuk, Nowak, and Simmons, 2016), which is of great significance for the mucosal fluid.

2. Speaking and singing

Speaking and singing involve opening or closing of the glottis as well as tensing and vibrating of the vocal folds in the larynx, producing (together with mouth, lip, and tongue movements) a wide spectrum of sounds (Abkarian *et al.*, 2020). Both speaking and singing are widely variable, with speaking spanning from whispering to shouting. Speaking is a relatively frequent and semicontinuous respiratory activity. In relation to speaking, singing is typically characterized by continuous vocalization, higher sound pressure, higher frequencies, deeper breaths, higher peak airflow, and more articulated consonants (Alsved, Matamis *et al.*, 2020). In airborne pathogen transmission, both speaking and singing have been considered significant driving forces, as they are major sources of respiratory particles (Asadi *et al.*, 2019; 2023; Gregson *et al.*, 2021; Mürbe *et al.*, 2021; Bagheri *et al.*, 2023). Mechanistically, particle formation through speaking and singing is still somewhat uncertain (Johnson and Morawska, 2009; Johnson *et al.*, 2011). Each likely involves two or even three formation mechanisms and sites: (i) laryngeal particle generation, (ii) particle formation through mouth, lip, and tongue movements, and (iii) under vigorous conditions, probably also high-speed shear forces at the ELF-air interface in the trachea (Johnson and Morawska, 2009; Johnson *et al.*, 2011). The breath-related bronchiolar particle formation is involved as an underlying process.

Figure 14 summarizes existing experimental data on speaking- and singing-related particle emissions spanning a wide size range from > 10 nm to ~1000 μm. We found that the generalized parametrization based on five log-normal modes represents the experimental data well; compare this to Sec. III.B. Two of these modes are the bronchiolar modes B1 and B2 since breathing is inherently involved in speaking and singing. Beyond the modes B1 and B2 (located at $D_{B1} = 0.07$ μm and $D_{B2} = 0.3$ μm), a third mode emerges that presumably originates from particle formation in the larynx and trachea [Figs. 14(a) and 14(c)] according to Johnson *et al.* (2011). We call the third mode LT (representing larynx and trachea). Based on the individual NSDs in Fig. 14, the LT mode D_{LT} ranges from 0.7 to 1.5 μm (average: $D_{LT} = 1.0$ μm).[6] In the size range of large particles, the individual PSDs can be described well by either one or two log-normal modes (Fig. 14). As these large droplets presumably originate from mouth, lip, and tongue movements, we refer to them as oral modes O1 and O2 (Johnson *et al.*, 2011). The O1 mode D_{O1} ranges from 8 to 13 μm (average: $D_{O1} = 10$ μm), and the O2 mode D_{O2} is located between 60 and 130 μm (average: $D_{O2} = 96$ μm). A summary of all average fit parameters is given in Table VI. Overall, the five modes have significant overlap and constitute a continuous PSD across more than 5 orders of magnitude in D.

[6]Note that we omitted one outlier at $D_{LT} = 0.45$ μm based on the study by Morawska *et al.* (2009) in this general statement.

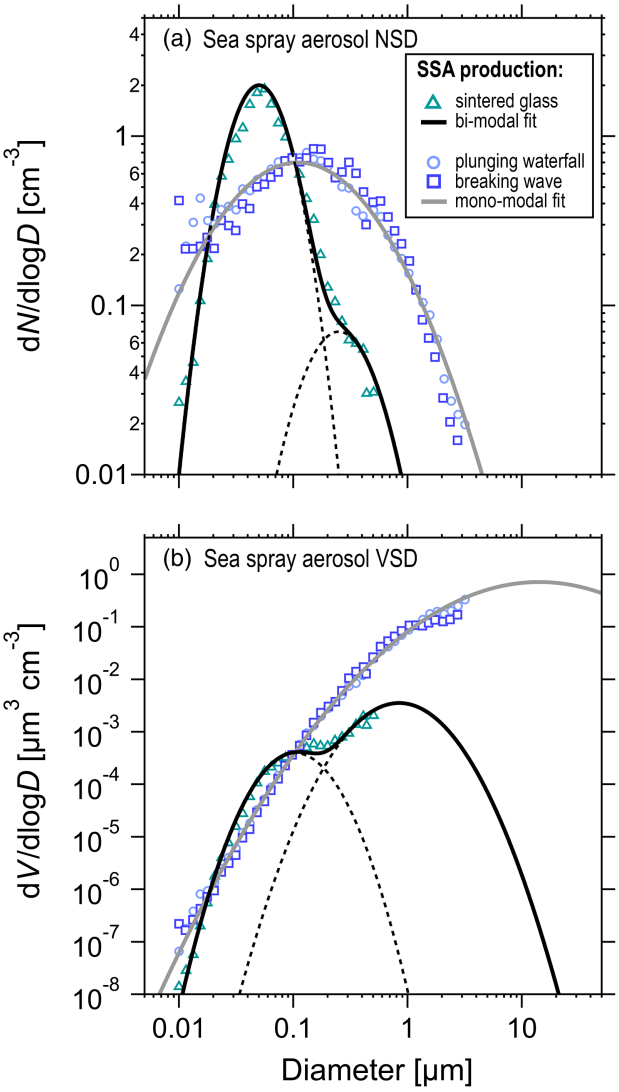

FIG. 13. Number size distribution (NSD) and volume size distribution (VSD) for laboratory-generated sea spray aerosols (SSAs) based on a study by Prather *et al.* (2013) with log-normal fit functions (solid lines). The size distributions were not normalized. The sea spray aerosols of Prather *et al.* (2013) were generated using three different methods: (i) sintered glass, (ii) plunging waterfall, and (iii) breaking waves (see differently colored markers). Note that the PSDs of SSAs react sensitively to the bubble size distributions. Data from plunging waterfall and breaking wave were combined and fitted jointly with monomodal log-normal functions, as size distributions were similar. Sintered glass data were fitted with separate bimodal log-normal fits and share strong similarity with breath aerosol (Fig. 12). The corresponding fit parameters are summarized in Table V.

The parametrizations of speaking- and singing-related PSDs have been developed separately for two size regimes: a small particle range < 5 µm with modes B1, B2, and LT and a large particle range > 5 µm with modes O1 and O2. This two-step approach was chosen because the existing experimental data originate from two groups of instruments that primarily focus on either the small or the large particle regime; compare this to Table VI. Only Johnson *et al.* (2011) and Bagheri *et al.* (2023) provided PSDs across the entire size range. For the small particle range, the data coverage is comparatively good between 0.9 and 5 µm due to the frequent use of the APS (Morawska *et al.*, 2009; Johnson *et al.*, 2011; Asadi *et al.*, 2019; Alsved, Matamis *et al.*, 2020; Gregson *et al.*, 2021). Note here that the original APS size range (i.e., 0.5 and 20 µm) was limited for the reasons outlined in Sec. III.B. Data < 0.9 µm are available from four studies with OPC measurements (Lai, Bottomley, and McNerney, 2011; Hartmann *et al.*, 2020; Mürbe *et al.*, 2021; Bagheri *et al.*, 2023). For the size range primarily focused < 5 µm, we collected 21 speaking-related, 8 singing-related, and 4 shouting-related PSDs. For the size range primarily focused > 5 µm, we collected ten speaking-related, one singing-related, and one shouting-related PSDs; see Table VI. In the parametrization in Fig. 14, the existence and properties of the modes B1 and O1 are more uncertain than those of the modes B2, LT, and O2. For mode B1, the data coverage is sparse and only Bagheri *et al.* (2023) has reported speaking-, singing-, and shouting-related data in the relevant size range. Nevertheless, this article is based on a broad statistical background with more than 130 subjects (Table IV). For mode O1, only a subset of datasets actually resolve this mode (Duguid, 1946; Chao *et al.*, 2009; Morawska *et al.*, 2009; Bagheri *et al.*, 2023), whereas others do not show indications of its presence (Johnson *et al.*, 2011).

In the trimodal log-normal fits of the modes B1, B2, and LT, some of the nine fit parameters had to be fixed because (i) the available experimental data cover only a part of the relevant size range and (ii) the modes are not separately resolved due to significant overlap. Specifically, the parameters D_{B1}, D_{B2}, σ_{B1}, and σ_{B2} were fixed as they were adapted from the average breath PSD in Fig. 12. The only exceptions are three studies (Morawska *et al.*, 2009; Alsved, Matamis *et al.*, 2020; Bagheri *et al.*, 2023) in which the data points resolved parts of the modes B1 and B2 sufficiently well that D_{B2} could also be implemented as a free fitting parameter. Moreover, the ratio $A_{B1}/A_{B2} = 7.0$ for tidal breathing was fixed, whereas the overall height of this bimodal fit for B1 and B2 was a free parameter. For the mode LT, the parameters D_{LT} and A_{LT} were free, whereas σ_{LT} was fixed to 0.9 for reasons outlined in Sec. III.C.1. In the bimodal log-normal fits of the modes O1 and O2, all fit parameters (i.e., D_{O1}, D_{O2}, A_{O1}, A_{O2}, σ_{O1}, and σ_{O2}) were free because the experimental data cover the relevant size range well and the modes O1 and O2 were sufficiently separated. Note also that in these fits, where σ_i was implemented as a free parameter, σ_{O1} and σ_{O2} values close to 0.9 were obtained, which underlines the belief that this log-normal peak width is a good representation for respiration PSD modes overall.

Figure 14 also emphasizes the large variability of mode LT on top of the modes B1 and B2, as visualized with the gray background shading. We found no systematic changes in D_{LT} as a function of speaking or singing activities, suggesting that the mode positions of the trimodal distribution are generally consistent for different speaking and singing activities. In contrast, the ratio A_{B2}/A_{LT} of the heights of the modes B2 and LT varies widely from ≈ 180 (dominated by the breath-related mode B2) to 0.06 (dominated by the speaking- or singing-related mode LT). Overall, the ratio A_{B2}/A_{LT} of the speaking- and singing-related PSDs in Fig. 14 appears to be associated

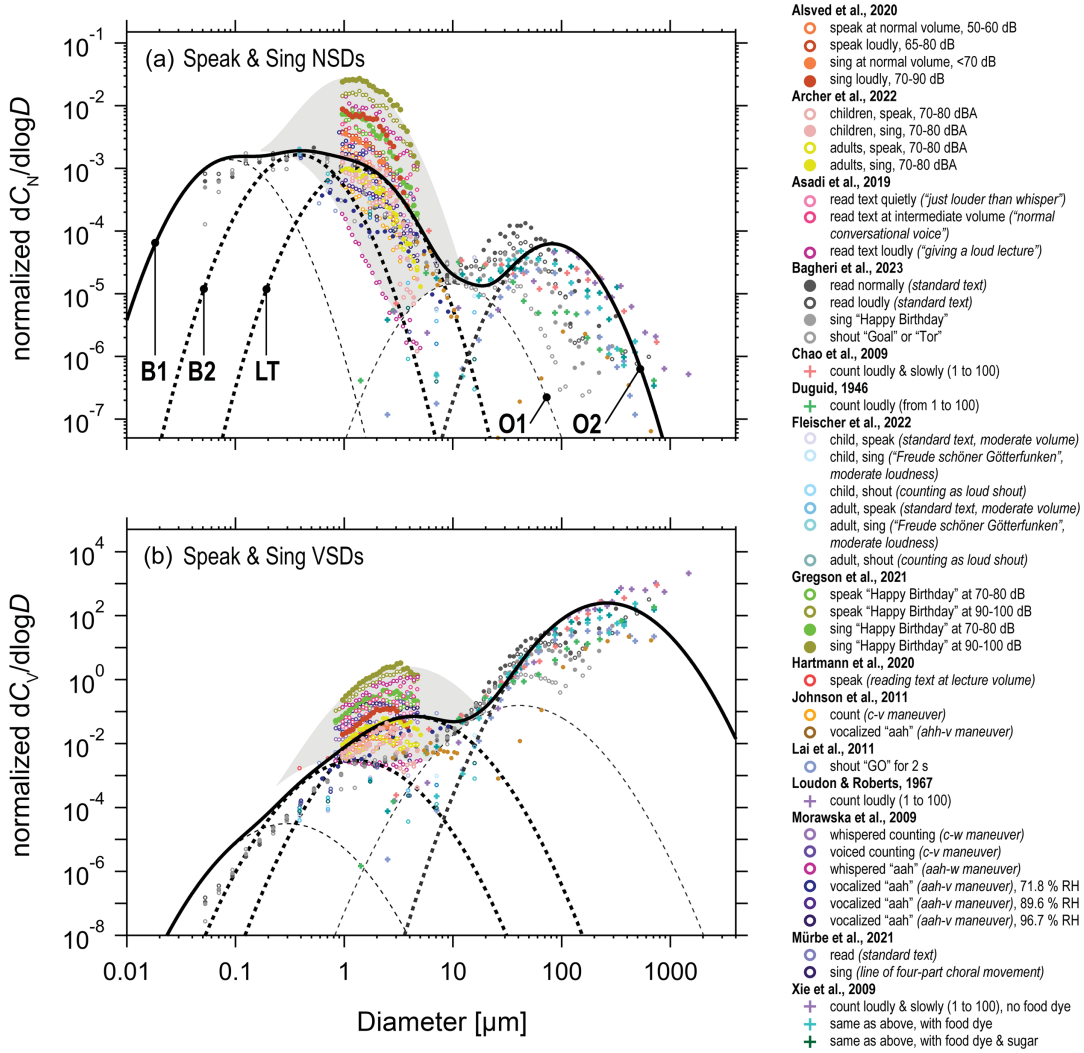

FIG. 14. Combined literature data on speaking- and singing-related particle (a) NSDs and (b) VSDs with parametrizations based on five log-normal modes. The dashed black lines show the five individual modes and the solid black line shows the average multimodal fit, which represents the average of all fit parameters of the individual PSDs in the legend. The dashed lines of underlying modes B2, LT, and O2 are thicker than those of the other modes to show that the experimental uncertainty is smaller here. All PSDs were normalized here for comparability. (i) Those SDs centered < 5 µm and primarily covering the modes B1, B2, and LT were described by a trimodal log-normal fit and normalized to the integral of the B1 and B2 modes; see Fig. 11. (ii) Those PSDs centered > 5 µm and primarily covering the modes O1 and O2 were described by monomodal or bimodal log-normal fits and related to the integral of the B1 and B2 modes with the data from Bagheri *et al.* (2023), which allows one to bridge both groups of PSDs, as it covers the entire size range. The gray shading emphasizes the variability of the LT mode. The legend summarizes information on the specific speaking and singing activities conducted in the individual studies. For further details, refer to the original articles.

with the vigor of the speaking or singing activities, which is in line with previous evidence (Asadi *et al.*, 2019; Gregson *et al.*, 2021).

Mode O2 was found for all individual PSDs in Fig. 14. The presence of mode O1 is less conclusive, though. It was resolved in multiple studies (Duguid, 1946; Loudon and Roberts, 1967a; Chao *et al.*, 2009; Bagheri *et al.*, 2023) and appeared to be absent in others (Johnson *et al.*, 2011). Xie *et al.* (2009) reported three average PSDs, with mode O1 clearly resolved in one and absent in the other two. The PSDs there were investigated in relation to the use of food dye in the mouth for better microscopic detection of settled particles. The study suggests that mode O1 was present when sugar and dye were used, whereas mode O1 was absent when no dye was used. In this case, these differences in the PSDs based on the same experimental approach suggest that the presence of mode O1 might indeed either depend on differences in characteristics such as saliva composition or reflect experimental uncertainties, such as that the comparatively small particles are more easily detected with than without dye. For PSDs with a resolved mode O1, the ratio of the mode heights A_{O1}/A_{O2} varied from ~10 for Duguid (1946) to ~0.14 for Xie *et al.* (2009). Generally, the ambiguous findings on mode O1 can potentially be explained by either experimental issues such as particle drying dynamics and, therefore, observations in different nonequilibrium states or different sensitivities of the instruments used in this particular size range. Further, the variable appearance of mode O1 could potentially also be

caused by a mechanistic difference in the course of droplet formation in the mouth. Evidently, further studies are needed to extend our knowledge on speaking- and singing-related emission in this large particle range.

Regarding the drying dynamics and measurements under nonequilibrium states, Fig. 4(b) shows that the evaporation times of particles in the smaller modes B1, B2, and LT are comparatively short, which implies that these particles were likely dried to a significant extent under the experimental conditions of most of the studies in Table IV. For the particles in the larger modes O1 and O2, however, Fig. 4(b) shows comparatively long evaporation times, especially if the evaporation delays shown by Chong *et al.* (2021) are taken into account, which implies that these particles were likely measured under nonequilibrium conditions. Accordingly, these kinetic effects probably entail that the extent of drying decreases from mode B1 to mode O2. For Fig. 14, this presumably entails that the modes O1 and O2 are shifted to larger diameters and would move closer to the mode LT if they were dried to the equilibrium state under the given RH conditions.

3. Coughing and sneezing

Coughing is caused by an abrupt parting of the vocal folds and an associated sudden expulsion of air (Grotberg, 2001; Morawska *et al.*, 2009). Sneezing is a sudden violent spasmodic expiration with a blast of air being driven through the nasal and mouth chambers (Brubaker, 1919; Han, Weng, and Huang, 2013; Fontes *et al.*, 2020). Both are short, noncontinuous, and vigorous respiratory activities associated with an ejection of ELF and saliva. Traditionally they have been regarded as main drivers of pathogen transmission (Bourouiba, Dehandschoewercker, and Bush, 2014; Dhand and Li, 2020). Like speaking and singing, (i) laryngeal aerosol generation, (ii) droplet formation through mouth, lip, and tongue movements, and (iii) high-speed shear forces at the ELF-air interface in the trachea and main bronchi are probably the relevant formation mechanisms and sites (Johnson and Morawska, 2009; Johnson *et al.*, 2011; Patterson and Wood, 2019). The breath-related bronchiolar particle formation is involved as an underlying process. Compared to breathing and speaking, the available data on coughing- and sneezing-related particle formation are relatively sparse: for the size range < 5 μm, we found five PSDs from five studies for coughing and no PSDs for sneezing. For the size range > 5 μm, we found five PSDs from five studies for coughing and one PSD for sneezing.

Figure 15 summarizes the experimental data on cough-related particle emissions in the size range from > 10 nm to ∼1000 μm. The PSD shape is similar to the speaking- and singing-related PSDs and can also be described with five log-normal modes (Fig. 14). In addition to the bronchiolar modes B1 and B2, the LT mode emerges, as in the cases of speaking and singing. The LT mode D_{LT} is located between 0.8 and 1.2 μm (average: $D_{LT} = 1.0$ μm). The mode height ratio A_{B2}/A_{LT} ranges from 20 to 7.5 and is therefore higher than the ratio A_{B2}/A_{LT} for speaking- and singing-related PSDs, which means that the cough-related mode LT is weaker than the speaking- and singing-related mode LT relative to mode B2 (at least within the scope of the data reviewed here).

The large particle size range can be represented by two oral modes O1 and O2 as with speaking and singing (Johnson *et al.*, 2011). The O1 mode D_{O1} is located between 8 and 13 μm (average: $D_{O1} = 11$ μm). The O2 mode D_{O2} is located between 90 and 200 μm (average: $D_{O2} = 128$ μm). The mode height ratio A_{O1}/A_{O2} is variable, ranging from 0 (Duguid, 1946) to ∼16 (Loudon and Roberts, 1967a, 1967b). As with speaking and singing, the mode O2 is present in all five studies, whereas the mode O1 is present in three studies (Duguid, 1946; Loudon and Roberts, 1967a; Chao *et al.*, 2009) and absent in two studies (Xie *et al.*, 2009; Johnson *et al.*, 2011). The PSD for sneezing for the large particle size range based on the work of Duguid (1946) shows the mode positions $D_{O1} = 8$ μm and $D_{O2} = 130$ μm as well as a mode height ratio $A_{O1}/A_{O2} = 48$. A summary of all average fit parameters is given in Table VI.

A noteworthy observation involves the similarity between speaking- and singing-related versus coughing-related PSDs in terms of the properties of all five modes; compare Figs. 14 and 15. This suggests that for both respiratory activities the modes LT, O1, and O2 are formed by the same (or at least similar) mechanisms in the respiratory tract. Another notable observation is that the sneezing-related PSD in Figs. 15(b) and 15(d) resembles the corresponding coughing-related PSDs. At least in the range of modes O1 and O2, the two respiratory activities can be described with a similar PSD, at least within the scope of data in Fig. 15. Note that PSD data on sneezing are generally sparse. In addition to Duguid (1946), Han, Weng, and Huang (2013) also reported sneeze PSDs, which, however, could not be implemented in Fig. 15 due to difficulties with normalization.[7] Nevertheless, qualitatively the data from Han, Weng, and Huang (2013) were mostly consistent with Fig. 15, as about half of the their PSDs showed a bimodal PSD with one mode at ∼70 μm, which corresponds to mode O2. In their data, another mode was reported at ∼400 μm, indicating the presence of an additional mode O3, although comprising low particle concentrations. The other half of PSDs given by Han, Weng, and Huang (2013) were monomodal, showing mode O3 only.

D. Number concentrations and emission rates

Sections III.C.1–III.C.3 focused on the shape of the PSDs and developed a consistent parametrization of their multimodal character. We used the multimodal parametrization to calculate and summarize the statistics of the mode-specific properties in Fig. 16, such as number and volume concentrations (C_N and C_V) as well as number and volume emission rates (Q_N and Q_V) based on the available studies with quantitative PSDs (flag A in Table IV); see also Fig. 10. Consistent with previous studies (Xie *et al.*, 2009; Holmgren *et al.*, 2010; Schwarz *et al.*, 2015; Bake *et al.*, 2017; Asadi *et al.*, 2019; Gregson *et al.*, 2021; Mürbe *et al.*, 2021; Archer

[7]Since the area under mode O2 was used for normalization in Figs. 15(b) and 15(d) and not all PSDs of Han, Weng, and Huang (2013) showed mode O2, the data could not be consistently normalized. Furthermore, the PSDs were provided only in relative and not in absolute terms so that no mode-specific particle number and volume concentrations could be retrieved for the further steps of our analysis.

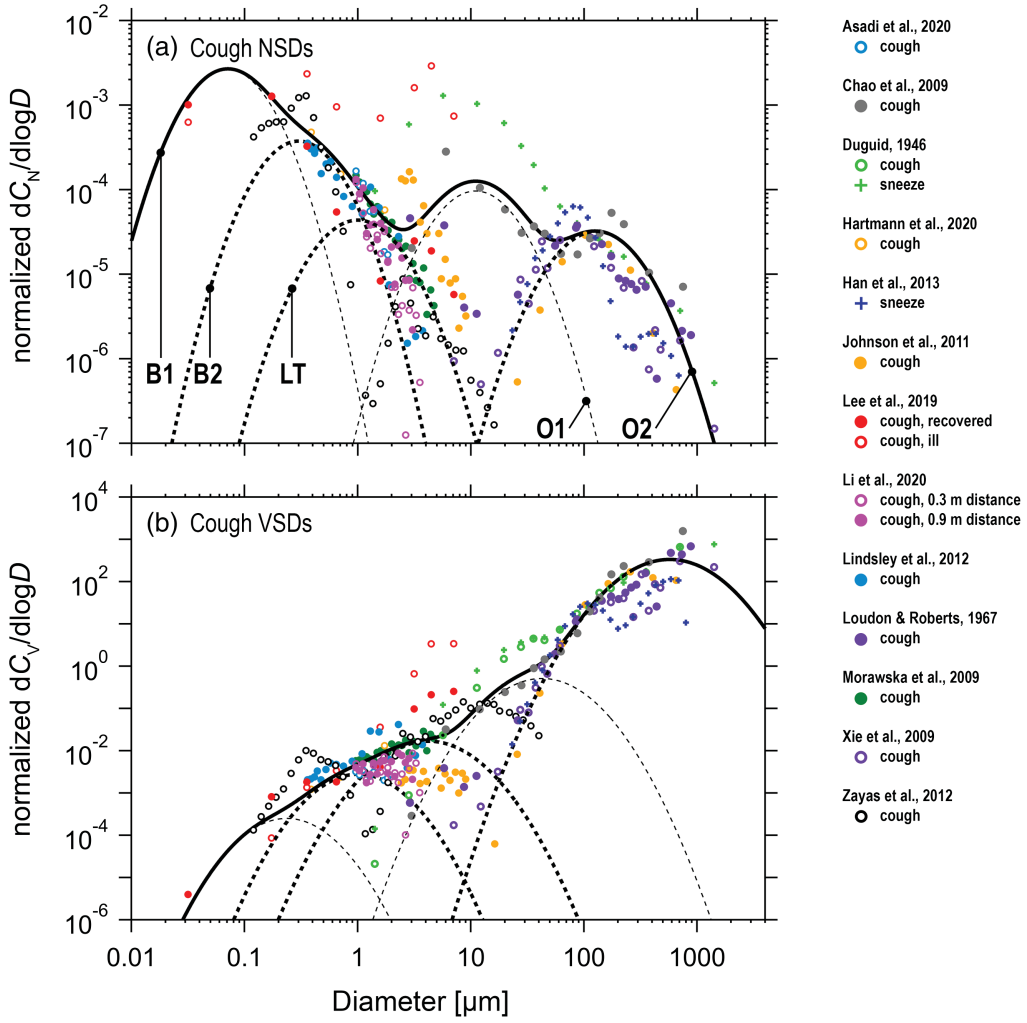

FIG. 15. Combined literature data on (a) cough-related particle NSDs with (b) calculated VSDs and a multimodal log-normal parametrization. The dashed black lines show the five underlying modes, while the solid black line displays the average multimodal fit as the average of all fit parameters of the individual PSDs in the legend; see also Fig. 10 and Table VI. Generally, cough-related PSDs show more scattering in the original data than speaking- and singing-related PSDs (Fig. 14). The dashed lines for modes B2, LT, and O2 are drawn thicker to indicate their higher experimental certainty compared to modes B1 and O1. All individual PSDs were normalized here for comparability. (i) Those PSDs centered < 5 µm and primarily covering the modes B1, B2, and/or LT were described by a trimodal log-normal fit and normalized to the integral of the modes B1 and B2; see Fig. 11. (ii) Those PSDs centered > 5 µm and primarily covering the modes O1 and O2 were described by monomodal or bimodal log-normal fits and normalized to the integral of mode O2. The work of Johnson *et al.* (2011) has allowed us to relate the two size ranges.

et al., 2022), the obtained C and Q levels are highly variable and span across several orders of magnitude. The large variability in Q among infected individuals has been considered as a potential explanation for the existence of superspreaders in infectious disease transmission, as they emit much more potentially pathogen-laden particles than others (Bischoff *et al.*, 2013; Asadi *et al.*, 2019; Edwards *et al.*, 2021; Bagheri *et al.*, 2023).

On average, the highest C_N and Q_N levels were found for the modes B1 and B2, which then decrease via mode LT to modes O1 and O2. The opposite trend (an increase from mode B1 to O2) was found for C_V and Q_V since the volume scales with D^3, and therefore overcompensates for the decreasing trend in number representation. Note here that modes B1 and O1 are associated with higher uncertainties than the other modes, as previously outlined. Figure 16(f) shows the comparatively low variability of the peak position of individual modes and further emphasizes that some modes (i.e., B2 and LT) overlap significantly, whereas others (i.e., O1 and O2) appear to be rather well separated. The ratio $C_N(i)/C_N(i+1)$ in Fig. 16(c) shows that the variability of the relative strength of individual modes is high; compare this with Secs. III.C.2 and III.C.3).

The particle concentration and emission flux for a given respiratory activity are both relevant quantities for a better understanding of airborne disease transmission, which can in principle occur in the near field or far field (Fig. 1). Figure 17 provides total C and Q levels for selected particle size ranges to emphasize the relative importance of breathing, speaking, and coughing in near- and far-field scenarios of disease transmission.

In a potential near-field aerosol transmission scenario, the recipient is located close (a few meters) to the emitter and

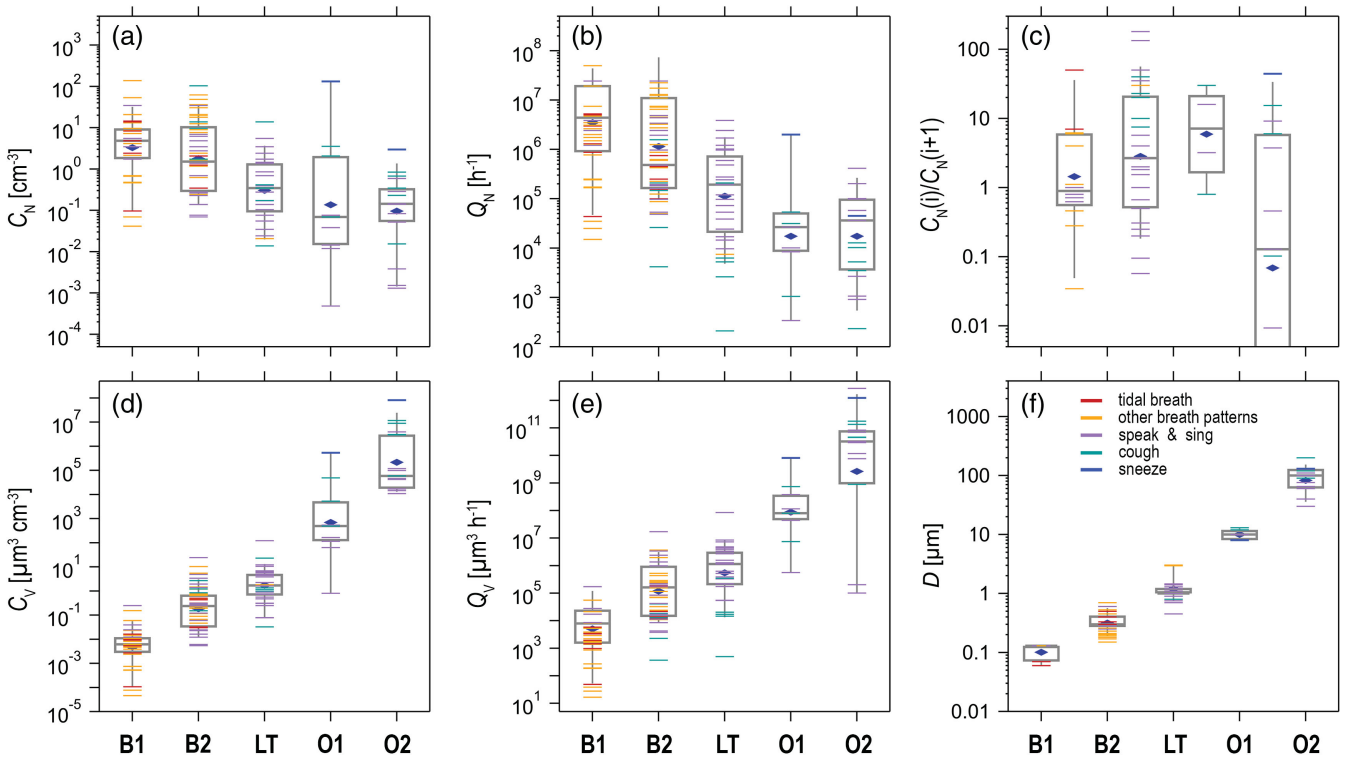

FIG. 16. Statistical summary of mode-specific particle concentrations (C), emission rates (Q), and peak diameters (D) for individual modes B1, B2, LT, O1, and O2. Only markers for modes that are well constrained by PSDs in the relevant size range are shown. The wide variability of C and Q across several orders of magnitude is illustrated. Particle concentrations and emission rates are provided for number and volume (C_N vs C_V and Q_N vs Q_V). Further, the ratios of C_N of adjacent modes [$C_N(i)/C_N(i+1)$] derived from individual studies with PSD data covering two or more modes [i.e., $C_N(B1)/C_N(B2)$, $C_N(B2)/C_N(LT)$, $C_N(LT)/C_N(O1)$, and $C_N(O1)/C_N(O2)$] are shown. Colored markers (short vertical lines) distinguish between respiratory activities (see the legend). In the box-whisker plots, the boxes represent the 25 and 75 percentiles, the gray lines indicate the medians, the blue diamond markers represent the means, and the whiskers indicate the 9 and 91 percentiles.

inhales her or his concentrated particle puff(s) relatively soon after release [Fig. 17(a)]. Thus, the time span between emission and inhalation is presumably too short for particle cloud dilution as well as large particle sedimentation to occur to a significant degree. Within the simplified picture of an expanding conical jet as an imperfect first-order approximation, the aerosol concentration is inversely proportional to the square of the distance between emitter and recipient (Poydenot *et al.*, 2022). Thus, Figs. 17(b) and 17(c) compare the total C_N and C_V levels for the size range from 0.1 to 100 µm. Here 0.1 µm was chosen as a lower limit since it is the physical size of SARS-CoV-2 and infuenza virions; see Sec. III.E. Coughing as well as, presumably, sneezing (not shown here due to sparse data availability) causes the highest concentrations in the near-field aerosol cloud. For C_N in the $0.1-100$ µm range, coughing clearly exceeds breathing, which is closely followed by speaking. For C_V in the $0.1-100$ µm range, coughing is highest, comparatively closely followed by speaking, with breathing being significantly smaller. These trends in number and volume representation result from the differences in the multimodal shape of the corresponding PSDs and have to be considered in the choice of either C_N or C_V for risk assessments.

In a potential far-field aerosol transmission scenario, an infected individual emits pathogen-laden particles, which can accumulate over time in confined spaces, such as in a restaurant room or on public transport [Fig. 17(d)] (Birnir and Angheluta, 2020; Kohanski, Lo, and Waring, 2020; Lelieveld *et al.*, 2020; Azimi *et al.*, 2021; Hwang *et al.*, 2021). Whether critical pathogen concentrations can build up in room air depends on multiple factors, such as source strength, particle size, room size, and ventilation rates; see Lai (2002), Riley *et al.* (2002), Nazaroff (2016), Helleis, Klimach, and Pöschl (2021), Poydenot *et al.* (2022), and references therein. Infection risks depend on the airborne pathogen concentrations, exposure times, and the recipient's susceptibility. The source strength, which is the particle number Q_N or volume emission rate Q_V as a function of respiratory activity, is of primary relevance. Previous studies have reported a high variability in Q_N. For example, (i) Alsved, Matamis *et al.* (2020) reported for particle sizes 0.5–10 µm $Q_N = 4.9 \times 10^5$ h^{-1} for breathing, ~20.5×10^5 h^{-1} for loud speaking, and 24.8×10^5 h^{-1} for loud singing. (ii) Mürbe *et al.* (2021) reported for particle sizes 0.3–10 µm $Q_N = 0.2 \times 10^5$ h^{-1} for breathing, ~2.4×10^5 h^{-1} for speaking, and 55×10^5 h^{-1} for singing. (iii) Archer *et al.* (2022) reported for particle sizes 0.5–10 µm $Q_N = 0.1 \times 10^5$ to 0.7×10^5 h^{-1} for breathing, 1.4×10^5 to 3.6×10^5 h^{-1} for speaking, and 2.5×10^5 to 7.2×10^5 h^{-1} for singing.

Figure 17(e) and 17(f) provides average Q_N and Q_V values based on the studies with flag A in Table IV, as well as the

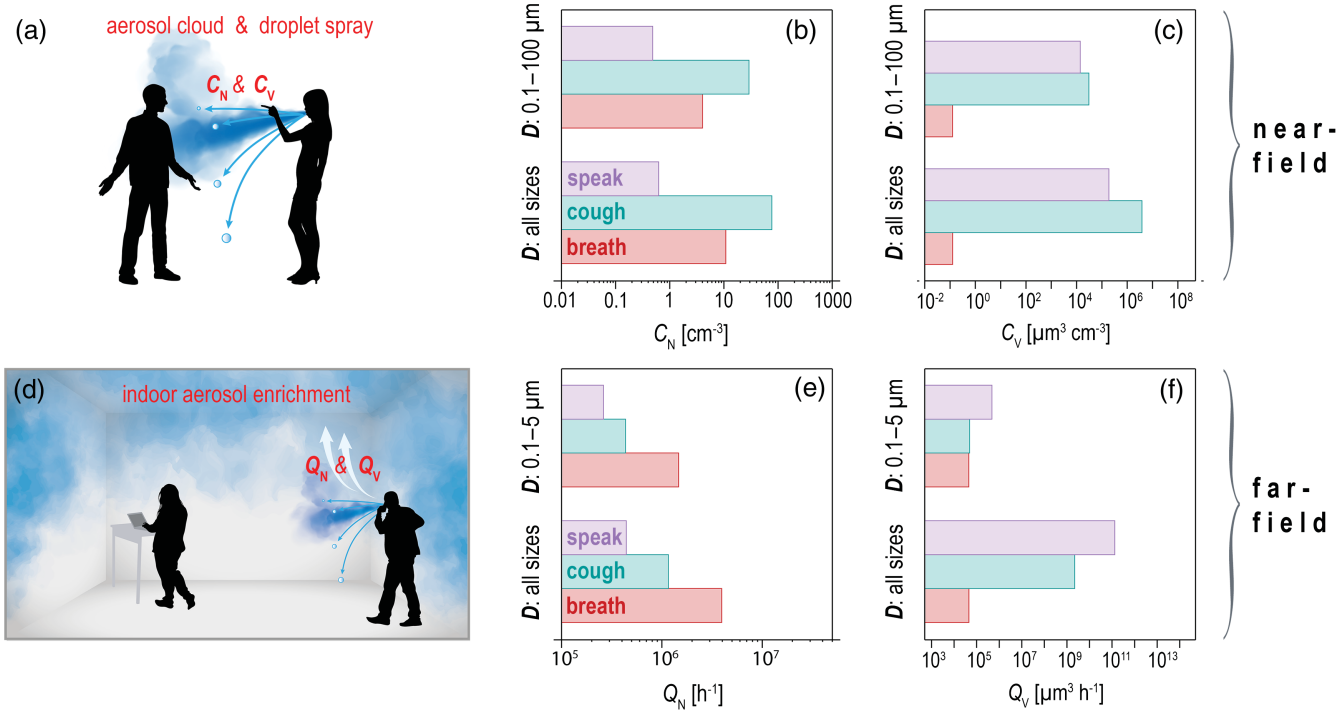

FIG. 17. Total number and volume concentrations (C_N and C_V) as well as emission rates (Q_N and Q_V) of exhaled particles for different respiratory activities. Two different particle size ranges were chosen to compare conditions under near- vs far-field disease transmission scenarios: (a)–(c) First, in the near field C_N and C_V in the exhaled puff(s) prior to dilution and dissipation are primarily relevant. Here a lower threshold of 0.1 µm (typical size of virus pathogens; Fig. 19) and an upper threshold of 100 µm (upper limit of common aerosol definitions; see Sec. II.A) were chosen. (d)–(f) Second, in the far field Q_N and Q_V are primarily relevant, especially if emission extends over longer periods. Here a lower threshold of 0.1 µm and an upper threshold of 5 µm (particles below this threshold have a particularly long residence time in air; Fig. 2) were chosen. In addition, C and Q across the entire size range of the parametrization (i.e., $0.002 - 4000$ µm) are shown in all cases for reference. The total C_N and C_V as well as Q_N and Q_V values were derived as the integral under the non-normalized and averaged multimodal NSDs and VSDs based on all flag A studies in Table IV; see also Fig. 10.

respiratory parameters in Table I. To emphasize the different source strengths of breathing, speaking, and coughing, we focus on the $0.1 - 5$ µm particle size range, which comprises those particles with particularly long airborne residence times. Figure 17(e) shows that in a far-field scenario breathing dominates in Q_N in the $0.1 - 5$ µm range, followed by coughing and then speaking. Figure 17(f) shows that speaking dominates in Q_V in the $0.1 - 5$ µm range, followed by coughing and then breathing. The high values for speaking in C_V and Q_V suggest that speaking might be a particularly important driver for airborne transmission, as it represents a comparatively strong particle source and occurs more frequently and continuously than, for instance, coughing. This is consistent with the conclusions of previous studies (Asadi *et al.*, 2019; Gregson *et al.*, 2021; Mürbe *et al.*, 2021; Archer *et al.*, 2022). Note further that the transmission of SARS-CoV-2 occurs to a significant extent presymptomatically or even asymptomatically: recent studies estimate the fraction of such transmission events as between 40% and 80% (Tindale *et al.*, 2020; Johansson *et al.*, 2021; Kang *et al.*, 2022). This further diminishes the supposed relevance of coughing as a disease symptom and emphasizes the supposed importance of speaking. Note, however, that all these studies were conducted under laboratory conditions with partially artificial respiratory maneuvers, so uncertainty remains as to what extent the results reflect real life conditions.

E. Multimodality of size distributions in airborne disease transmission

Figure 18 combines the main findings of this review and data synthesis and emphasizes that a detailed understanding of the multimodal shape of the respiration PSDs provides mechanistic insights into airborne disease transmission and the effectiveness of preventative measures (Johnson *et al.*, 2011). An important parameter for the transport of viruses, bacteria, and bacterial or fungal spores by respiratory particles is the pathogen's size. Figure 18(a) summarizes the size of selected aerosol-transmissible pathogens, such as rhinoviruses (one of the agent groups causing the "common cold") (Pitkäranta and Hayden, 1998; Fabian *et al.*, 2011), measles morbilliviruses (Liljeroos *et al.*, 2011), SARS-CoV-2 (Ke *et al.*, 2020; Yao *et al.*, 2020; Zhu *et al.*, 2020), influenza viruses (Mosley and Wyckoff, 1946; Rossman and Lamb, 2011; Enoki *et al.*, 2012), and *M. tuberculosis* (Schafer, 1999). The pathogen size defines a principle lower limit for the respiratory particle size range that is relevant for pathogen transport, although the actual lower limit for effective pathogen incorporation into the carrier particles might be significantly higher. Figures 18(b) and 18(c) combine the parametrizations for different respiratory activities in relation to the average mode-specific emission rates from Figs. 16 and 17. The breath-related

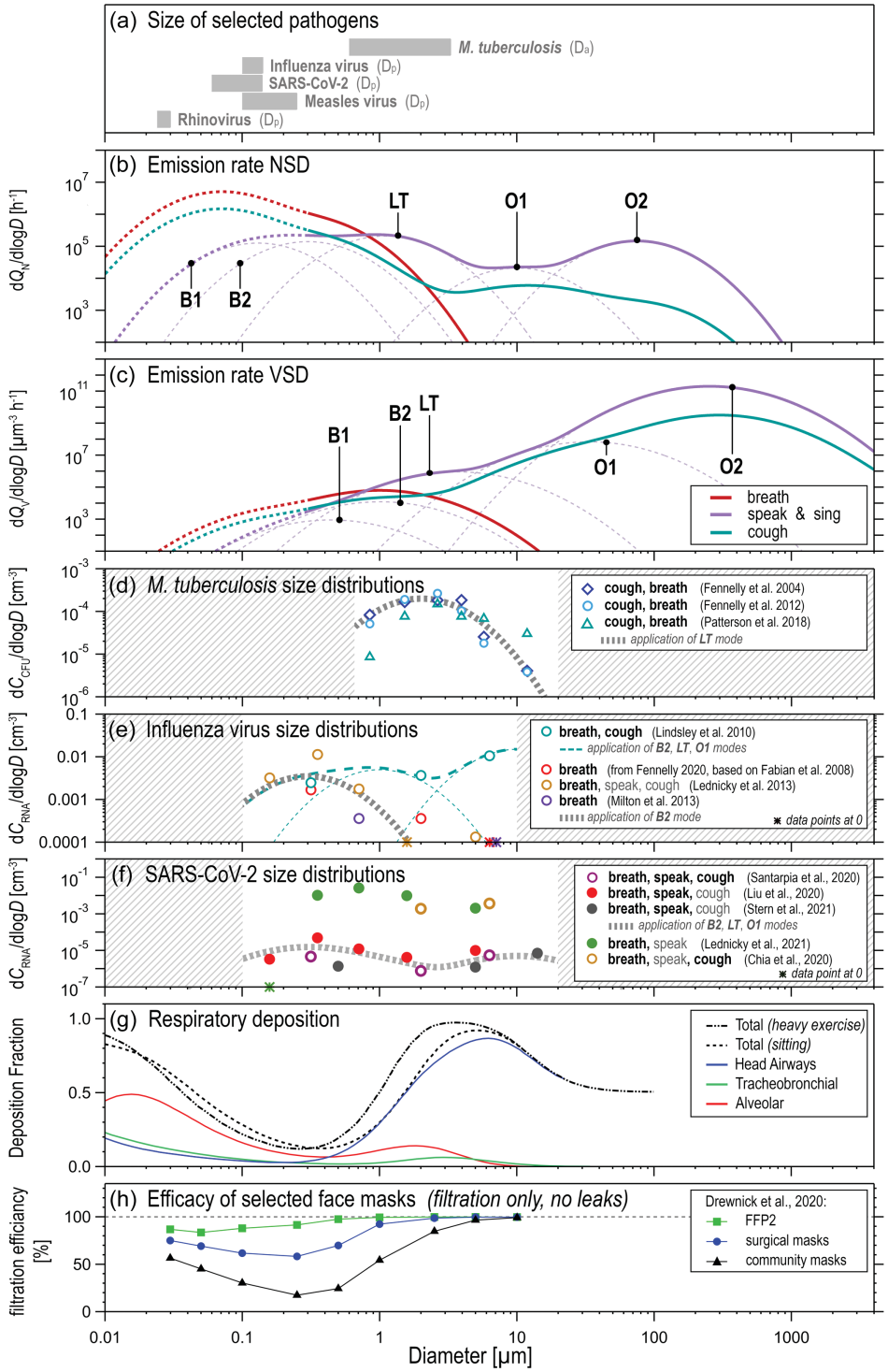

FIG. 18. Synthesized data emphasizing the relevance of the multimodal character of the exhaled particle size distribution (PSD) in airborne disease transmission. (b),(c) PSD parametrization combined with the size of selected pathogens (physical diameter D_p for all viruses and aerodynamic diameter D_a for *M. tuberculosis*) as a lower limit for (a) pathogen carriage, (d)–(f) measured size distributions of pathogen-carrying respiratory particles, (g) deposition properties of the respiratory tract (the ICPR model), and (h) filtration efficacy of face mask materials. Note that the mode properties of B1 and O1 are more uncertain than those of B2, LT, and O2; see Secs. III.C.2 and III.C.3. (d)–(f) The size distributions of pathogen-laden particles were obtained from the original studies (see the legend), bin normalized, and converted into pathogen entities per air volume. The legend further specifies involved respiratory activities (bold, black font) and activities that might be involved as well (gray font). The parametrization was applied to the size distributions of pathogen-laden particles by adapting the position(s) and width(s) of modes B2, LT, and O1 (with only slight changes) and freely adjusting the mode height(s). (h) Filtration efficiencies of face mask materials were measured at high air velocity, with surgical mask transmissibility representing the average of three types of surgical masks and community mask transmissibility representing the average of three materials: velvet polyester, two layers of cotton jersey, and thin silk. The data from Drewnick *et al.* (2021) are shown here as a particularly notable study.

bimodal PSD is shown in relation to the speaking- and singing-related as well as cough-related pentamodal PSDs, yielding a coherent overall picture. The comparison shows that all viruses in Fig. 18(a) are in principle small enough to be transmitted via all five modes. For the larger *M. tuberculosis*, the modes B1 and B2 can presumably be excluded as potential carriers, which leaves the modes LT, O1, and O2 for transmission.

A fundamental property in this context is the size range of the overall PSD, which is laden primarily with the pathogens and is therefore most relevant for disease transmission; see Fennelly (2020) and references therein. In principle, the distribution of pathogen-laden particles can either resemble the NSD or the VSD of the carrier particle population or be shaped in a modal pattern; see also Sec. II.B.2. Different strategies have been applied to investigate the incorporation or entrainment probability of pathogens into the respiratory carrier particles upon emission. Following statistical approaches, Anand and Mayya (2020) and Madas *et al.* (2020) applied Poisson probability distributions to assess the pathogen loading across the entire carrier particle size range and argue that the probability of particles containing pathogens strictly scales with the volume. This approach, however, is based on the simplified assumption that a polydisperse PSD is aerosolized from the same batch of an aqueous pathogen suspension, while the aerosolization in the human respiratory tract likely occurs in different particle formation mechanisms and sites in relation to the actual site of infection (Sec. II.D). Laboratory studies have also reported that virus or bacteria incorporation probabilities scale with the VSD of the carrier particles (Gerone *et al.*, 1966; Hogan *et al.*, 2005; Appert *et al.*, 2012; Zuo *et al.*, 2013). It is unlikely, however, that *in vitro* approaches with laboratory aerosolization techniques, such as the Collison nebulizer, mimic the aerosolization conditions in the respiratory tract, and therefore yield insights into the actual properties of respiratory aerosol formation (Zuo *et al.*, 2013). Probably the most informative approach is size-resolved sampling of pathogen-laden aerosols that are emitted from infected individuals. Some but not many studies have provided data from such experiments. *In vivo* studies on human (Fabian *et al.*, 2008; Lindsley *et al.*, 2010b; Fennelly *et al.*, 2012; Bischoff *et al.*, 2013; Patterson *et al.*, 2018) and animal emissions (Alonso *et al.*, 2015, 2017; Bekking *et al.*, 2019) suggest that the pathogen loading in most cases does not strictly scale with the VSD of the carrier aerosol. Instead, and contrary to statistical probability, significant pathogen loads were found in the smallest particle size bins, down to 500 nm or even smaller (Wainwright *et al.*, 2009; Fennelly *et al.*, 2012; Alonso *et al.*, 2015). Note, however, that pathogen availability is not necessarily related to pathogen viability. A summary of the studies on *M. tuberculosis*, influenza virions, and SARS-CoV-2 virions follows.

Experimental data on the actual size distributions of pathogen-laden carrier aerosols, which were introduced in Sec. II.B.3, are sparse since they are difficult to obtain. The available data from size-resolved sampling of airborne *M. tuberculosis*, influenza virions, and SARS-CoV-2 virions are shown in Figs. 18(d)–18(f). Generally, the available data suggest that these pathogens are enriched in a certain size range of the overall PSD, which presumably reflects the sites of infection and particle formation in the respiratory tract. Note, however, that the number of existing studies is small and certain parts of the overall size range (i.e., > 10 μm) have not yet been investigated with size-resolved sampling approaches.[8]

A comparison of the size distributions of pathogen-carrying particles from different aerosol samplers with different numbers and definitions of the size bins requires a normalization to the bin width [for details see Seinfeld and Pandis (2016)]. For some of the studies summarized in Figs. 18(d)–18(f), the upper limit of the largest size bin and the lower limit of the smallest bin are not specified, mostly because the design of the samplers do not provide defined size cutoffs as upper and lower bounds. Santarpia *et al.* (2022) used the NIOSH sampler and reported the three size bins of the pathogen-laden PSD as < 1, 1–4, and > 4.1 μm. We assume upper and lower bounds here as follows: (i) The lower size threshold of the smallest bin is given by the average size of the pathogen, which here is SARS-CoV-2 virions with 0.1 μm. (ii) The upper size threshold of the largest bin is not clearly defined. Liu *et al.* (2020) and Lednicky *et al.* (2021) used 10 μm as the upper limit of the largest bin. For consistency, we followed this definition and used 10 μm as well for the other influenza- and SARS-CoV-2–related studies (Lednicky and Loeb, 2013; Milton *et al.*, 2013; Chia *et al.*, 2020; Santarpia *et al.*, 2022). Further, a sensitivity test was conducted by comparing 10 and 20 μm as upper bounds, showing that within this range the bin width-normalized concentrations are not affected significantly. With this approach, the bin widths of Santarpia *et al.* (2022) are 0.1–1, 1–4, and 4.1–10 μm. The corresponding geometric means, which are commonly used as bin centers (Seinfeld and Pandis, 2016) and were used for the plotting in Fig. 18, are 0.32, 2.0, and 6.4 μm. For the other datasets in Figs. 18(d)–18(f), the same approach was applied.

Under the assumption that airborne pathogen transmission is driven by specific respiratory activities and their associated PSD modes, we applied the previously defined parametrization to the size distributions of pathogen-laden particles. Specifically, we described the size-resolved concentrations of the pathogen-laden particles [i.e., ribonucleic acid (RNA) copies for virions and a culture forming unit for *M. tuberculosis*] using the previously defined mode properties; see Table VI. Here the position D_i and width σ_i of the mode(s) were mostly

[8]Different aerosol samplers were used in the studies summarized in Figs. 18(d)–18(f): (i) the Sioutas five-stage personal cascade impactor (SKC, Inc.) [described by Misra *et al.* (2002) and Singh, Misra, and Sioutas (2003) and used by Lednicky and Loeb (2013), Liu *et al.* (2020), and Lednicky *et al.* (2021)]; (ii) the cascade cyclone of the National Institute for Occupational Safety and Health (NIOSH) sampler [described by Cao *et al.* (2011) and used by Lindsley *et al.* (2010b), Chia *et al.* (2020), and Santarpia *et al.* (2022)]; (iii) the Andersen six-stage cascade impactor [described by Fennelly *et al.* (2015) and used by Fennelly, Martyny *et al.* (2004), Fennelly *et al.* (2012), and Patterson *et al.* (2018)]; (iv) a two-stage slit impactor with an intermediate condensational growth step as part of the G-II sampling setup [described by McDevitt *et al.* (2013) and used by Milton *et al.* (2013)]; and (v) other custom-built samplers (Stern *et al.*, 2021). Strengths and limitations of the individual sampling approaches have to be kept in mind when results are compared [further information was given by Mainelis (2020)].

constrained and only slightly adjusted, whereas the number of modes (one or two) as well as their heights A_i were scaled to best represent the size distributions of pathogen-carrying particles. The size distributions could be described consistently with one to three of the modes B2, LT, and O1. This approach holds uncertainties, due especially to the small number of datasets as well as the comparatively coarse size resolution (for instance, three to six size bins only). Nevertheless, Figs. 18(d)–18(f) show conceptually that the size distributions of the pathogen-carrying particles can be described using an underlying modal structure in agreement with the overall PSD parametrization.

M. tuberculosis in Fig. 18(d) was sampled by Fennelly, Martyny *et al.* (2004), Fennelly *et al.* (2012), and Patterson *et al.* (2018) from infected and coughing individuals, and the resulting size distributions of pathogen-laden particles can be fitted well by the cough-related mode LT. The agreement between the *M. tuberculosis* size distributions and the mode LT is consistent; see also Fennelly (2020). The *M. tuberculosis* size distribution decreases toward the modes B1 and B2, which is consistent with the fact that those exhaled particles are too small for pathogen transport. Moreover, the *M. tuberculosis* size distribution decreases (rather steeply) toward the modes O1 and O2, which suggests that these modes may not play a primary role in TB transmission. Keep in mind, however, that large particles are particularly prone to impaction and sedimentation losses in the sampling setup, and that the potential influence of such sampling artifacts on the shape of the size distributions of pathogen-laden particles has to be critically evaluated (von der Weiden, Drewnick, and Borrmann, 2009; Mainelis, 2020; Niazi, Groth, Spann, and Johnson, 2021).

The size distributions of airborne influenza virions obtained from breathing (Fabian *et al.*, 2008; Milton *et al.*, 2013; Fennelly, 2020) and coughing individuals (Lindsley *et al.*, 2010b) as well as from mixed respiratory activities (Lednicky and Loeb, 2013) are shown in Fig. 18(e). The breath-related influenza size distributions suggest a predominance of mode B2 without strong contributions by the mode LT. Furthermore, consistent with Sec. III.C.3 is that the cough-related influenza size distribution involves the mode B2 as well as the modes LT and O1, which both occur in relation to coughing; see also Fennelly (2020). The low size resolution bears large uncertainties regarding the relative contributions from the modes LT and O1. The upper size limit of the sampling at ∼10 μm does not allow solid conclusions on the influenza abundance in the modes O1 and, particularly, O2. Overall, these results underline previous observations of influenza virions, especially in the small aerosol size range and emphasize that essentially all respiratory activities might be driving forces in the spread of this virus (Bischoff *et al.*, 2013; Cowling *et al.*, 2013; Milton *et al.*, 2013; Yan *et al.*, 2018; Leung *et al.*, 2020; Shiu *et al.*, 2020).

The five available SARS-CoV-2 size distributions with at least two size bins based on studies by Chia *et al.* (2020), Liu *et al.* (2020), Lednicky *et al.* (2021), Stern *et al.* (2021), and Santarpia *et al.* (2022) are summarized in Fig. 18(f). The sampling of Santarpia *et al.* (2022), Liu *et al.* (2020), Chia *et al.* (2020), and Stern *et al.* (2021) did not target specific respiratory activities but rather was conducted inside hospital rooms with COVID-19 patients. Presumably the sampling probed a mixture of breathing, coughing (a common symptom of COVID-19), and probably also speaking. Chia *et al.* (2020) specified that the sampled patients were coughing. Lednicky *et al.* (2021) collected aerosol samples inside a car driven by a COVID-19 patient with a mild clinical course of the disease, and thus an unknown mixture of respiratory activities was probed. A summary of the studies shows that viral RNA was observed over a wide size range of ∼10 nm to ∼20 μm. The size distributions appear to have a bimodal character, likely involving mode B2 as well as a mixture of modes LT and O1. We have refrained from describing the distributions in Fig. 18(f) with individual modes in detail since the available data are sparse and the variability is high.

Beyond aerosol emission and transport from host to host, the size-dependent deposition of pathogen-laden particles throughout the human respiratory tract is of critical importance. Figure 18(g) shows the established ICPR deposition model, thereby distinguishing depositions in the alveolar, tracheobronchiolar, and head airways, which is driven by the size-dependent influences of diffusion, impaction, and sedimentation particle losses. Here a detailed understanding of the modality of the inhaled PSD [Figs. 18(b) and 18(c)] in combination with knowledge on the modes that presumably carry most of a given pathogen [Fig. 18(d)–18(f)] allows one to assess to what extent the pathogens reach their corresponding target sites in the respiratory tract. For example, alveolar macrophages are the target site for airborne infection with *M. tuberculosis* (Roy and Milton, 2004; Lin and Flynn, 2010). A combination of Figs. 18(d) and 18(g) shows that the carrier mode LT is colocated with a secondary maximum of alveolar deposition, underlining that the bacteria could reach the target directly in the airborne state. Note further that the modes O1 and O2, for which Fig. 18(d) suggests that the bacteria are only sparsely present, corresponds to a size range in which the alveolar deposition approaches zero. In this sense, the mode LT appears to be the "evolutionarily optimized" vehicle for the airborne spread of TB directly to its target sites.

Finally, Fig. 18(h) completes the picture by illustrating the characteristic size-dependent filtration efficiencies of selected face mask materials. Wearing face masks is a main measure to decelerate the spread of diseases given that (semi)ballistic droplet spray and aerosol transmission are major infection routes. Accordingly, the literature on the influence of face masks (especially in the context of the COVID-19 pandemic) has grown considerably (Lindsley *et al.*, 2010a, 2010b, 2021; Asadi *et al.*, 2020; Mitze *et al.*, 2020; Cheng *et al.*, 2021; Clapp *et al.*, 2021; Drewnick *et al.*, 2021; Gandhi and Marr, 2021; Leith, L'Orange, and Volckens, 2021; Li, Niu, and Zhu, 2021; Pan *et al.*, 2021; Rogak *et al.*, 2021; Bagheri *et al.*, 2023). Figure 18(h) shows an exemplary study with measured filtration efficiencies of mask materials. The similarity between the size-dependent deposition in the respiratory tract and the face mask filtration efficiency is obvious and can be explained by the fact that the relevant particle loss mechanisms (i.e., diffusional, impaction, and sedimentation losses) are comparatively ineffective in the range roughly between 100 and 500 nm. In the field of atmospheric aerosol physics, this size band is known as the location of the so-called accumulation mode because particles tend to accumulate there

due to the minimum in particle loss or removal efficiencies (Cheng, 1997; Lai, 2002; He, Morawska, and Gilbert, 2005; Seinfeld and Pandis, 2016). Scheuch (2020) emphasized that this size band is particularly important, as it is the colocation of the minimum in face mask efficiency and the maximum of the atmospheric lifetime of pathogen-laden particles. The peak of mode B2 falls within this range, which implies that it has on average the longest lifetime in the air, as well as the largest transmissibility through common face mask materials (especially so-called community masks). Face masks with high filtration efficiencies (such as N95 and FFP2 masks) show a much lower transmissibility in this size range and are thus particularly useful for preventing the airborne transmission of diseases such as COVID-19 (Lelieveld *et al.*, 2020; Cheng *et al.*, 2021; Howard *et al.*, 2021; Nordsiek, Bodenschatz, and Bagheri, 2021; Bagheri *et al.*, 2023).

Figure 19 shows the filtration effect of face mask materials on the size distribution of the speaking-related particles emission rates shown in Fig. 18(b). All PSDs, the initial speaking-related PSD and the PSDs after face mask filtration, have been multiplied by the total deposition curve of the respiratory tract in Fig. 18(h). Thus, the black PSDs in Fig. 19(b) compare the deposited particle fractions with and without face mask filtration. Note that this assumes mask filtration without leaks (i.e., a tight fit of the mask). Beyond the filtration efficiency of the mask materials, the tightness of the fit and the potential leakage between mask and face is crucial to the overall mask performance (Shaffer and Rengasamy, 2009; Bagheri *et al.*, 2023). All mask materials have a high filtration efficacy for large particles (i.e., larger than ∼5 μm). For the small particle range (i.e., smaller than ∼5 μm), however, the transmission curves of community, surgical, and FFP2 masks show significant differences. Note that these differences overlap with the size range of the modes B2 and LT, which are presumably involved in the pathogen transmission, as shown in Figs. 18(d)–18(f).

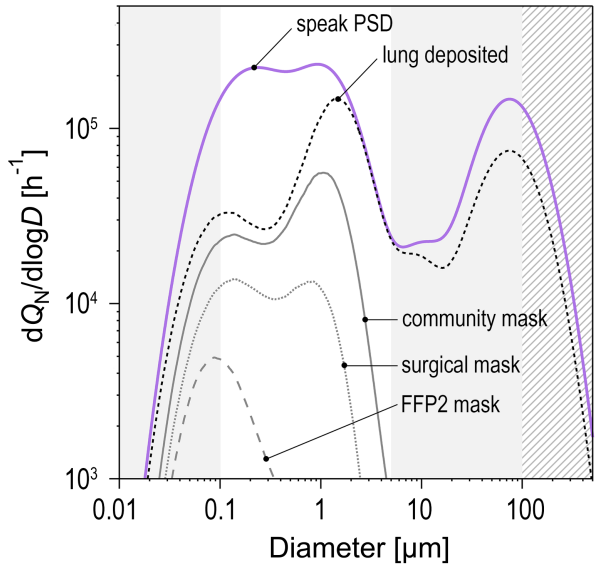

FIG. 19. Effects of particle deposition in respiratory tract and face mask filtration on speaking-related PSD [here the number emission rate Q_N adapted from Fig. 18(b)]. Compared here are (i) PSD after emission, (ii) the fraction of PSD deposited in the respiratory tract [compare this to Fig. 18(g)], and (iii) the fraction of PSD deposited in the respiratory tract after filtration through materials of community masks, surgical masks, and FFP2 masks [compare this to Fig. 18(h)]. Only the mask filtration, not the mask fitting properties (loose vs tight), is taken into account. Background shading divides the overall size range according to common definitions (up to 100 μm) and a size spanning the physical size of influenza and SARS-CoV-2 virions (∼0.1 μm) to ∼5 μm, with the fraction being particularly relevant for far-field transmission.

IV. SUMMARY AND CONCLUSIONS

A. Aerosol and droplet transmission of infectious human diseases

(1) A critical review of definitions, nomenclature, and concepts regarding airborne or contact-free disease transmission was presented. Through this process we clarified critical aspects of the discussion for efficient transdisciplinary exchange and collaboration between the medical and physical sciences (such as the use of the term airborne, the continuity and overlap of respiratory aerosol and droplet size ranges, and droplet desiccation and hygroscopicity). Moreover, we highlighted important knowledge gaps that currently hamper the quantitative assessment and prediction of the spread of pathogens. An improved connection between infectious disease medicine and a physical or mechanistic understanding of respiratory emissions thus provides a basis for the improved control of disease transmission, including nonpharmaceutical intervention strategies (such as mask type, ventilation, and filtration), especially for diseases for which no effective vaccination exists. While we endeavor to provide tools to bring groups of scientists closer together, we acknowledge disciplinary bias is implicit and have written primarily from the perspective of physical scientists.

(2) Based on a comprehensive review and synthesis of the scientific literature, we developed a parametrization of particle emissions from the full respiratory tract. The parametrization requires only five log-normal modes for the size range of > 10 nm to ∼1000 μm to efficiently describe all PSDs available in the published literature. The parametrization was optimized in the course of a "multidimensional fitting" to represent both number and volume size distributions. As a further development of Johnson *et al.* (2011), the five log-normal modes can be subdivided into three categories that elucidate unique and different particle formation mechanisms and sites in the respiratory tract. The bronchiolar modes B1 and B2 are formed in the terminal brochioles through film bursting processes. The mode LT is presumably formed through vibrations and shear forces in the larynx and/or high turbulence and shear forces in the trachea. The modes O1 and O2 are formed by mouth, tongue, and lip movements.

(3) Breathing is associated with a bimodal (B1 and B2), maybe trimodal (B1, B2, and LT) PSD, whereas speaking and singing as well as coughing are associated with pentamodal PSDs (B1, B2, LT, O1, and O2). It has been documented that the modes O1 and O2 are indeed absent during breathing and not a matter of limitations in the measured size range. Overall, the PSDs of all respiratory activities yield a consistent pattern. Respiratory activities show a characteristic, multimodal PSD shape, while the associated particle concentrations and emission rates vary across orders of magnitude.

(4) The variability among PSDs within a given respiratory activity can be explained by (i) the fact that the particles were measured under different RH conditions and thus different particle drying states after exhalation as well as by (ii) differences in mode height relative to one other regarding breathing patterns and vocalization volumes.

(5) The emission of pathogen-laden particles in the course of all respiratory activities can transmit diseases in the near and far field. For near-field aerosol transmission, the particle concentration in the exhaled puffs is of primary relevance. Here our parametrization is consistent with previous determinations that show the following order for number concentrations C_N, $C_N(\text{coughing}) > C_N(\text{speaking}) \approx C_N(\text{breathing})$, and for volume concentrations C_V, $C_V(\text{coughing}) \approx C_V(\text{speaking}) > C_V(\text{breathing})$ (Asadi *et al.*, 2019; Archer *et al.*, 2022; Hamilton *et al.*, 2022; Bagheri *et al.*, 2023). For far-field aerosol transmission, the particle emission rate, which strongly depends on the frequency of a given respiratory activity, is of primary relevance. Here our parametrization shows the following order for the number emission rates Q_N, $Q_N(\text{speaking}) > Q_N(\text{coughing}) > Q_N(\text{breathing})$, and for the volume emission rates Q_V, $Q_V(\text{speaking}) > Q_V(\text{coughing}) > Q_V(\text{breathing})$.

(6) An understanding of the multimodal shape of the respiration PSDs provides mechanistic insight into airborne disease transmission and the efficacy of preventative measures. For common aerosol-transmissible diseases, modes were identified through which the pathogens might be transmitted, for instance, cough-related mode LT for tuberculosis; breathing-, speaking- or singing-, and cough-related modes B2, LT, and O1 for influenza and SARS-CoV-2. Future studies will help to constrain this relationship.

(7) Public health recommendations can benefit from an improved understanding of the respiration PSDs parametrized here and through an updated view of the mechanisms of particle mixing and transmission illustrated in Fig. 20. Larger droplets (> 100 μm) are not generally inhalable, have rapid settling velocity, and are thus relevant only in the near field, where ballistic trajectories can launch them onto nearby surfaces or directly onto mucosal membranes of the recipient. For respiratory particles in this size regime, even relatively loose fitting masks (i.e., surgical style) or face shields are sufficient for protection (Cappa *et al.*, 2021). Smaller aerosols (< 100 μm) can be inhaled, have a lower settling velocity, and therefore can remain suspended for many minutes to hours. Thus, they are relevant in both the near and far fields. In the near field, aerosols are concentrated in the breathing zone of the emitting person but rapidly mix into the full room volume. In both the near and far fields, improved masks (i.e., FFP2 or N95 respirators) are most appropriate to guard against aerosol inhalation (Bischoff *et al.*, 2013; Cheng *et al.*, 2021; Goldberg *et al.*, 2021; Bagheri *et al.*, 2023), and physical barriers are not particularly effective. In the far field, aerosols that build up in poorly ventilated rooms [see Lai (2002), He, Morawska, and Gilbert (2005), Helleis, Klimach, and Pöschl (2021), and references therein] can also be removed via ventilation and filtration, but these added controls provide little benefit in the near field. Appropriate control measures and nonpharmaceutical intervention tools, such as use of high-quality face masks, physical distancing, ventilation, and room filtration, should thus be matched to the type of space involved and the sizes and properties of the respiratory particles relevant for a given respiratory disease. Other engineering controls such as upper-room germicidal UV light can also be deployed as part of a layered strategy for virus inactivation, with a primary application against far-field aerosols (Miller, Linnes, and Luongo, 2013). Note also that far-field aerosol transmission is an almost exclusively indoor challenge because dilution as a function of increasing distance from the emitter becomes so large outdoors that infection risk is dramatically lower (although not zero, depending on wind patterns and other variables) (Bulfone *et al.*, 2021; Maggiore, Tommasini, and Ossi, 2021). The near-field aerosol transmission, however, is relevant in both indoor and outdoor settings.

B. Aerosol and droplet transmission of COVID-19 via the SARS-CoV-2 virus

(1) No definitive proof exists that SARS-CoV-2 (or almost any other individual viral pathogen) is transmitted through a specific transmission mechanism (Leung, 2021). That said, considerable evidence suggests that the transmission of SARS-CoV-2 proceeds primarily through aerosol particles in the size range of ∼0.1 to ∼10 μm, possibly dominated by near-field exposure but with an important contribution from far-field mixing in the room (Allen and Marr, 2020; Chen *et al.*, 2020; Klompas, Baker, and Rhee, 2020; Kwon *et al.*, 2020; Lednicky *et al.*, 2020, 2021; Lee *et al.*, 2020; Lu *et al.*, 2020; Prather, Wang, and Schooley, 2020; Tang *et al.*, 2020, 2021; Azimi *et al.*, 2021; Hwang *et al.*, 2021; Kutter *et al.*, 2021; Miller *et al.*, 2021). The parametrization here suggests that the source of these particles is the PSD modes B2, LT, and/or O1, originating from multiple respiratory activities, including breathing, speaking or singing, and coughing. Fecal material aerosolized in broadly

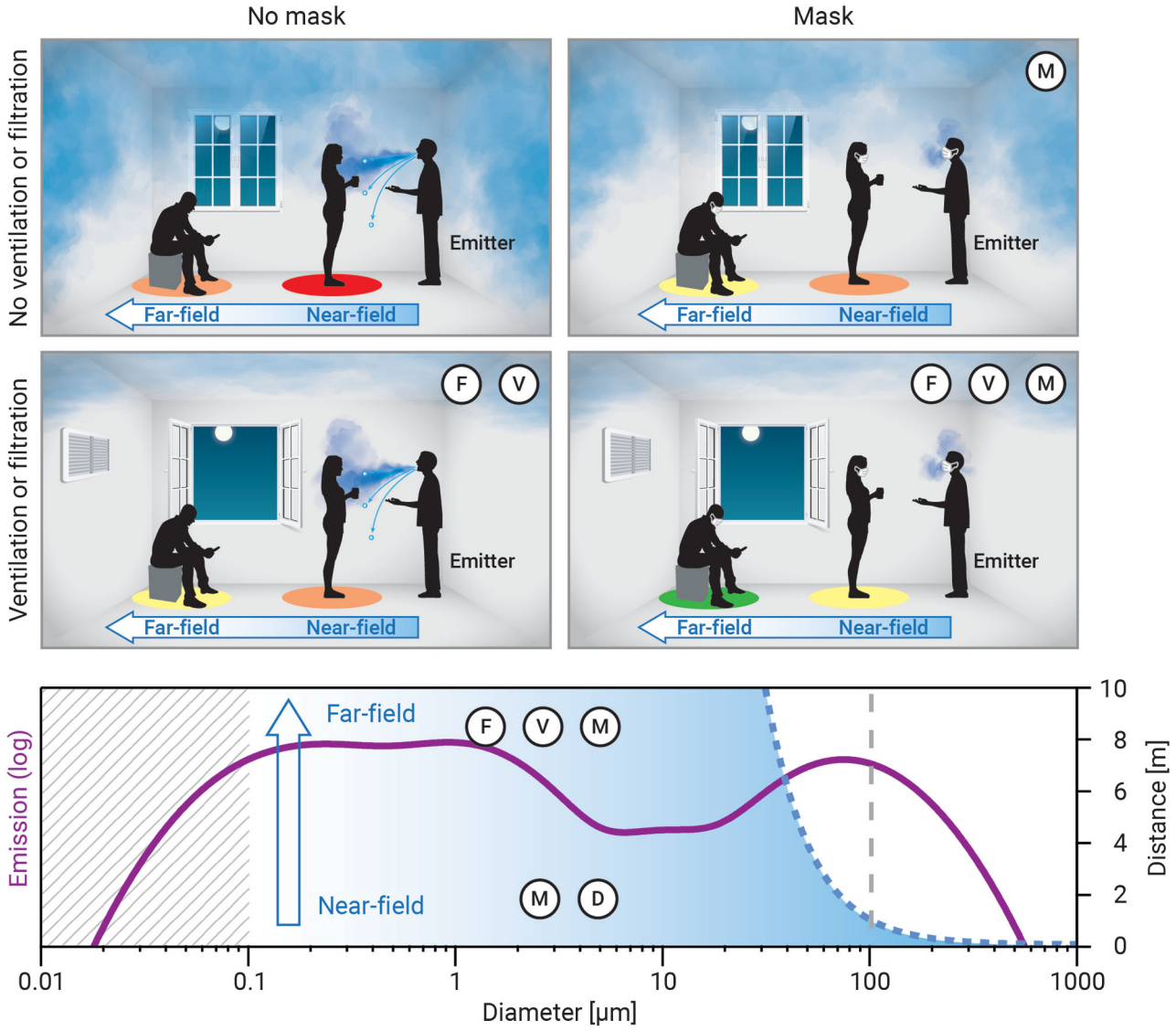

FIG. 20. Top panels: illustrations of near- and far-field aerosol transmission in relation to the respiratory PSD and the following preventative measures: M, masking; D, distance; F, filtration; and V, ventilation. Only the aerosol emission from the infected emitter is visualized. The approximated infection risks for the recipients are illustrated with colored circles (red = highest risk > orange > yellow > green = lowest risk). Bottom panel: speaking-related PSD [adapted from Fig. 19(b)] that represents the particle concentration (most relevant in the near field) and emission rate (most relevant in the far field) that can be converted into one another with a constant factor; see Table I. The blue dashed line shows that the travel range of exhaled particles (for an exemplary emission velocity of 20 $m\,s^{-1}$ and an emission height of 1.5 m) in still air is strongly size dependent (D^2 relationship): large particles (i.e., > 100 μm) are exclusively relevant in the near field, whereas smaller particles (i.e., < 100 μm) are relevant in both the near and far fields. The blue background shading in the lower panel qualitatively illustrates the fact that particle concentrations decrease with distance from the emitter due to dilution and mixing. The threshold at 100 nm marks the physical size of the SARS-CoV-2 and influenza virions.

similar size ranges ($\lesssim$10 μm) have also been suggested to be important for disease spread in some cases (Kang *et al.*, 2020; Gormley, Aspray, and Kelly, 2021) but was not discussed in detail in the review.

(2) The relevance of SARS-CoV-2–carrying aerosol particles in the size range of ~0.1 to ~10 μm combined with the variable filtration efficiency and poor average fit quality of so-called community face masks in this size range imply that tight-fitting, high efficiency masks such as N95 and FFP2 ones are particularly important for mitigating the airborne transmission of COVID-19 (Cheng *et al.*, 2021; Drewnick *et al.*, 2021; Bagheri *et al.*, 2023). The small size of these particles also supports the suggestion that increased ventilation and room filtration will provide a community health benefit against COVID-19 (Nissen *et al.*, 2020; Curtius, Granzin, and Schrod, 2021; Helleis, Klimach, and Pöschl, 2021; Mathai *et al.*, 2021; Rothamer *et al.*, 2021).

(3) With regard to studies suggesting that the upper respiratory tract (i.e., the nose) is the initial target site for SARS-CoV-2 (Hou *et al.*, 2020; Wolfel *et al.*,

2020), the particle modes LT and O1 may be particularly important because they overlap with the size range of the highest deposition probability in the upper airways.

(4) Speaking, often with other persons in close proximity, is a frequent activity of everyday life and is also associated with high particle emission rates. Therefore, speaking can play a particularly important role in both near- and far-field transmission of COVID-19. A summary of the aerosol emission rates and particle sizes, as shown, supports the idea that speaking is likely a stronger driver of the pandemic than generally considered early in the development of the COVID-19 pandemic.

(5) Similar bimodal distributions observed for influenza and SARS-CoV-2 in the size range of the modes B2, LT, and/or O1 might indicate analogies in the airborne transmission routes of those two pathogens. This is a critical piece in context of available preventative measures against each because it shows that observations about mask wearing and ventilation can be leveraged for substantial public health benefit against seasonal influenza as well as other emerging respiratory diseases.

(6) Together these findings (such as those in Fig. 20) should be implemented in updated and sophisticated hygiene concepts, allowing common work and life in times of pandemic.

C. Open questions and research perspectives

(1) Experimental data on respiratory PSDs should be extended to reduce uncertainties with respect to our process understanding and in relation to major respiratory diseases. Data coverage of the smallest mode B1 (centered at ∼70 nm) and the largest modes O1 and O2 (centered at ∼10 μm and ∼100 μm) is especially sparse. Further, most available measurements have focused on a limited portion of the full range of respiratory particle sizes (< 10 nm to > 1000 μm). We propose that systematic experiments across the full size spectrum should be conducted for different respiratory activities and a large cohort of volunteers (including healthy and individual disease groups) to consolidate our knowledge on the overall modality, the mode ratios, and their variability as a function of respiratory activities. A number of instruments will be required to span the full range of particle sizes (Johnson *et al.*, 2011; Bagheri *et al.*, 2023). Within the design of these experiments, care should be taken so that instrument PSDs overlap for cross validation. Instruments with high size resolution are preferred to resolve details of the PSDs, which ideally can be acquired at high time resolution to also observe differences in PSD properties as a function of rapidly changing emission mechanisms.

(2) Existing measurements have been conducted under widely differing experimental conditions, which hampers comparisons across studies and individuals. Standardized operational procedures for the analysis of respiratory aerosols would therefore be desirable, as outlined for atmospheric aerosols by Wiedensohler *et al.* (2014). One effort in this area was recently conducted as part of journal special issues focused on standardizing bioaerosol measurements; however, this was only a first step, and significant follow-up will be required (Alsved, Bourouiba *et al.*, 2020; Cox *et al.*, 2020; Huffman *et al.*, 2020; Huffman and Ratnesar-Shumate, 2020; Mainelis, 2020; Santarpia, Ratnesar-Shumate, and Haddrell, 2020; Santl-Temkiv *et al.*, 2020). Important aspects of such a standardization might be as follows.

   (i) Defined drying conditions, for instance, $< 40\%$ RH, which is a rather reproducible state.
   (ii) Isokinetic and isoaxial aerosol sampling, especially for large particles.
   (iii) Corrections for particle losses in the experimental setup (von der Weiden, Drewnick, and Borrmann, 2009).
   (iv) Documentation of the precise sampling conditions (i.e., RH and temperature).
   (v) A documentation of basic physiological, spirometric, and demographic parameters.

(3) Recorded measurements of respiratory activities have thus far been mostly standardized maneuvers and therefore reflect "normal live" emissions only imperfectly. Therefore, continuous measurements of respiratory emission from volunteers during different everyday activities (such as conversation, office work, school attendance, and gym workouts) would be useful for better assessing infection risks under real-world conditions. Note, however, that the ambient aerosol background might mask the respiration aerosols and thus must be avoided, for instance, using suitable sampling masks (Bagheri *et al.*, 2023) or other strategies.

(4) Edwards *et al.* (2021) showed significant differences in SARS-CoV-2 aerosol emission rates as a function of age and several physiological factors, but otherwise data are still relatively sparse regarding the physical basis for explaining why some individuals act as viral aerosol superspreaders. For example, it is still relatively uncertain to what extent the superspreading of many diseases by certain individuals correlates with particularly high emission rates of exhaled particles overall and why this might be the case. Dedicated studies on the high intersubject variability of emission rates would be important for closing gaps in this area of knowledge.

(5) Data on the chemical composition of saliva and ELF and its variability are still limited. While many studies on saliva composition exist, for instance, concentrations of a variety of species are either uncertain or even completely lacking. Further experiments are needed here, as the chemical microenvironment plays a primary role in the decay of viability of embedded pathogens during airborne transport.

(6) Data on the hygroscopic properties of mucosalivary particles and their shrinkage or growth under changing RH conditions, including the influence of potential

hysteresis effects upon efflorescence and deliquescence, are sparse. Instruments reaching high RH, such as a HHTDMA (Mikhailov and Vlasenko, 2020; Mikhailov *et al.*, 2021) or a similar device, may allow for investigation of these parameters.

(7) Precise pathogen emission mechanisms and sites are still largely uncertain. In this sense, our assignment of certain modes and likely emission mechanisms and sites (i.e., B1, B2, LT, O1, and O2) can be considered preliminary estimates. While the processes behind the mode B2 are well documented, the origin of the mode B1 is widely unknown. Additionally, the interplay of emission from the larynx and trachea, which we combined here in the mode LT, present large uncertainties. Finally, the precise mechanisms and sites of droplet formation in the mouth that generate the modes O1 and O2 are poorly understood.

(8) Further experimental studies on the size distributions of pathogen-laden particles are greatly needed as they (i) provide suggestions on droplet formation mechanisms and sites in the respiratory tract, (ii) allow for the assessment of which PSD modes are most relevant as drivers of pathogen spread, and (iii) help to identify the most likely deposition sites in the respiratory tract in relation to data on pathogen tropism (Nomaguchi *et al.*, 2012; Hou *et al.*, 2020).

(9) A better understanding of respiratory particle transport and dilution in air as a function of particle size will be required to help model the relative risk of infection in both indoor and outdoor settings. Without the ability to detect a small fraction of respiratory particles, it is impossible to use particle sizing instruments alone to observe respiratory emissions in a room. Thus, improved instrumental techniques will be required to selectively analyze respiratory particles amid the overwhelming pool of existing aerosols in any room or outdoor air volume. Further, an improved understanding will be required on the quantitative range of how many pathogen entities (for instance, virions) for each disease are necessary for infection via the inhalation of the aerosol phase or deposition of the droplet phase (Wells, 1955; Rudnick and Milton, 2003; Jones and Brosseau, 2015).

(10) An improved understanding of the environmental viability of pathogens as a function of aerosol size and composition, RH, temperature, and UV flux will aid the estimation of infectivity as a function of real-world parameters (Fears *et al.*, 2020; Santarpia *et al.*, 2020; van Doremalen *et al.*, 2020).

LIST OF SYMBOLS AND ABBREVIATIONS

A_i (cm^{-3})	parameter in log-normal fit function, number concentration at D_i
a_w	water activity in the aqueous solution
APS	aerodynamic particle sizer
ASL	airways surface layer
b	empirical factor representing the relationship between C_N and V_B/V_{VC}
BFFB	bronchiole fluid film burst
BSA	bovine serum albumin
B1	bronchiol mode 1
B2	bronchiol mode 2
C_c	Cunningham slip correction
C_D	drag coefficient
c_g ($mol\,cm^{-3}$)	molar concentration of water vapor in the gas phase
c_{gs} ($mol\,cm^{-3}$)	molar concentration of water vapor in the near-surface gas phase
C_H (cm^{-3})	mode number concentration in the Heintzenberg formula
C_N (cm^{-3})	number concentration
C_T (cm^{-3})	number concentration during tidal breathing
C_v ($\mu m^3\,cm^{-3}$)	volume concentration
C	breathing with airway closure
CFU	culture forming unit
COVID-19	coronavirus disease 2019
CP	airway closing point
D (μm)	diameter [the unit in Eqs. (1)–(3) is m]
D_{dry} (μm)	dry diameter
D_{eq} (μm)	equilibrium diameter after shrinking in dry atmosphere
D_{exh} (μm)	initial diameter after exhalation
D_g ($cm^2\,s^{-1}$)	gas diffusion coefficient of water vapor
D_i (μm)	mode mean geometric diameter
D_{wet} (μm)	wet diameter for a supersaturation

$dC_N/d\log D$ (cm^{-3})	bin-normalized number concentration
$dC_V/d\log D$ ($\mu m^3\,cm^{-3}$)	bin-normalized volume concentration
$dQ_N/d\log D$ (h^{-1})	bin-normalized number emission rate
$dQ_V/d\log D$ ($\mu m^3\,h^{-1}$)	bin-normalized volume emission rate
DDA	droplet deposition analysis
DRH	deliquescence relative humidity
ELF	epithelial lining fluid
ERH	efflorescence relative humidity
ERV	expiration reserve volume
EXH	exhalation
f (h^{-1})	frequency of respiratory activity
FFP2	filtering facepiece respirator filtering $\leq 94\%$ of airborne particles
FRC	functional residual capacity
g ($m\,s^{-2}$)	gravitational acceleration
g_d	diameter equivalent hygroscopic growth factor
g_m	mass equivalent hygroscopic growth factor
HHTDMA	high-humidity tandem differential mobility analyzer
i_s	van 't Hoff factor of the solute
ICPR	International Commission on Radiological Protection
IRV	inspiration reserve volume
INH	inhalation
LLPS	liquid-liquid phase separation
LRT	lower respiratory tract
LT	larynx and trachea mode
M ($kg\,mol^{-1}$)	molar weight (indices w = water, s = dry solute)
MERS-CoV	Middle East respiratory syndrome coronavirus
MeV	Measles morbillivirus
n	number of moles
NIOSH	National Institute for Occupational Safety and Health
NSD	number size distribution
N95	filtering facepiece respirator filtering $\leq 95\%$ of airborne particles
O1	oral mode 1
O2	oral mode 2
OPC	optical particle counter
OPS	optical particle sizer
PSD	particle size distribution
q (cm^{-3})	volume exhaled by respiratory activity
Q_N (h^{-1})	number emission rate
Q_V ($\mu m^3\,h^{-1}$)	volume emission rate
R ($kg\,m^2\,s^{-2}\,mol^{-1}\,K^{-1}$)	universal gas constant
R^2	coefficient of determination
R_0	basic reproduction rate for infectious diseases
Re	Reynolds number
RH (%)	relative humidity
RNA	ribonucleic acid
RTLF	respiratory tract lining fluid
RV	residual volume
s	water vapor saturation
S (%)	water vapor supersaturation
SARS-CoV	severe acute respiratory syndrome coronavirus
SARS-CoV-2	severe acute respiratory syndrome coronavirus 2
SSA	sea spray aerosol
SMPS	scanning mobility particle sizer

t_e (s)	evaporation time
t_s (s)	sedimentation time
T (K)	absolute temperature
T	tidal breathing
TB	Tuberculosis
TLC	total lung capacity
URT	upper respiratory tract
UV APS	ultraviolet aerodynamic particle sizer
UVB	ultraviolet B radiation
v_s ($m\,s^{-1}$)	relative velocity between air and particle
V (cm^3)	volume
$\dot{V}$ ($cm^3\,h^{-1}$)	time-averaged air emission rate (in Table I, the unit is Lh^{-1})
V_B (cm^3)	breathed volume
V_s (cm^3)	volume of the dry solute
V_T (cm^3)	tidal volume
V_{VC} (cm^3)	vital capacity
V_w (cm^3)	volume of pure water within the droplet
VC	vital capacity
VSD	volume size distribution
VZV	varicella-zoster virus
ZSR	Zdanovskii-Stokes-Robinson
Δt (s)	duration of respiratory activities or events
λ (μm)	gas mean free path
κ	hygroscopicity parameter
ρ ($kg\,m^{-3}$)	density (indices g, gas; p, particle; s, solute; w, water)
η ($kg\,m^{-1}\,s^{-1}$)	gas dynamic viscosity
θ (°C)	temperature
σ_i	modal geometric standard deviation for a log-normal fit
σ_H	modal geometric standard deviation in the Heintzenberg formulation
σ_s ($kg\,s^{-2}$)	solution surface tension
ν_s	stoichiometric dissociation number
Φ_s	molar osmotic coefficient in aqueous solution

ACKNOWLEDGMENTS

We thank Benjamin Bandowe, Kevin Cahill, James Davies, Bruna Holanda, Prasad Kasibhatla, Thomas Klimach, Uwe Kuhn, Luiz Machado, Oliver Schlenczek, John Volckens, and Cornelius Zetzsch for the support and the inspiring discussions. We appreciate the helpful support of Andreas Zimmer in the literature research and the creative support of Dom Jack in figure layout. M. L. P. and C. P. are particularly grateful for the support by Gerhard Heun, Rita Heun, and Gabriele Krüger during the writing of this manuscript. This work has been supported by the Max Planck Society (MPG). G. B., E. B., and S. S. acknowledge support from the German Federal Ministry of Education and Research (BMBF) as part of Bundesweites Forschungsnetz Angewandte Surveillance und Teststrategie (B-FAST) Project No. 01KX2021 within the Netzwerk Universitätsmedizin (NUM) and the MPG. The funders had no role in study design, data collection and analysis, decision to publish, or preparation of the manuscript. J. A. H. thanks the University of Denver for intramural funding for faculty support. The work on the section on hygroscopic properties of the respiratory particles was supported by the Russian Science Foundation (Grant Agreement No. 22-27-00258).

REFERENCES

Abkarian, M., S. Mendez, N. Xue, F. Yang, and H. A. Stone, 2020, Proc. Natl. Acad. Sci. U.S.A. **117**, 25237.

Abkarian, M., and H. A. Stone, 2020, Phys. Rev. Fluids **5**, 102301.

Ai, Z. T., and A. K. Melikov, 2018, Indoor Air **28**, 500.

Alford, R. H., J. A. Kasel, P. J. Gerone, and V. Knight, 1966, Proc. Soc. Exp. Biol. Med. **122**, 800.

Allen, J. G., and L. C. Marr, 2020, Indoor Air **30**, 557.

Almstrand, A.-C., B. Bake, E. Ljungström, P. Larsson, A. Bredberg, E. Mirgorodskaya, and A.-C. Olin, 2010, J. Appl. Physiol. **108**, 584.

Almstrand, A.-C., E. Ljungström, J. Lausmaa, B. Bake, P. Sjövall, and A.-C. Olin, 2009, Anal. Chem. **81**, 662.

Alonso, C., P. C. Raynor, P. R. Davies, and M. Torremorell, 2015, PLoS One **10**, e0135675.

Alonso, C., P. C. Raynor, S. Goyal, B. A. Olson, A. Alba, P. R. Davies, and M. Torremorell, 2017, J. Vet. Diagn. Invest. **29**, 298.

Alsved, M., L. Bourouiba, C. Duchaine, J. Löndahl, L. C. Marr, S. T. Parker, A. J. Prussin, and R. J. Thomas, 2020, Aerosol Sci. Technol. **54**, 547.

Alsved, M., A. Matamis, R. Bohlin, M. Richter, P. E. Bengtsson, C. J. Fraenkel, P. Medstrand, and J. Löndahl, 2020, Aerosol Sci. Technol. **54**, 1245.

Anand, S., and Y. S. Mayya, 2020, Sci. Rep. **10**, 21174.

Andreae, M. O., 2009, Atmos. Chem. Phys. **9**, 543.

Andreae, M. O., and D. Rosenfeld, 2008, Earth-Sci. Rev. **89**, 13.

Anwarul Hasan, M. D., C. F. Lange, and M. L. King, 2010, J. Non-Newtonian Fluid Mech. **165**, 1431.

Appert, J., P. C. Raynor, M. Abin, Y. Chander, H. Guarino, S. M. Goyal, Z. Zuo, S. Ge, and T. H. Kuehn, 2012, Aerosol Sci. Technol. **46**, 249.

Archer, J., *et al.*, 2022, Interface Focus **12**, 20210078.

Armendariz, A. J., and D. Leith, 2002, J. Aerosol Sci. **33**, 133.

Artaxo, P., *et al.*, 2022, Tellus B **74**, 24.

Arundel, A. V., E. M. Sterling, J. H. Biggin, and T. D. Sterling, 1986, Environ. Health Perspect. **65**, 351.

Asadi, S., C. D. Cappa, S. Barreda, A. S. Wexler, N. M. Bouvier, and W. D. Ristenpart, 2020, Sci. Rep. **10**, 15665.

Asadi, S., A. S. Wexler, C. D. Cappa, S. Barreda, N. M. Bouvier, and W. D. Ristenpart, 2019, Sci. Rep. **9**, 2348.

Azimi, P., Z. Keshavarz, J. G. Cedeno Laurent, B. Stephens, and J. G. Allen, 2021, Proc. Natl. Acad. Sci. U.S.A. **118**, e2015482118.

Bagheri, G., and C. Bonadonna, 2016, Powder Technol. **301**, 526.

Bagheri, G., B. Thiede, B. Hejazi, O. Schlenczek, and E. Bodenschatz, 2021, Proc. Natl. Acad. Sci. U.S.A. **118**, e2110117118.

Bagheri, G., *et al.*, 2023, J. Aerosol Sci. **168**, 106102.

Bake, B., P. Larsson, G. Ljungkvist, E. Ljungström, and A. C. Olin, 2019, Respir. Res. **20**, 8.

Bake, B., E. Ljungstrom, A. Claesson, H. K. Carlsen, M. Holm, and A. C. Olin, 2017, J. Aerosol Med. Pulm. Drug Delivery **30**, 267.

Bansil, R., and B. S. Turner, 2006, Curr. Opin. Colloid Interface Sci. **11**, 164.

Bazant, M. Z., and J. W. M. Bush, 2021, Proc. Natl. Acad. Sci. U.S.A. **118**, e2018995118.

Bekking, C., L. Yip, N. Groulx, N. Doggett, M. Finn, and S. Mubareka, 2019, Influenza Other Respir. Viruses **13**, 564.

Ben-Aryeh, H., M. Fisher, R. Szargel, and D. Laufer, 1990, Arch. Oral Biol. **35**, 929.

Ben-Aryeh, H., A. Shalev, R. Szargel, A. Laor, D. Laufer, and D. Gutman, 1986, Biochem. Med. Metab. Biol. **36**, 260.

Berkemeier, T., S. S. Steimer, U. K. Krieger, T. Peter, U. Poeschl, M. Ammann, and M. Shiraiwa, 2016, Phys. Chem. Chem. Phys. **18**, 12662.

Bertram, A. K., S. T. Martin, S. J. Hanna, M. L. Smith, A. Bodsworth, Q. Chen, M. Kuwata, A. Liu, Y. You, and S. R. Zorn, 2011, Atmos. Chem. Phys. **11**, 10995.

Bicer, E. M., 2014, Ph.D. thesis (King's College London).

Birnir, B., and L. Angheluta, 2020, 10.1101/2020.08.11.20173195.

Bischoff, W. E., K. Swett, I. Leng, and T. R. Peters, 2013, J. Infect. Dis. **207**, 1037.

Bloch, A. B., W. A. Orenstein, W. M. Ewing, W. H. Spain, G. F. Mallison, K. L. Herrmann, and A. R. Hinman, 1985, Pediatrics **75**, 676.

Bloom, B. R., and C. J. L. Murray, 1992, Science **257**, 1055.

Boone, S. A., and C. P. Gerba, 2007, Appl. Environ. Microbiol. **73**, 1687.

Booth, T. F., *et al.*, 2005, J. Infect. Dis. **191**, 1472.

Bourouiba, L., 2020, JAMA, J. Am. Med. Assoc. **323**, 1837.

Bourouiba, L., 2021, Annu. Rev. Fluid Mech. **53**, 473.

Bourouiba, L., E. Dehandschoewercker, and J. W. M. Bush, 2014, J. Fluid Mech. **745**, 537.

Brandtzaeg, P., 1998, in *Glandular Mechanisms of Salivary Secretion*, Vol. 10, edited by J. Garrett, J. Ekström, and L. Anderson (Karger, Basel, Switzerland), pp. 167–199.

Bredberg, A., J. Gobom, A.-C. Almstrand, P. Larsson, K. Blennow, A.-C. Olin, and E. Mirgorodskaya, 2012, Clin. Chem. (Washington, DC) **58**, 431.

Brown, J., F. K. A. Gregson, A. Shrimpton, T. M. Cook, B. R. Bzdek, J. P. Reid, and A. E. Pickering, 2021, Anaesthesia **76**, 174.

Brubaker, A. P., 1919, JAMA, J. Am. Med. Assoc. **73**, 585.

Bulfone, T. C., M. Malekinejad, G. W. Rutherford, and N. Razani, 2021, J. Infect. Dis. **223**, 550.

Cao, G., J. D. Noti, F. M. Blachere, W. G. Lindsley, and D. H. Beezhold, 2011, J. Environ. Monit. **13**, 3321.

Cappa, C., S. Asadi, S. Barreda, A. Wexler, N. Bouvier, and W. Ristenpart, 2021, Sci. Rep. **11**, 12110.

Chao, C. Y. H., *et al.*, 2009, J. Aerosol Sci. **40**, 122.

Chaudhuri, S., S. Basu, P. Kabi, V. R. Unni, and A. Saha, 2020, Phys. Fluids **32**, 063309.

Chaudhuri, S., S. Basu, and A. Saha, 2020, Phys. Fluids **32**, 123306.

Cheaib, Z., and A. Lussi, 2013, J. Biosci. **38**, 259.

Chen, W., N. Zhang, J. Wei, H.-L. Yen, and Y. Li, 2020, Build. Environ. **176**, 106859.

Cheng, Y., N. Ma, C. Witt, S. Rapp, P. S. Wild, M. O. Andreae, U. Pöschl, and H. Su, 2021, Science **372**, 1439.

Cheng, Y. S., 1997, Aerosol Sci. Technol. **27**, 131.

Chi, Y., K. Honda, J. Wei, H. Feng, and J. Dang, 2015, in *Proceedings of the 16th Annual Conference of the International Speech Communication Association (Interspeech 2015), Dresden, Germany, 2015*, 10.21437/Interspeech.2015-488.

Chia, P. Y., *et al.*, 2020, Nat. Commun. **11**, 2800.

Chong, K. L., C. S. Ng, N. Hori, R. Yang, R. Verzicco, and D. Lohse, 2021, Phys. Rev. Lett. **126**, 034502.

Clapp, P. W., E. E. Sickbert-Bennett, J. M. Samet, J. Berntsen, K. L. Zeman, D. J. Anderson, D. J. Weber, and W. D. Bennett, 2021, JAMA Intern. Med. **181**, 463.

Clegg, S. L., P. Brimblecombe, and A. S. Wexler, 1998, J. Phys. Chem. A **102**, 2155.

Conrad, B., and P. Schönle, 1979, Arch. Psychiatr. Nervenkrankh. **226**, 251.

Cowling, B. J., *et al.*, 2013, Nat. Commun. **4**, 1935.

Cox, J., H. Mbareche, W. G. Lindsley, and C. Duchaine, 2020, Aerosol Sci. Technol. **54**, 572.

Cross, C. E., A. Vandervliet, C. A. Oneill, S. Louie, and B. Halliwell, 1994, Environ. Health Perspect. **102**, 185.

Cummins, C. P., O. J. Ajayi, F. V. Mehendale, R. Gabl, and I. M. Viola, 2020, Phys. Fluids **32**, 083302.

Curtius, J., M. Granzin, and J. Schrod, 2021, Aerosol Sci. Technol. **55**, 586.

Cyranoski, D., 2020, Nature (London) **581**, 22.

Dabisch, P., *et al.*, 2021, Aerosol Sci. Technol. **55**, 142.

Dargaville, P. A., M. South, and P. N. McDougall, 1999, Am. J. Respir. Crit. Care Med. **160**, 771.

Dauletbaev, N., 2001, Thorax **56**, 13.

Davies, C., 1945, Proc. Phys. Soc. **57**, 259.

Davies, J. F., C. L. Price, J. Choczynski, and R. K. Kohli, 2021, Chem. Commun. (Cambridge) **57**, 3243.

Dawes, C., 1969, Arch. Oral Biol. **14**, 277.

Dawes, C., 1974, Arch. Oral Biol. **19**, 887.

Dawes, C., and C. Dong, 1995, Arch. Oral Biol. **40**, 699.

Day, W. C., and R. F. Berendt, 1972, Infect. Immun. **5**, 77.

de Rivas, A., and E. Villermaux, 2016, Phys. Rev. Fluids **1**, 014201.

de Rooij, M. M. T., F. Borlee, L. A. M. Smit, A. de Bruin, I. Janse, D. J. J. Heederik, and I. M. Wouters, 2016, PLoS One **11**, e0151281.
Dhand, R., and J. Li, 2020, Am. J. Respir. Crit. Care Med. **202**, 651.
Dollfuss, R. E., J. Milic-Emili, and D. V. Bates, 1967, Respir. Physiol. **2**, 234.
Drewnick, F., J. Pikmann, F. Fachinger, L. Moormann, F. Sprang, and S. Borrmann, 2021, Aerosol Sci. Technol. **55**, 63.
Drossinos, Y., and N. I. Stilianakis, 2020, Aerosol Sci. Technol. **54**, 639.
Druett, H. A., D. W. Henderson, L. Packman, and S. Peacock, 1953, J. Hyg. **51**, 359.
Druett, H. A., D. W. Henderson, and S. Peacock, 1956, J. Hyg. **54**, 49.
Duguid, J. P., 1946, Epidemiol. Infect. **44**, 471.
Dwyer, T. M., 2004, Lung **182**, 241.
Edwards, D. A., *et al.*, 2021, Proc. Natl. Acad. Sci. U.S.A. **118**, e2021830118.
Enoki, S., R. Iino, N. Morone, K. Kaihatsu, S. Sakakihara, N. Kato, and H. Noji, 2012, PLoS One **7**, e49208.
Estillore, A. D., H. S. Morris, V. W. Or, H. D. Lee, M. R. Alves, M. A. Marciano, O. Laskina, Z. Qin, A. V. Tivanski, and V. H. Grassian, 2017, Phys. Chem. Chem. Phys. **19**, 21101.
Fabian, P., J. Brain, E. A. Houseman, J. Gern, and D. K. Milton, 2011, J. Aerosol Med. Pulm. Drug Delivery **24**, 137.
Fabian, P., J. J. McDevitt, W. H. DeHaan, R. O. P. Fung, B. J. Cowling, K. H. Chan, G. M. Leung, and D. K. Milton, 2008, PLoS One **3**, e2691.
Fajnzylber, J., *et al.*, 2020, Nat. Commun. **11**, 5493.
Fears, A. C., *et al.*, 2020, Emerging Infect. Dis. **26**, 2168.
Fennelly, K., M. Tribby, C. Wu, G. Heil, L. Radonovich, J. Loeb, and J. Lednicky, 2015, Virus Adapt. Treat. **7**, 1.
Fennelly, K. P., 2020, Lancet Respir. Med. **8**, 914.
Fennelly, K. P., A. L. Davidow, S. L. Miller, N. Connell, and J. J. Ellner, 2004, Emerging Infect. Dis. **10**, 996.
Fennelly, K. P., J. W. Martyny, K. E. Fulton, I. M. Orme, D. M. Cave, and L. B. Heifets, 2004, Am. J. Respir. Crit. Care Med. **169**, 604.
Fennelly, K. P., *et al.*, 2012, Am. J. Respir. Crit. Care Med. **186**, 450.
Ferretti, L., *et al.*, 2020, 10.1101/2020.09.04.20188516.
Fleischer, M., L. Schumann, A. Hartmann, R. S. Walker, L. Ifrim, D. von Zadow, J. Lüske, J. Seybold, M. Kriegel, and D. Mürbe, 2022, J. R. Soc. Interface **19**, 20210833.
Fontes, D., J. Reyes, K. Ahmed, and M. Kinzel, 2020, Phys. Fluids **32**, 111904.
Frohlich-Nowoisky, J., *et al.*, 2016, Atmos. Res. **182**, 346.
Gandhi, M., and L. C. Marr, 2021, Med. Phys. **2**, 29, https://www.cell.com/med/pdf/S2666-6340(20)30072-6.pdf.
Gao, C., X. Zhang, D. Wang, Z. Wang, J. Li, and Z. Li, 2018, Medicine **97**, e11904.
Gao, Y., S. B. Chen, and L. E. Yu, 2007, Atmos. Environ. **41**, 2019.
Gerone, P. J., R. B. Couch, G. V. Keefer, R. G. Douglas, E. B. Derrenbacher, and V. Knight, 1966, Bacteriol. Rev. **30**, 576.
Goldberg, L., Y. Levinsky, N. Marcus, V. Hoffer, M. Gafner, S. Hadas, S. Kraus, M. Mor, and O. Scheuerman, 2021, Open Forum Infect. Dis. **8**, ofab036.
Gong, X., H. Wex, J. Voigtländer, K. W. Fomba, K. Weinhold, M. van Pinxteren, S. Henning, T. Müller, H. Herrmann, and F. Stratmann, 2020, Atmos. Chem. Phys. **20**, 1431.
Good, N., K. M. Fedak, D. Goble, A. Keisling, C. L'Orange, E. Morton, R. Phillips, K. Tanner, and J. Volckens, 2021, Environ. Sci. Technol. Lett. **8**, 1071.
Gormley, M., T. J. Aspray, and D. A. Kelly, 2021, Indoor Air **31**, 1427.
Gralton, J., E. Tovey, M.-L. McLaws, and W. D. Rawlinson, 2011, J. Infect. **62**, 1.
Gregson, F. K. A., *et al.*, 2021, Aerosol Sci. Technol. **55**, 681.
Gregson, F. K. A., *et al.*, 2022, Aerosol Sci. Technol. **56**, 160.
Grotberg, J. B., 2001, Annu. Rev. Biomed. Eng. **3**, 421.
Groth, R., L. T. Cravigan, S. Niazi, Z. Ristovski, and G. R. Johnson, 2021, J. R. Soc. Interface **18**, 20210209.
Gupta, J. K., C. H. Lin, and Q. Chen, 2009, Indoor Air **19**, 517.
Gupta, J. K., C. H. Lin, and Q. Y. Chen, 2010, Indoor Air **20**, 31.
Haas, C. N., 2015, Environ. Sci. Technol. **49**, 1245.
Hamed, R., and J. Fiegel, 2014, J. Biomed. Mater. Res., Part A **102**, 1788.
Hamilton, F., *et al.*, 2022, Thorax **77**, 276.
Han, Z. Y., W. G. Weng, and Q. Y. Huang, 2013, J. R. Soc. Interface **10**, 20130560.
Harper, G. J., 1961, Epidemiol. Infect. **59**, 479.
Hartmann, A., J. Lange, H. Rotheudt, and M. Kriegel, 2020, 10.14279/depositonce-10332.
Haslbeck, K., K. Schwarz, J. M. Hohlfeld, J. R. Seume, and W. Koch, 2010, J. Aerosol Sci. **41**, 429.
Hatch, G. E., 1992, in *Comparative Biology of the Normal Lung*, edited by R. A. Parent (CRC Press, Boca Raton), p. 793.
He, C., L. Morawska, and D. Gilbert, 2005, Atmos. Environ. **39**, 3891.
He, X., *et al.*, 2020, Nat. Med. **26**, 672.
Heintzenberg, J., 1994, Aerosol Sci. Technol. **21**, 46.
Helleis, F., T. Klimach, and U. Pöschl, 2021, 10.5281/zenodo.5070421.
Henderson, A. G., *et al.*, 2014, J. Clin. Invest. **124**, 3047.
Hendley, J. O., R. P. Wenzel, and J. M. Gwaltney, 1973, N. Engl. J. Med. **288**, 1361.
Henskens, Y. M. C., U. Velden, E. C. I. Veerman, and A. V. N. Amerongen, 1993, J. Periodontal Res. **28**, 43.
Heyder, J., J. Gebhart, G. Rudolf, C. Schiller, and W. Stahlhofen, 1986, J. Aerosol Sci. **17**, 811.
Hinds, W. C., 1999, *Aerosol Technology: Properties, Behavior, and Measurement of Airborne Particles* (Wiley, New York).
Hitchman, M. L., 2020, Future Virol. **15**, 823.
Hogan, Jr., C., E. Kettleson, M.-H. Lee, B. Ramaswami, L. Angenent, and P. Biswas, 2005, J. Appl. Microbiol. **99**, 1422.
Holmgren, H., B. Bake, A. C. Olin, and E. Ljungstrom, 2011, J. Aerosol Med. Pulm. Drug Delivery **24**, 253.
Holmgren, H., E. Gerth, E. Ljungstrom, P. Larsson, A. C. Almstrand, B. Bake, and A. C. Olin, 2013, Respir. Physiol. Neurobiol. **185**, 228.
Holmgren, H., and E. Ljungström, 2012, J. Aerosol Med. Pulm. Drug Delivery **25**, 47.
Holmgren, H., E. Ljungström, A.-C. Almstrand, B. Bake, and A.-C. Olin, 2010, J. Aerosol Sci. **41**, 439.
Hou, Y. J., *et al.*, 2020, Cell **182**, 429.
Howard, J., *et al.*, 2021, Proc. Natl. Acad. Sci. U.S.A. **118**, e2014564118.
Huffman, J. A., and S. Ratnesar-Shumate, 2020, Aerosol Sci. Technol. **54**, 463.
Huffman, J. A., *et al.*, 2020, Aerosol Sci. Technol. **54**, 465.
Hull, J., M. South, P. Phelan, and K. Grimwood, 1997, Am. J. Respir. Crit. Care Med. **156**, 161.
Humphrey, S. P., and R. T. Williamson, 2001, J. Prosthet. Dent. **85**, 162.
Huynh, E., A. Olinger, D. Woolley, R. K. Kohli, J. M. Choczynski, J. F. Davies, K. Lin, L. C. Marr, and R. D. Davis, 2022, Proc. Natl. Acad. Sci. U.S.A. **119**, e2109750119.

Hwang, S. E., J. H. Chang, B. Oh, and J. Heo, 2021, Int. J. Infect. Dis. **104**, 73.
Ijaz, M. K., A. H. Brunner, S. A. Sattar, R. C. Nair, and C. M. Johnson-Lussenburg, 1985, J. Gen. Virol. **66**, 2743.
Iwasaki, Y., M. Hoshi, R. Ito, K. Saito, and H. Nakazawa, 2006, J. Chromatogr. B **839**, 74.
Jayaraman, S., Y. Song, L. Vetrivel, L. Shankar, and A. Verkman, 2001, J. Clin. Invest. **107**, 317.
Jayaweera, M., H. Perera, B. Gunawardana, and J. Manatunge, 2020, Environ. Res. **188**, 109819.
Jing, B., C. Peng, Y. Wang, Q. Liu, S. Tong, Y. Zhang, and M. Ge, 2017, Sci. Rep. **7**, 43572.
Johansson, M. A., T. M. Quandelacy, S. Kada, P. V. Prasad, M. Steele, J. T. Brooks, R. B. Slayton, M. Biggerstaff, and J. C. Butler, 2021, JAMA Network Open **4**, e2035057.
John, W., 2011, in *Aerosol Measurement*, edited by P. Kulkarni, P. A. Baron, and K. Willeke (John Wiley & Sons, New York), Chap. 4, pp. 41–54.
Johnson, D. L., K. R. Mead, R. A. Lynch, and D. V. L. Hirst, 2013, Am. J. Infect. Control **41**, 254.
Johnson, G. R., and L. Morawska, 2009, J. Aerosol Med. Pulm. Drug Delivery **22**, 229.
Johnson, G. R., *et al.*, 2011, J. Aerosol Sci. **42**, 839.
Jones, R. M., and L. M. Brosseau, 2015, J. Occup. Environ. Med. **57**, 501.
Jones-Lopez, E. C., *et al.*, 2013, Am. J. Respir. Crit. Care Med. **187**, 1007.
Judson, S., and V. Munster, 2019, Viruses **11**, 940.
Kang, J.-H., Y.-H. Lee, and H.-S. Kho, 2018, BMC Oral Health **18**, 49.
Kang, M., *et al.*, 2020, Ann. Intern. Med. **173**, 974.
Kang, M., *et al.*, 2022, Eurosurveillance **27**, 2100815.
Ke, Z., *et al.*, 2020, Nature (London) **588**, 498.
Klompas, M., M. A. Baker, and C. Rhee, 2020, JAMA, J. Am. Med. Assoc. **324**, 441.
Klompas, M., M. Baker, and C. Rhee, 2021, JAMA Surg. **156**, 113.
Knibbs, L. D., L. Morawska, and S. C. Bell, 2012, Epidemiol. Infect. **140**, 474.
Knibbs, L. D., *et al.*, 2014, Thorax **69**, 740.
Knowles, M. R., J. M. Robinson, R. E. Wood, C. A. Pue, W. M. Mentz, G. C. Wager, J. T. Gatzy, and R. C. Boucher, 1997, J. Clin. Invest. **100**, 2588.
Kohanski, M. A., L. J. Lo, and M. S. Waring, 2020, Allergy Rhinol. **10**, 1173.
Köhler, H., 1936, Trans. Faraday Soc. **32**, 1152.
Kormuth, K. A., K. Lin, Aaron J. Prussin II, E. P. Vejerano, A. J. Tiwari, S. S. Cox, M. M. Myerburg, S. S. Lakdawala, and L. C. Marr, 2018, J. Infect. Dis. **218**, 739.
Kovalchuk, N. M., E. Nowak, and M. J. Simmons, 2016, Langmuir **32**, 5069.
Kreidenweis, S. M., K. Koehler, P. J. DeMott, A. J. Prenni, C. Carrico, and B. Ervens, 2005, Atmos. Chem. Phys. **5**, 1357.
Kulkarni, P., P. A. Baron, and K. Willeke, 2011, in *Aerosol Measurement: Principles, Techniques, and Applications*, edited by P. Kulkarni, P. A. Baron, and K. Willeke (John Wiley & Sons, New York), Chap. 2, pp. 15–30.
Kulmala, M., T. Vesala, and P. E. Wagner, 1993, Proc. R. Soc. A **441**, 589.
Kumar, B., N. Kashyap, A. Avinash, R. Chevvuri, M. K. Sagar, and K. Shrikant, 2017, Int. J. Contemp. Dent. Med. Rev. 011217, https://core.ac.uk/download/pdf/228420903.pdf.
Kutter, J. S., D. de Meulder, T. M. Bestebroer, P. Lexmond, A. Mulders, R. A. M. Fouchier, and S. Herfst, 2021, Nat. Commun. **12**, 1653.
Kutter, J. S., M. I. Spronken, P. L. Fraaij, R. A. M. Fouchier, and S. Herfst, 2018, Curr. Opin. Virol. **28**, 142.
Kwon, K. S., J. I. Park, Y. J. Park, D. M. Jung, K. W. Ryu, and J. H. Lee, 2020, J. Korean Med. Sci. **35**, e415.
Lai, A., 2002, Indoor Air **12**, 211.
Lai, A. C. K., T. F. Tan, W. S. Li, and D. K. M. Ip, 2018, Indoor Air **28**, 73.
Lai, K.-M., C. Bottomley, and R. McNerney, 2011, PLoS One **6**, e20086.
Lakey, P. S. J., T. Berkemeier, H. J. Tong, A. M. Arangio, K. Lucas, U. Poschl, and M. Shiraiwa, 2016, Sci. Rep. **6**, 32916.
Langmuir, A. D., 1961, Bacteriol. Rev. **25**, 173.
Langmuir, I., 1918, Phys. Rev. **12**, 368.
Larsson, B., G. Olivecrona, and T. Ericson, 1996, Arch. Oral Biol. **41**, 105.
Laskina, O., H. S. Morris, J. R. Grandquist, Z. Qiu, E. A. Stone, A. V. Tivanski, and V. H. Grassian, 2015, J. Phys. Chem. A **119**, 4489.
Lednicky, J. A., M. Lauzardo, M. M. Alam, M. A. Elbadry, C. J. Stephenson, J. C. Gibson, and J. G. Morris, Jr., 2021, Int. J. Infect. Dis. **108**, 212.
Lednicky, J. A., and J. C. Loeb, 2013, Influenza Res. Treat. **2013**, 656825.
Lednicky, J. A., *et al.*, 2020, Int. J. Infect. Dis. **100**, 476.
Lee, E. C., N. I. Wada, M. K. Grabowski, E. S. Gurley, and J. Lessler, 2020, Science **370**, 406.
Lee, J., D. Yoo, S. Ryu, S. Ham, K. Lee, M. Yeo, K. Min, and C. Yoon, 2019, Aerosol Air Qual. Res. **19**, 840.
Leith, D., C. L'Orange, and J. Volckens, 2021, Environ. Sci. Technol. **55**, 3136.
Lelieveld, J., F. Helleis, S. Borrmann, Y. Cheng, F. Drewnick, G. Haug, T. Klimach, J. Sciare, H. Su, and U. Pöschl, 2020, Int. J. Environ. Res. Public Health **17**, 8114.
Leung, N. H. L., 2021, Nat. Rev. Microbiol. **19**, 528.
Leung, N. H. L., *et al.*, 2020, Nat. Med. **26**, 676.
Lever, M. S., A. Williams, and A. M. Bennett, 2000, Lett. Appl. Microbiol. **31**, 238.
Levitzky, M. G., 2017, *Pulmonary Physiology*, 9th ed. (McGraw-Hill, New York).
Lhuissier, H., and E. Villermaux, 2009, Phys. Fluids **21**, 091111.
Lhuissier, H., and E. Villermaux, 2012, J. Fluid Mech. **696**, 5.
Li, L., M. Niu, and Y. Zhu, 2021, Aerosol Sci. Technol. **55**, 332.
Li, X., D. Gupta, H.-J. Eom, H. Kim, and C.-U. Ro, 2014, Atmos. Environ. **82**, 36.
Li, Y., 2021, Indoor Air **31**, 3.
Li, Y., S. Duan, I. T. S. Yu, and T. W. Wong, 2005, Indoor Air **15**, 96.
Li, Y., *et al.*, 2007, Indoor Air **17**, 2.
Lieber, C., S. Melekidis, R. Koch, and H.-J. Bauer, 2021, J. Aerosol Sci. **154**, 105760.
Lightstone, J. M., T. B. Onasch, D. Imre, and S. Oatis, 2000, J. Phys. Chem. A **104**, 9337.
Liljeroos, L., J. T. Huiskonen, A. Ora, P. Susi, and S. J. Butcher, 2011, Proc. Natl. Acad. Sci. U.S.A. **108**, 18085.
Lin, K., and L. C. Marr, 2020, Environ. Sci. Technol. **54**, 1024.
Lin, P. L., and J. L. Flynn, 2010, J. Immunol. **185**, 15.
Lindsley, W. G., *et al.*, 2010a, Clin. Infect. Dis. **50**, 693.
Lindsley, W. G., *et al.*, 2010b, PLoS One **5**, e15100.
Lindsley, W. G., *et al.*, 2012, J. Occup. Environ. Hyg. **9**, 443.
Lindsley, W. G., *et al.*, 2021, Aerosol Sci. Technol. **55**, 1125.

Little, J. W., R. D. Gordon, W. J. Hall Jr., and F. K. Roth, 1979, J. Med. Virol. **3**, 177.
Liu, H., S. He, L. Shen, and J. Hong, 2021, Phys. Fluids **33**, 023301.
Liu, L., J. Wei, Y. Li, and A. Ooi, 2017, Indoor Air **27**, 179.
Liu, P., *et al.*, 2018, Nat. Commun. **9**, 4076.
Liu, Y., *et al.*, 2020, Nature (London) **582**, 557.
Lloyd-Smith, J. O., S. J. Schreiber, P. E. Kopp, and W. M. Getz, 2005, Nature (London) **438**, 355.
Loudon, R. G., and R. M. Roberts, 1967a, Am. Rev. Respir. Dis. **95**, 435.
Loudon, R. G., and R. M. Roberts, 1967b, Nature (London) **213**, 95.
Lu, J., J. Gu, K. Li, C. Xu, W. Su, Z. Lai, D. Zhou, C. Yu, B. Xu, and Z. Yang, 2020, Emerging Infect. Dis. **26**, 1628.
Madas, B. G., P. Furi, A. Farkas, A. Nagy, A. Czitrovszky, I. Balashazy, G. G. Schay, and A. Horvath, 2020, Sci. Rep. **10**, 22430.
Maggiore, E., M. Tommasini, and P. M. Ossi, 2021, Aerosol Sci. Technol. **55**, 340.
Mahjoub Mohammed Merghani, K., B. Sagot, E. Gehin, G. Da, and C. Motzkus, 2021, Indoor Air **31**, 7.
Mainelis, G., 2020, Aerosol Sci. Technol. **54**, 496.
Marr, L. C., J. W. Tang, J. Van Mullekom, and S. S. Lakdawala, 2019, J. R. Soc. Interface **16**, 20180298.
Martin, S. T., 2000, Chem. Rev. **100**, 3403.
Martin, S. T., *et al.*, 2010, Atmos. Chem. Phys. **10**, 11415.
Mathai, V., A. Das, J. A. Bailey, and K. Breuer, 2021, Sci. Adv. **7**, eabe0166.
Matricardi, P. M., R. W. Dal Negro, and R. Nisini, 2020, Pediatr. Allergy Immunol. **31**, 454.
McDevitt, J. J., P. Koutrakis, S. T. Ferguson, J. M. Wolfson, M. P. Fabian, M. Martins, J. Pantelic, and D. K. Milton, 2013, Aerosol Sci. Technol. **47**, 444.
McNeill, V. F., 2022, Annu. Rev. Chem. Biomol. Eng. **13**, 123.
Meadow, J. F., A. E. Altrichter, A. C. Bateman, J. Stenson, G. Z. Brown, J. L. Green, and B. J. M. Bohannan, 2015, PeerJ **3**, e1258.
Meurman, J. H., P. Rantonen, H. Pajukoski, and R. Sulkava, 2002, Oral Surg. Oral Med. Oral Pathol. Oral Radiol. **94**, 432.
Mikhailov, E., S. Vlasenko, S. T. Martin, T. Koop, and U. Pöschl, 2009, Atmos. Chem. Phys. **9**, 9491.
Mikhailov, E., S. Vlasenko, R. Niessner, and U. Pöschl, 2004, Atmos. Chem. Phys. **4**, 323.
Mikhailov, E., S. Vlasenko, D. Rose, and U. Poschl, 2013, Atmos. Chem. Phys. **13**, 717.
Mikhailov, E. F., and S. S. Vlasenko, 2020, Atmos. Meas. Tech. **13**, 2035.
Mikhailov, E. F., *et al.*, 2021, Atmos. Chem. Phys. **21**, 6999.
Miller, S. L., J. Linnes, and J. Luongo, 2013, Photochem. Photobiol. **89**, 777.
Miller, S. L., W. W. Nazaroff, J. L. Jimenez, A. Boerstra, G. Buonanno, S. J. Dancer, J. Kurnitski, L. C. Marr, L. Morawska, and C. Noakes, 2021, Indoor Air **31**, 314.
Milton, D., 2012, Front. Cell. Infect. Microbiol. **2**, 150.
Milton, D. K., 2020, J. Pediatr. Infect. Dis. Soc. **9**, 413.
Milton, D. K., M. P. Fabian, B. J. Cowling, M. L. Grantham, and J. J. McDevitt, 2013, PLoS Pathog. **9**, e1003205.
Misra, C., M. Singh, S. Shen, C. Sioutas, and P. M. Hall, 2002, J. Aerosol Sci. **33**, 1027.
Mittal, R., C. Meneveau, and W. Wu, 2020, Phys. Fluids **32**, 101903.
Mittal, R., R. Ni, and J.-H. Seo, 2020b, J. Fluid Mech. **894**, F2.
Mitze, T., R. Kosfeld, J. Rode, and K. Wälde, 2020, Proc. Natl. Acad. Sci. U.S.A. **117**, 32293.
Morawska, L., 2006, Indoor Air **16**, 335.
Morawska, L., G. Johnson, Z. Ristovski, M. Hargreaves, K. Mengersen, C. Chao, M. Wan, Y. Li, X. Xie, and D. Katoshevski, 2008, in *Proceedings of the 11th International Conference on Indoor Air Quality and Climate, Copenhagen, 2008*, edited by B. W. Olesen, J. Toftum, P. Wargocki, D. Zukowska, and P. Strom-Tejsen (Technical University of Denmark, Kongens Lyngby, Denmark), pp. 1–8.
Morawska, L., G. R. Johnson, Z. D. Ristovski, M. Hargreaves, K. Mengersen, S. Corbett, C. Y. H. Chao, Y. Li, and D. Katoshevski, 2009, J. Aerosol Sci. **40**, 256.
Morawska, L., and D. K. Milton, 2020, Clin. Infect. Dis. **71**, 2311.
Morawska, L., *et al.*, 2020, Environ. Int. **142**, 105832.
Moriarty, J. A., and J. B. Grotberg, 1999, J. Fluid Mech. **397**, 1.
Mosley, V. M., and R. W. G. Wyckoff, 1946, Nature (London) **157**, 263.
Murata, T., M.-S. Lee, and A. Tanioka, 1999, J. Colloid Interface Sci. **220**, 250.
Mürbe, D., M. Kriegel, J. Lange, H. Rotheudt, and M. Fleischer, 2021, Sci. Rep. **11**, 1.
Namati, E., J. Thiesse, J. de Ryk, and G. McLennan, 2008, Am. J. Respir. Cell Mol. Biol. **38**, 572.
NASEM, 2020, *Airborne Transmission of SARS-CoV-2: Proceedings of a Workshop—In Brief* (National Academies Press, Washington, DC).
Nazaroff, W. W., 2016, Indoor Air **26**, 61.
Ng, C. S., K. L. Chong, R. Yang, M. Li, R. Verzicco, and D. Lohse, 2021, Phys. Rev. Fluids **6**, 054303.
Niazi, S., R. Groth, L. Cravigan, C. R. He, J. W. Tang, K. Spann, and G. R. Johnson, 2021, Environ. Sci. Technol. **55**, 499.
Niazi, S., R. Groth, K. Spann, and G. R. Johnson, 2021, Environ. Pollut. **276**, 115767.
Nicas, M., W. W. Nazaroff, and A. Hubbard, 2005, J. Occup. Environ. Hyg. **2**, 143.
Niimura, Y., and K. Hasegawa, 2019, PLoS One **14**, e0212074.
Nissen, K., J. Krambrich, D. Akaberi, T. Hoffman, J. Ling, A. K. Lundkvist, L. Svensson, and E. Salaneck, 2020, Sci. Rep. **10**, 19589.
Nomaguchi, M., M. Fujita, Y. Miyazaki, and A. Adachi, 2012, Front. Microbiol. **3**, 281.
Nordsiek, F., E. Bodenschatz, and G. Bagheri, 2021, PLoS One **16**, e0248004.
Noti, J. D., F. M. Blachere, C. M. McMillen, W. G. Lindsley, M. L. Kashon, D. R. Slaughter, and D. H. Beezhold, 2013, PLoS One **8**, e57485.
Olsen, S. J., *et al.*, 2003, N. Engl. J. Med. **349**, 2416.
Oswin, H. P., *et al.*, 2022, Proc. Natl. Acad. Sci. U.S.A. **119**, e2200109119.
Pan, J., C. Harb, W. Leng, and L. C. Marr, 2021, Aerosol Sci. Technol. **55**, 718.
Pan, M., L. Carol, J. A. Lednicky, A. Eiguren-Fernandez, S. Hering, Z. H. Fan, and C.-Y. Wu, 2019, Aerosol Sci. Technol. **53**, 583.
Pancic, F., D. C. Carpentier, and P. E. Came, 1980, J. Clin. Microbiol. **12**, 567.
Papineni, R. S., and F. S. Rosenthal, 1997, J. Aerosol Med. **10**, 105.
Paramonov, M., P. P. Aalto, A. Asmi, N. Prisle, V. M. Kerminen, M. Kulmala, and T. Petäjä, 2013, Atmos. Chem. Phys. **13**, 10285.
Patterson, B., and R. Wood, 2019, Tuberculosis **117**, 31.
Patterson, B., *et al.*, 2018, Gates Open Res. **1**, 11.
Peters, T. M., and D. Leith, 2003, J. Aerosol Sci. **34**, 627.
Petters, M. D., and S. M. Kreidenweis, 2007, Atmos. Chem. Phys. **7**, 1961.
Pfeifer, S., *et al.*, 2016, Atmos. Meas. Tech. **9**, 1545.
Pfrommer, E., C. Dreier, G. Gabriel, T. Dallenga, R. Reimer, K. Schepanski, R. Scherließ, U. E. Schaible, and T. Gutsmann, 2020, Sci. Rep. **10**, 9159.

Pica, N., and N. M. Bouvier, 2012, Curr. Opin. Virol. **2**, 90.
Pitkäranta, A., and F. G. Hayden, 1998, Ann. Med. **30**, 529.
Pöhlker, M. L., *et al.*, 2016, Atmos. Chem. Phys. **16**, 15709.
Pöhlker, M. L., *et al.*, 2018, Atmos. Chem. Phys. **18**, 10289.
Port, J. R., *et al.*, 2021, Nat. Commun. **12**, 4985.
Pöschl, U., 2005, Angew. Chem., Int. Ed. Engl. **44**, 7520.
Poydenot, F., I. Abdourahamane, E. Caplain, S. Der, J. Haiech, A. Jallon, I. Khoutami, A. Loucif, E. Marinov, and B. Andreotti, 2022, PNAS Nexus **1**, pgac223.
Prather, K. A., L. C. Marr, R. T. Schooley, M. A. McDiarmid, M. E. Wilson, and D. K. Milton, 2020, Science **370**, 303.
Prather, K. A., C. C. Wang, and R. T. Schooley, 2020, Science **368**, 1422.
Prather, K. A., *et al.*, 2013, Proc. Natl. Acad. Sci. U.S.A. **110**, 7550.
Prussin, A. J., E. B. Garcia, and L. C. Marr, 2015, Environ. Sci. Technol. Lett. **2**, 84.
Pyankov, O. V., S. A. Bodnev, O. G. Pyankova, and I. E. Agranovski, 2018, J. Aerosol Sci. **115**, 158.
Pyankov, O. V., O. G. Pyankova, and I. E. Agranovski, 2012, J. Aerosol Sci. **53**, 21.
Quinn, P. K., D. B. Collins, V. H. Grassian, K. A. Prather, and T. S. Bates, 2015, Chem. Rev. **115**, 4383.
Randall, K., E. T. Ewing, L. C. Marr, J. L. Jimenez, and L. Bourouiba, 2021, Interface Focus **11**, 20210049.
Rantonen, P. J. F., and J. H. Meurman, 2000, Acta Odontol. Scand. **58**, 160.
Ren, S., J. L. Niu, Z. H. Luo, Y. Shi, M. L. Cai, Z. J. Luo, and Q. H. Yu, 2020, Complexity 9036369.
Renbaum-Wolff, L., M. Song, C. Marcolli, Y. Zhang, P. F. Liu, J. W. Grayson, F. M. Geiger, S. T. Martin, and A. K. Bertram, 2016, Atmos. Chem. Phys. **16**, 7969.
Renke, W., 2016, in *Dental Caries: Principles and Management*, edited by Z. Xuedong (Springer, Berlin), pp. 59–69.
Rennard, S. I., *et al.*, 1990, Am. Rev. Respir. Dis. **141**, 208.
Reynolds, K. A., P. I. Beamer, K. R. Plotkin, L. Y. Sifuentes, D. W. Koenig, and C. P. Gerba, 2016, Arch. Environ. Occup. Health **71**, 157.
Richard, M., and R. A. M. Fouchier, 2016, FEMS Microbiol. Rev. **40**, 68.
Riemer, N., A. P. Ault, M. West, R. L. Craig, and J. H. Curtis, 2019, Rev. Geophys. **57**, 187.
Riley, E. C., G. Murphy, and R. L. Riley, 1978, Am. J. Epidemiol. **107**, 421.
Riley, R. L., 1974, Am. J. Med. **57**, 466.
Riley, R. L., C. C. Mills, W. Nyka, N. Weinstock, P. B. Storey, L. U. Sultan, M. C. Riley, and W. F. Wells, 1959, Am. J. Hyg. **70**, 185.
Riley, R. L., D. N. Shivpuri, F. Wittstadt, F. Ogrady, L. U. Sultan, and C. C. Mills, 1962, Am. Rev. Respir. Dis. **85**, 511, https://www.atsjournals.org/doi/epdf/10.1164/arrd.1962.85.4.511?role=tab.
Riley, W. J., T. E. McKone, A. C. Lai, and W. W. Nazaroff, 2002, Environ. Sci. Technol. **36**, 200.
Rogak, S. N., T. A. Sipkens, M. Guan, H. Nikookar, D. Vargas Figueroa, and J. Wang, 2021, Aerosol Sci. Technol. **55**, 398.
Rose, D., S. S. Gunthe, E. Mikhailov, G. P. Frank, U. Dusek, M. O. Andreae, and U. Poeschl, 2008, Atmos. Chem. Phys. **8**, 1153.
Rossman, J. S., and R. A. Lamb, 2011, Virology **411**, 229.
Rothamer, D. A., S. Sanders, D. Reindl, and T. H. Bertram, 2021, Sci. Technol. Built Environ. **27**, 1181.
Roy, C. J., and D. K. Milton, 2004, N. Engl. J. Med. **350**, 1710.
Roy, C. J., D. S. Reed, and J. A. Hutt, 2010, Vet. Pathol. **47**, 779.
Rudnick, S. N., and D. K. Milton, 2003, Indoor Air **13**, 237.
Santarpia, J. L., S. Ratnesar-Shumate, and A. Haddrell, 2020, Aerosol Sci. Technol. **54**, 585.
Santarpia, J. L., *et al.*, 2020, Sci. Rep. **10**, 12732.
Santarpia, J. L., *et al.*, 2022, J. Exposure Sci. Environ. Epidemiol. **32**, 706.
Santl-Temkiv, T., *et al.*, 2020, Aerosol Sci. Technol. **54**, 520.
Sarkar, A., F. Xu, and S. Lee, 2019, Adv. Colloid Interface Sci. **273**, 102034.
Satija, N., and S. K. Lal, 2007, Ann. N.Y. Acad. Sci. **1102**, 26.
Scarpelli, E. M., 1998, Anat. Rec. **251**, 491.
Scarpelli, E. M., and B. A. Hills, 2000, J. Appl. Physiol. **89**, 408.
Schafer, M. P., 1999, Aerosol Sci. Technol. **30**, 161.
Schenkels, L. C. P. M., E. C. I. Veerman, and A. V. Nieuw Amerongen, 1995, Crit. Rev. Oral Biol. Med. **6**, 161.
Scheuch, G., 2020, J. Aerosol Med. Pulm. Drug Delivery **33**, 230.
Schicht, M., *et al.*, 2015, Ann. Anat. **199**, 92.
Schuit, M., S. Gardner, S. Wood, K. Bower, G. Williams, D. Freeburger, and P. Dabisch, 2020, J. Infect. Dis. **221**, 372.
Schulze-Röbbecke, R., 2014, Krankenhaushygiene up2date **09**, 281, https://www.thieme-connect.com/products/ejournals/html/10.1055/s-0034-1391270.
Schwarz, K., H. Biller, H. Windt, W. Koch, and J. M. Hohlfeld, 2010, J. Aerosol Med. Pulm. Drug Delivery **23**, 371.
Schwarz, K., H. Biller, H. Windt, W. Koch, and J. M. Hohlfeld, 2015, J. Aerosol Med. Pulm. Drug Delivery **28**, 52.
Schwarz, K., O. Holz, and J. M. Hohlfeld, 2020, in *Breathborne Biomarkers and the Human Volatilome*, 2nd ed., edited by J. Beauchamp, C. Davis, and J. Pleil (Elsevier, Boston), Chap. 8, pp. 121–133.
Seinfeld, J. H., and S. N. Pandis, 2016, *Atmospheric Chemistry and Physics* (John Wiley & Sons, New York).
Seminara, G., B. Carli, G. Forni, S. Fuzzi, A. Mazzino, and A. Rinaldo, 2020, Rend. Lincei Sci. Fis. Nat. **31**, 505.
Seto, W. H., 2015, J. Hosp. Infect. **89**, 225.
Shaffer, R. E., and S. Rengasamy, 2009, J. Nanopart. Res. **11**, 1661.
Shante, V. K. S., and S. Kirkpatrick, 1971, Adv. Phys. **20**, 325.
Sherertz, R. J., S. Bassetti, and B. Bassetti-Wyss, 2001, Emerging Infect. Dis. **7**, 241.
Shinya, K., M. Ebina, S. Yamada, M. Ono, N. Kasai, and Y. Kawaoka, 2006, Nature (London) **440**, 435.
Shiraiwa, M., M. Ammann, T. Koop, and U. Pöschl, 2011, Proc. Natl. Acad. Sci. U.S.A. **108**, 11003.
Shiraiwa, M., C. Pfrang, T. Koop, and U. Pöschl, 2012, Atmos. Chem. Phys. **12**, 2777.
Shiu, E. Y. C., W. Huang, D. Ye, Y. Xie, J. Mo, Y. Li, B. J. Cowling, Z. Yang, and N. H. L. Leung, 2020, Indoor Air **30**, 805.
Singh, M., C. Misra, and C. Sioutas, 2003, Atmos. Environ. **37**, 4781.
Sinha, A., K. K. Lee, G. F. Rafferty, N. Yousaf, I. D. Pavord, J. Galloway, and S. S. Birring, 2016, Eur. Respir. J. **47**, 1461.
Slade, R., K. Crissman, J. Norwood, and G. Hatch, 1993, Exp. Lung Res. **19**, 469.
Smith, S. H., G. A. Somsen, C. van Rijn, S. Kooij, L. van der Hoek, R. A. Bem, and D. Bonn, 2020, Phys. Fluids **32**, 107108.
Smither, S. J., L. S. Eastaugh, J. S. Findlay, and M. S. Lever, 2020, Emerging Microbes Infect. **9**, 1415.
Snyder, M. H., E. H. Stephenson, H. Young, C. G. York, E. L. Tierney, W. T. London, R. M. Chanock, and B. R. Murphy, 1986, J. Infect. Dis. **154**, 709.
Song, M., P. Liu, S. T. Martin, and A. K. Bertram, 2017, Atmos. Chem. Phys. **17**, 11261.
Song, M., C. Marcolli, U. K. Krieger, A. Zuend, and T. Peter, 2012, Atmos. Chem. Phys. **12**, 2691.
Songer, J. R., 1967, Appl. Microbiol. **15**, 35.
Sonkin, L. S., 1951, Am. J. Epidemiol. **53**, 337.

Stadnytskyi, V., C. E. Bax, A. Bax, and P. Anfinrud, 2020, Proc. Natl. Acad. Sci. U.S.A. **117**, 11875.
Stern, R. A., P. Koutrakis, M. A. G. Martins, B. Lemos, S. E. Dowd, E. M. Sunderland, and E. Garshick, 2021, Respir. Res. **22**, 73.
Stiti, M., G. Castanet, A. Corber, M. Alden, and E. Berrocal, 2022, Environ. Res. **204**, 112072.
Stokes, R. H., and R. A. Robinson, 1966, J. Phys. Chem. **70**, 2126.
Suh, K.-I., Y.-K. Kim, and H.-S. Kho, 2009, Arch. Oral Biol. **54**, 797.
Sumner, H., A. Woodcock, U. Kolsum, R. Dockry, A. L. Lazaar, D. Singh, J. Vestbo, and J. A. Smith, 2013, Am. J. Respir. Crit. Care Med. **187**, 943.
Sunger, K., W. Powley, A. Kelsall, H. Sumner, R. Murdoch, and J. A. Smith, 2013, Eur. Respir. J. **41**, 277.
Sutinen, S., H. Riska, R. Backman, S. Sutinen, and B. Fröseth, 1995, Respir. Med. **89**, 85.
Tang, I. N., and H. R. Munkelwitz, 1994, J. Appl. Meteorol. Climatol. **33**, 791.
Tang, J. W., 2009, J. R. Soc. Interface **6**, S737.
Tang, J. W., *et al.*, 2021, J. Hosp. Infect. **110**, 89.
Tang, S., *et al.*, 2020, Environ. Int. **144**, 106039.
Tellier, R., Y. G. Li, B. J. Cowling, and J. W. Tang, 2019, BMC Infect. Dis. **19**, 101.
Teske, S. S., M. H. Weir, T. A. Bartrand, Y. Huang, S. B. Tamrakar, and C. N. Haas, 2014, Risk Anal. **34**, 911.
Thomas, R. J., 2013, Virulence **4**, 847.
Thomas, R. J., *et al.*, 2009, Infect. Immun. **77**, 1315.
Thompson, A. B., T. Bohling, F. Payvandi, and S. I. Rennard, 1990, J. Lab. Clin. Med. **115**, 148, https://pubmed.ncbi.nlm.nih.gov/2299262/.
Tindale, L. C., J. E. Stockdale, M. Coombe, E. S. Garlock, W. Y. V. Lau, M. Saraswat, L. Zhang, D. Chen, J. Wallinga, and C. Colijn, 2020, eLife **9**, e57149.
Tortora, G. J., and B. Derrickson, 2017, *Principles of Anatomy & Physiology*, 15th ed. (John Wiley & Sons, Hoboken, NJ).
van der Vliet, A., and C. E. Cross, 2000, Am. J. Med. **109**, 398.
van der Vliet, A., C. A. O'Neill, C. E. Cross, J. M. Koostra, W. G. Volz, B. Halliwell, and S. Louie, 1999, Am. J. Physiol. Lung Cell Mol. Physiol. **276**, L289.
van Doremalen, N., *et al.*, 2020, N. Engl. J. Med. **382**, 1564.
van Kampen, J. J. A., *et al.*, 2021, Nat. Commun. **12**, 267.
van Riel, D., V. J. Munster, E. de Wit, G. F. Rimmelzwaan, R. A. M. Fouchier, A. D. M. E. Osterhaus, and T. Kuiken, 2007, Am. J. Pathol. **171**, 1215.
Vejerano, E. P., and L. C. Marr, 2018, J. R. Soc. Interface **15**, 20170939.
Veldhuizen, R., K. Nag, S. Orgeig, and F. Possmayer, 1998, Biochim. Biophys. Acta **1408**, 90.
Vette, A. F., A. W. Rea, P. A. Lawless, C. E. Rodes, G. Evans, V. R. Highsmith, and L. Sheldon, 2001, Aerosol Sci. Technol. **34**, 118.
Vignes, A., 1966, Ind. Eng. Chem. Fundam. **5**, 189.
Villermaux, E., 2020, J. Fluid Mech. **898**, P1.
Villermaux, E., A. Moutte, M. Amielh, and P. Meunier, 2017, Phys. Rev. Fluids **2**, 074501.
Vincent, J. H., D. Mark, B. G. Miller, L. Armbruster, and T. L. Ogden, 1990, J. Aerosol Sci. **21**, 577.
Volckens, J., and T. M. Peters, 2005, J. Aerosol Sci. **36**, 1400.
Volkwein, J. C., A. D. Maynard, and M. Harper, 2011, in *Aerosol Measurement: Principles, Techniques, and Applications*, edited by P. Kulkarni, P. A. Baron, and K. Willeke (John Wiley & Sons, New York), Chap. 25, pp. 571–590.
von der Weiden, S. L., F. Drewnick, and S. Borrmann, 2009, Atmos. Meas. Tech. **2**, 479.
Wainwright, C. E., *et al.*, 2009, Thorax **64**, 926.
Wang, J., M. Alipour, G. Soligo, A. Roccon, M. De Paoli, F. Picano, and A. Soldati, 2021, Proc. Natl. Acad. Sci. U.S.A. **118**, e2105279118.
Webb, S. J., R. Bather, and R. W. Hodges, 1963, Can. J. Microbiol. **9**, 87.
Wei, J., and Y. Li, 2015, Build. Environ. **93**, 86.
Wei, J. J., and Y. G. Li, 2017, PLoS One **12**, e0169235.
Wells, W. F., 1934, Am. J. Epidemiol. **20**, 611.
Wells, W. F., 1955, *Airborne Contagion and Air Hygiene: An Ecological Study of Droplet Infections* (Oxford University Press, London).
Wells, W. F., and M. W. Wells, 1936, JAMA, J. Am. Med. Assoc. **107**, 1698.
Wex, H., *et al.*, 2016, Atmos. Chem. Phys. **16**, 14107.
Wiedensohler, A., W. Birmili, J. P. Putaud, J. Ogren, I. Colbeck, and M. Lazaridis, 2014, *Recommendations for Aerosol Sampling, Aerosol Science: Technology and Applications* (Blackwell Science, Oxford).
Willeke, K., and K. T. Whitby, 1975, J. Air Pollut. Control Assoc. **25**, 529.
Wilson, N. M., G. B. Marks, A. Eckhardt, A. Clarke, F. Young, F. L. Garden, W. Stewart, T. M. Cook, and E. R. Tovey, 2021, Anaesthesia **76**, 1465.
Wilson, N. M., A. Norton, F. P. Young, and D. W. Collins, 2020, Anaesthesia **75**, 1086.
Wolfel, R., *et al.*, 2020, Nature (London) **581**, 465.
Wong, T.-w., *et al.*, 2004, Emerging Infect. Dis. **10**, 269.
Xie, X., Y. Li, A. Chwang, P. Ho, and W. Seto, 2007, Indoor Air **17**, 211.
Xie, X. J., Y. G. Li, H. Q. Sun, and L. Liu, 2009, J. R. Soc. Interface **6**, S703.
Yamamoto, N., D. Hospodsky, K. C. Dannemiller, W. W. Nazaroff, and J. Peccia, 2015, Environ. Sci. Technol. **49**, 5098.
Yan, J., M. Grantham, J. Pantelic, P. J. B. de Mesquita, B. Albert, F. J. Liu, S. Ehrman, D. K. Milton, and E. Consortium, 2018, Proc. Natl. Acad. Sci. U.S.A. **115**, 1081.
Yang, F., A. A. Pahlavan, S. Mendez, M. Abkarian, and H. A. Stone, 2020, Phys. Rev. Fluids **5**, 122501.
Yang, S., G. Bekö, P. Wargocki, J. Williams, and D. Licina, 2021, Environ. Sci. Technol. **55**, 509.
Yang, S. H., G. W. M. Lee, C. M. Chen, C. C. Wu, and K. P. Yu, 2007, J. Aerosol Med. **20**, 484.
Yao, H., *et al.*, 2020, Cell **183**, 730.
Yeh, H.-C., and G. Schum, 1980, Bull. Math. Biol. **42**, 461.
You, R. Y., W. L. Cui, C. Chen, and B. Zhao, 2013, Aerosol Air Qual. Res. **13**, 911.
Yousaf, N., W. Monteiro, S. Matos, S. S. Birring, and I. D. Pavord, 2013, Eur. Respir. J. **41**, 241.
Yu, I. T. S., Y. Li, T. W. Wong, W. Tam, A. T. Chan, J. H. W. Lee, D. Y. C. Leung, and T. Ho, 2004, N. Engl. J. Med. **350**, 1731.
Zayas, G., M. C. Chiang, E. Wong, F. MacDonald, C. F. Lange, A. Senthilselvan, and M. King, 2012, BMC Pulm. Med. **12**, 11.
Zhang, N., W. Chen, P.-T. Chan, H.-L. Yen, J. W.-T. Tang, and Y. Li, 2020, Indoor Air **30**, 645.
Zhu, N., *et al.*, 2020, N. Engl. J. Med. **382**, 727.
Zuend, A., C. Marcolli, B. P. Luo, and T. Peter, 2008, Atmos. Chem. Phys. **8**, 4559.
Zuo, Y. Y., W. E. Uspal, and T. Wei, 2020, ACS Nano **14**, 16502.
Zuo, Z., T. H. Kuehn, H. Verma, S. Kumar, S. M. Goyal, J. Appert, P. C. Raynor, S. Ge, and D. Y. H. Pui, 2013, Aerosol Sci. Technol. **47**, 373.